UCLouvain
Institute of Mechanics,
Materials and Civil Engineering

Interactions between flow and actuated structures simulated through a Vortex Particle-Mesh method: application to swimming and energy harvesting devices

Caroline Bernier

Thesis submitted in partial fulfilment for the degree of *Docteur en Sciences de l'Ingénieur*

Dissertation commitee

Prof. Philippe Chatelain (Supervisor)	UCLouvain, Belgium
Prof. Renaud Ronsse (Supervisor)	UCLouvain, Belgium
Prof. Paul Fisette	UCLouvain, Belgium
Prof. Laurent Delannay(Chairperson)	UCLouvain, Belgium
Prof. Mattia Gazzola	University of Illinois at Urbana-Champaign, USA
Prof. Chloé Mimeau	Conservatoire national des arts et métiers, France

Louvain-la-Neuve, 2021

Remerciements

A l'issue de ce travail, je tiens à adresser mes remerciements à de nombreuses personnes. En effet, toute seule, les résultats de cette thèse auraient certainement été bien différents sans leur précieuse contribution.

Tout d'abord, je tiens à remercier mes promoteurs Philippe Chatelain et Renaud Ronsse de m'avoir proposé ce sujet de thèse et de m'avoir soutenue et rassurée tout au long de ces 6 dernières années. Merci pour ces innombrables réunions surtout quand les résultats se faisaient attendre ...

Je souhaite également remercier tous les membres de mon jury : Paul Fisette, Mattia Gazzola, Chloé Mimeau, Laurent Delannay, Renaud Ronsse, Philippe Chatelain pour leur examen minutieux de ce document ainsi que pour leurs remarques et commentaires avisés lors de la défense privée.

Merci également aux deux départements qui m'ont acceuillie TFL et MEED et à tous les collègues avec lesquels j'ai travaillé durant toutes ces années. Je remercie tout spécialement Isabelle et Astrid. Merci pour leur bonne humeur et leur efficacité au quotidien. Je remercie tous les collègues de l'ancienne équipe TFL avec qui j'ai commencé : Benjamin, Denis-Gabriel, Elise, Matthieu, Maud, Olivier, Philippe B., Philippe P. et Thomas. Je remercie aussi Anouk, Baptiste, David, Denis, François, Gauthier, Ignace, Marion, Maxime, Pierre, Romain, Victoria et Victor! L'ancienne équipe MEED avec Caroline, Christophe E., Corentin, François H., Guillaume B., Olivier, Sophie et Xavier ; ainsi que la nouvelle équipe avec Ali, Christophe, Emile, Gianmarco, Guillaume C., Guillaume F., Henri, Jeanne, Joachim, Lisa, Sébastien et Virginie.

Je souhaite aussi remercier plus particulièrement l'équipe mécatro Christophe, Guillaume C. et Guillaume F., avec qui encadrer cette option a été un vrai plaisir. Je remercie Caroline et Sophie pour le partage de nombreux temps de midi et nombreuses soirées sport qui ont égaillé ces années (avant le covid 19).

J'en profite également pour remercier ceux qui comptent le plus pour moi et qui me soutiennent depuis des années: mes amis et ma famille.

Je remercie Aude, pour son soutien essentiel dans les moments de doutes, pour ses relectures en tout genre pendant ces 6 années et pour m'avoir donné l'opportunité de venir la rejoindre en Australie, espérons qu'on puisse un jour y retourner. Je remercie PA, pour les pauses avec cappuccino de la machine à café de l'Euler, pour les discussions, pour les conseils de rédaction et pour les soirées jeux de société. Aude et PA ont été un indispensable et précieux soutien pendant toutes ces années! Je remercie Anaïs, pour les encouragements dans les moments difficiles et les fous rires légendaires notamment pendant le road trip au Canada qui restera un super bon souvenir.

Je remercie Maman, Mamy et mon frère Alexandre, d'avoir toujours été à mes cotés, de m'avoir encouragée et soutenue.

Je remercie Lucas d'être mon réconfort dans les moments de doute et surtout d'avoir embelli ma vie.

Il est difficile de remercier nommément toutes les personnes qui m'auront inspirée, motivée et soutenue mais elles sont nombreuses ! De tout cœur j'adresse un grand merci à toutes et à tous.

Contents

Chapter 1

Introduction

1.1 Motivation

European eels (Anguilla anguilla) undertake a ±5000-km spawning migration from Europe to the Sargasso Sea although they do not feed during the migration. Indeed swimming organisms at large have refined their senses, morphologies, gaits and mechanical properties to effectively propel and maneuver in a variety of unsteady flow conditions. If one wants to fully uncover the mechanisms at play in Fluid-Solid Interactions, a good understanding of biological locomotion is needed.

The thorough comprehension of biological locomotion in fluids promises enhanced performance in a range of engineering applications from underwater vehicles to energy harvesting devices, e.g. for capturing energy contained in the sea waves. The interplay between sensing and musculoskeletal architectures only started to be uncovered by biologists and engineers alike [1]. This interest has spurred a number of research efforts in recent years. From an experimental perspective, biological observations have been complemented by an increasing number of robotic platforms to test biological hypotheses, designs, and actuation schemes [2, 3]. At the intersection of these disciplines lies the recent foray into the development of hybrid robotic-biological systems with the development of a tissue-engineered ray [4].

Through this thesis, we want to lay the foundations for the deep understanding of Fluid/Solid Interactions (FSI) by reproducing anguilliform swimming propulsion. This method will be focused on dynamic interactions between the swimmer and a fluid. In particular, we focus on two types of problem corresponding to different requirements, namely inverse and direct dynamics, see Fig. 1.1. Inverse dynamics consists in computing the actuation efforts - e.g. provided by the muscular system - that correspond to an "observed" set of body deformations. In other words, it computes the joint torques corresponding to an observed movement within a fluid. In contrast, direct dynamics consists in computing the body deformation resulting from a prescribed set of joint efforts, potentially generated by the muscles. In other words, it computes the trajectory followed by the body under a given actuation pattern and the resulting fluid reactions.

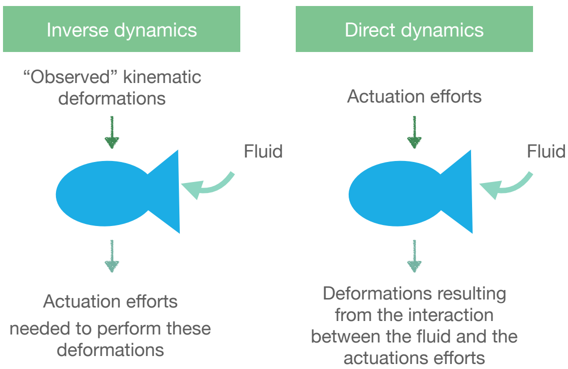

Figure 1.1: Illustration of the concept of inverse and direct dynamics.

This will allow to study a virtual (anguiliform) swimmer interacting with a fluid, if we impose either its deformation or its actuation efforts, thus providing a multipurpose tool. In this text, the word efforts refers to linear forces and torques applied on the various degree of freedom of the swimmer : if linear, forces are used; if rotational, torques are used. Torques are the rotational equivalent of linear force denoted $\boldsymbol{\tau}$.

The proposed framework is based on Vortex Particles Mesh method (VPM) that have the advantage to include perturbations in the flow and thus to capture more complex interactions. For example, disturbances in the fluid can come from external flows, from the wake of other swimmers or other objects wake subject to a flow (e.g. a stone in a river), etc. VPM method is used to solve the Navier-stokes equations in their velocity-vorticity formulation. The resolution, as illustrated in Fig. 1.2, is done on a uniform mesh that is discretized into particles to perform the advection part of the Navier-stokes equations then remeshed onto the uniform mesh to perform the rest of the resolution.

The first objective of this thesis is to develop a VPM method that includes dynamic interactions between an articulated structure with non-overlapping rigid bodies and the fluid around it, see Fig. 1.3. This

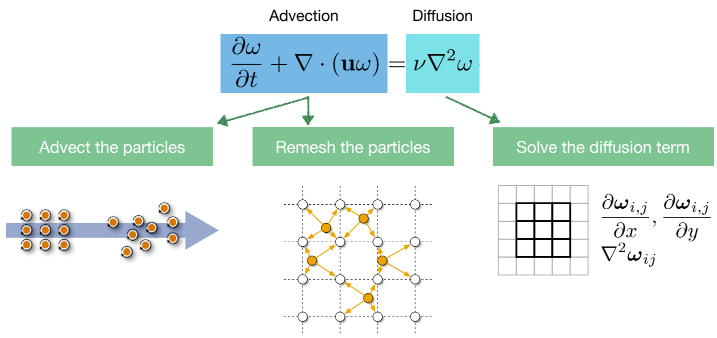

Figure 1.2: Resolution diagram of the velocity ($\mathbf{u}$)-vorticity formulation of the Navier-Stokes equations : $\mathbf{u}$ the velocity field, $\boldsymbol{\omega}$ the vorticity field, and ν the viscosity of the fluid. The advection of the fluid is solved by creating particles and then transport them due to the velocity field in the flow. The diffusion is done by solving the Poisson equation on a uniform grid where the particles have been remeshed. [5, 6].

allows dealing with the complex dynamic exchange in between the fluid and the solid structure. This solid structure will be described with a Multi-Body System. Multi-Body System (MBS), i.e. a framework from solid mechanics used for modeling the dynamic behavior of interconnected rigid or flexible bodies, each of which may undergo large translational and rotational displacements.

The second main objective of this work is to upgrade the VPM method again to continuous articulated structures interacting with fluid, see in Fig. 1.3.

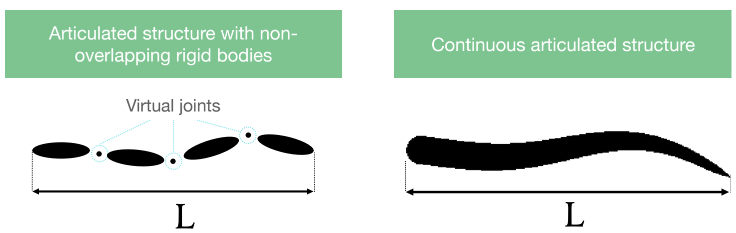

Figure 1.3: Swimmers body definition: the body in first part of the work is shown on the left, articulated structure with non-overlapping rigid bodies and virtual joints, and for the second part of the work, on the right, continuous articulated structures.

1.2 Research questions

In this dissertation, the following research questions will be investigated, questioning the ability of the VPM method to capture the dynamics of fluid/solid interactions :

- *Is VPM method suited to retrieve the hydrodynamic efforts (forces and moments) applied to a fixed or moving, deformable or rigid body ?*

  The quantification of hydrodynamic efforts has never been studied in the framework of vortex methods. Indeed, the dynamic interaction in this method is based on the exchange of momentum for a body with prescribed kinematics [5, 7]. In this case, there is no need to describe the forces and moments involved in the motion. Ultimately, this does not allow an approach based on coupled dynamics. Indeed, the deformation of the body should in this case be the result of the interaction of the hydrodynamic forces with the actuation forces produced by the body. This would be useful in the complex study of articulated systems continuously interacting with a fluid.

- *Can these efforts be introduced in an actuation scheme described by means of a multi-body system governing the deformation and motion of articulated rigid bodies in a fluid?*

  The hydrodynamic forces described above are used to increase the simulation possibilities within the numerical simulation code. This kind of interaction between a fluid and an articulated structure has only been simulated in the literature by using simplified methods to describe the reaction of the fluid [8, 9]. By explicitly using the vortex method, we introduce an advanced resolution software that captures the effect of the fluid as well as to introduce easily disturbances in the flow. This will allow to study flow sensing strategies in complex environments, such as in the wake of other fixed objects or articulated structures.

- *Can this method recover the actuation forces of a continuous deforming body in a fluid?*

  Another interesting field is the study of biological movements. Indeed, living organisms have already refined their ability to be optimal in certain situations: be silent, fast, efficient, move in a complex environment,... [10] All these abilities are the key to better understand the mechanisms at play in the interaction with a fluid. This is why this method offers the potential to study in more depth these propulsion movements that have been described kinematically through biological observation. As consequence, it is possible to extract actuation moments necessary to reproduce the same deformation pattern as well as hydrodynamic moments, and ultimately enables to compute the efficiency or the power needed for propulsion.

- *Can this method be used to create a dynamic control scheme for an articulated continuous body moving in a fluid?*

  In order to close the loop, applying the moments of actuation extracted from a specific kinematic on a continuous articulated structure would allow to reproduce the same specific kinematic previously observed. This will allow to study in a more thorough way the effect of the moments on the state of the system as well as on the surrounding fluid. Ultimately we could create a biologically inspired control schemed reaching the same performance and using the same sensing mechanism as their animal counterpart.

1.3 State-of-the-art

From a theoretical standpoint, the interest in swimming dynamics dates back more than half a century. Theories that consider potential flows include the famous Slender Body Theory (SBT) of Lighthill [11] where slender fish makes swimming movements only in a single direction at right angles to its direction of locomotion. It has been further extended to large amplitude deformation (Large Amplitude Elongated Body Theory, LAEBT) [12], and more recently to inviscid locomotion, in which the viscosity ν of the fluid is equal to zero, by Kanso et al. [13,14]. These approaches entail low computational costs, which allow their implementation into model-predictive control schemes in robotics, see e.g. Boyer et al. [8], Porez et al. [9] and Kelasidi et al. [15].

The shift to a realistic viscous setting and high fidelity simulations entails higher computational costs and, as a consequence, more complex and efficient models. A broad spectrum of direct CFD solvers have been applied to swimming problems: finite differences [16], Lagrangian multipliers [17], viscous vortex methods [18], block lower-upper symmetric Gauss-Seidel [19], Singular-Value Decomposition based Generalized Finite Difference (SVD-GFD) [20], finite volumes [10] and Smoothed Particle Hydrodynamic [21, 22]. In particular, the advantages of vortex methods for the application at hand are the following: the compactness of the working variable (vorticity) and the straightforward treatment of unbounded problems. All of these methods need to deal with two specific challenges (i) handle complex and deforming geometries and (ii) couple the flow problem with the swimmer dynamics in a fluid-structure interaction (FSI) problem.

Two classes of methods can be identified for the first problem. One in which the flow domain accounts for the swimming body in an explicit manner; this has been widely used with unstructured grids that deform and track the boundaries of the swimmer (Arbitrary Lagrangian Eulerian methods–ALE [23]). The second class gathers techniques where the boundaries are represented implicitly and have to be accounted for through either an additional force term in the momentum equations or a modification of the numerical stencil. These include Lagrangian Multipliers [24], immersed interface methods [25], immersed boundary methods [26, 27, 28] and Brinkman penalization methods [29, 30, 31]. Because the present focuses on vortex methods, we overview representative works for these two families: the explicit representation of geometries by Eldredge and colleagues [32] and the penalization techniques of [33, 34] or their more computationally efficient variants in [35]. Penalization - a key methodological concept for this thesis - is defined as a continuous forcing approach that relies on the addition of a mathematical artifact inside the Navier-Stokes equations to impose the boundary condition. It impose the inner boundary condition defining the body via a Lagrangian relaxation of the body constraint.

This first classification actually also influences the choice of the coupling technique for the second challenge: the FSI problem. Deforming grids favor the computation and integration of the stresses at the wall, which then allows to perform the fluid-structure coupling either in a weak or strong formulation [10,32]. The implicit geometry representation of immersed boundary and penalization techniques will be more predisposed to a coupling based on a computation of the net momentum exchange between the fluid and the solid, which can be performed through a projection step as in [36] and also in [5, 33, 37] in the context of vortex methods. We note that the contribution in [37] handles the interaction between the fluid and the articulated structures through a strong coupling, which accurately captures added mass effects and linkage constraints at the cost of a few iterations per time step. We also mention the related effort of Cottet and Maitre [38] for computing the interaction between a flow and elastic membranes through elastic energy, itself based on the level-set discretization of the membrane.

Almost all these efforts have considered the swimming kinematics to be known a priori, and thus have applied the FSI coupling to the swimmer as a whole, i.e. for the recovery of its rigid motion components. Very few numerical works have included the resolution of the swimmer internal dynamics and more specifically, the actuation needed to execute the desired swimming kinematics, i.e. the constraint efforts to enforce a desired kinematics. These exceptions concern the simplified analytical tools developed for the real-time control of robotic platforms in [8, 9], which cannot account for possible perturbations in the flow such as turbulence, large scale structures shed by an obstacle, or the wakes of other swimmers. To the best of our knowledge, there is only one previous work that handled analytical fluid dynamics resolution for the control of underwater snake robots in the presence of constant irrotational currents of unknown direction and magnitude [39]. However, more complex fluid structures cannot be captured by this framework. This context contributes to the rationale behind the present extension of vortex methods as those already combine computational efficiency, even past complex deforming geometries, and the ability to handle complex inflow perturbations.

The accurate numerical simulation of propulsive actuation strategies in complex flow scenarios constitutes a necessary capability towards uncovering the interplay between flow, sensing and gaits, in order to develop rational design of engineering applications. Indeed experimental studies have shown, using a robot, that hydrodynamic force feedback loops and redundancy of peripheral and central mechanisms of generating propulsion motion produce robust swimming. In order to deliver hydrodynamic force feedback, they used a custom designed robot with dedicated distributed hydrodynamic force sensing modules on its outer surface [40]. Other experimental results showed that flapping kinematics of hydrofoils swimming in tandem can be used to control stable locomotion within wakes. Flow interactions arising between them provide a mechanism which promotes group cohesion and prevent collisions [41].

Schooling of fish is also a great example of exploiting the wake and how sensing is a key mechanism of swimming. In [42], VPM method with imposed kinematics is used in combination of Reinforcement Learning to study schooling-like interaction mechanisms. The results confirm that fish may harvest energy shed in vortices and support the conjecture that swimming in formation is energetically advantageous.

The present work aims at providing a global approach for handling potentially complex and large perturbations in the environment of the swimmer. To that end, we develop a computational framework that unifies the treatments of the flow and of the swimmer. Specifically, we extend the methodology introduced by Coquerelle et al. [33] and further developed by Gazzola et al. [5] to allow the kinematics of the actuated device to be solved along with the fluid dynamics. The proposed approach retains the penalization/projection steps of the original works but deploys them in a more general fashion, which allows the extraction of hydrodynamic efforts. These efforts can then be seamlessly integrated into a Multi-Body System (MBS) solver. For complicated structures, kinematic constraints (e.g. rotational joints, linear rails, *etc*) can be enforced exactly by the MBS solver. This waives the use of a stiff forcing term in the flow equations and actually relaxes the stability and accuracy constraints on the time integration within the flow solver.

A central component of the proposed scheme is the computation of the hydrodynamic forces and moments on the individual device components based on information from the penalization and projection approaches. The method thus avoids the computation of local wall stresses and their subsequent integration. Incidentally, we note that the recovery of wall stresses in vortex methods has always been challenging. It indeed entails the evaluation of vorticity at the wall, i.e. in a region of high gradients, and the solution of a specific Poisson equation for the pressure at the wall. Verma et al. [43] used the same FSI-enabled VPM method of [5, 33] as in the present work, together with such a local wall stress computation, in order to calculate the power required for locomotion. The present approach can thus be seen to save one Poisson solution compared to Verma et al. [43] but at the cost of recovering integrated forces only.

1.4 Overview

The developments leading to the coupling methodology for continuous actuated structure will be progressively introduced in this manuscript.

The existing VPM solvers are mainly designed to study prescribed kinematic movements, whereas we want to develop a computational framework that unifies the treatments of the flow and of the swimmer. As a consequence, the first main objective of this work is to develop a VPM method that handles dynamic interactions between a fluid and an articulated structure. This allows dealing with the complex dynamics exchange between fluid and solid structure that is described with a multi-body system. The first two chapters will be devoted to this effort:

- **Chapter 2** presents the elements allowing to extend the VPM method coming from Gazzola et al. [5] that enables only prescribed deformation with an FSI coupling based on projection and penalization techniques. The hydrodynamic effort computation and the multi-body system resolution are presented and included in a new algorithm of resolution. The developments lead to a solver capable of performing accurate simulations of articulated structure with rigid bodies that do not collide with each other in an unbounded domain.

- **Chapter 3** presents a verification of numerical accuracy of our method by reproducing several benchmarks [5, 32, 44, 45]: sedimentation of a 2D cylinder, comparison with the vorticity-based control volume approach of Noca, flow past an elastically mounted cylinder, free swimming of an articulated fish, and its passive locomotion in the wake of a cylinder.

In the two next chapters, we focus on applying our method to concrete ecological situations where energy can be harvest from the vortical structure of the environment : a specific harvesting structure and a swimmer subjected to an incoming perturbed flow. More specifically,

- **Chapter 4** will be devoted to the application of the present framework to an eel-like energy harvester lying in the wake of a cylinder. The harvester is composed of springs and dampers in order to capture energy in the flow. The damping values will be optimized through several simulations in order to find the most efficient combination in term of energy gathered. Finally an harvester with individually-tuned dampers will be investigated.

- **Chapter 5** presents the development of a controller that allows a swimmer to draft behind an obstacle. Three different controllers are presented for three wake situations: no wakes, the wake of a stationary cylinder and the wake of a cylinder with sinusoidal vertical motion. In each situation, the swimmer manages to self-stabilize and we show that the presence of a wake in these cases reduces the cost of swimming.

The content of the chapter 2, 3 and 4 was published as a journal article entitled "Simulations of propelling and energy harvesting articulated bodies via vortex particle-mesh methods" [46]. It is essentially reproduced here as it was published with some additional developments presented in the last section of Chapter 4. The content of chapter 5 was published as a conference article entitled "Numerical Simulations and Development of Drafting

Strategies for Robotic Swimmers at Low Reynolds Number" [47]. Again it is essentially reproduced here as it was published with some additional changes that will be discussed in the conclusion of this chapter.

The second main objective of this work is to upgrade the VPM method developped in Chapter 2 to continuous articulated structures interacting with fluid (see Fig. 1.3). The last two chapters focus on this effort:

- **Chapter 6** addresses the verification of the previously established interaction forces and moments on a continuously deformable body with a non-solenoidal deformation velocity field. To do this, we take the original formulation of Gazzola et al. [5] and modify it so that the global dynamics of the body is governed by Newtonian equations of motion. This allows to artificially slice the body in order to extract the hydrodynamic efforts that are compared to the reference work of Verma [43]. We also show that this method can as well extract the actuation efforts.

- **Chapter 7** presents the elements allowing to extend the first VPM method only capable of simulating discontinuous structures to continuous ones. The new algorithm is presented and we show that it is capable of re-producing a specific swimming gait based on the actuation extracted in the previous chapter via an imposed kinematic simulation. Finally, we show the new capabilities of this method via a global swimming simulation.

The developments and results obtained during this doctoral thesis were communicated to the scientific community through oral presentations in different international conferences [47, 48, 49, 50] and through a journal paper [46].

Chapter 2

A Vortex Particle-Mesh method for articulated rigid bodies

This chapter presents the implementation of a Vortex Particle-Mesh (VPM) method capable of simulating actuated rigid bodies structures in fluids. The present approach builds upon the method developed in [5], and crucially extends it. The efficiency of the methodology relies on the use of an underlying grid describing the body; it allows the use of a FFT-based Poisson solver to calculate the velocity field. We recall that this method in its original form can only handle the interaction between a flow and an object whose deformations are prescribed; it is then the total linear and angular momenta of the object that are solved for. The proposed extension allows for the treatment of a system of articulated rigid bodies the deformations of which are unknown a priori, and are recovered by solving its internal dynamics.

A change has been made with respect to the algorithm presented in the corresponding published article [46]: the projection step no longer explicitly includes the resolution of the free flow through advection, diffusion and the resolution of the Poisson equation in order to obtain the velocity field. This very computational step has been removed as it was superfluous. The algorithm comes back to the original method where the projection is hidden in the Gudunov splitting as the fluid is free to evolve through advection and diffusion step. All the result in this manuscript were recomputed with this modification in the algorithm and no significant deviations with respect to the previously published results were observed.

In Sections 2.1 to 2.3, we briefly present the original algorithm of [5] in terms of its components : a vorticity-based flow solver, the enforcement of wall boundary condition and handling of the fluid-structure interaction via the Brinkman penalization and a projection technique. Further details about its implementation are provided in [5]. In Section 2.4, we describe the handling in the new algorithm of the articulated body via a multi-body approach and extract the hydrodynamic efforts from the VPM method.

2.1 The Vortex Particle-Mesh method

Both the original work and the present extension rely on a Vortex Particle-Mesh (VPM) method. The incompressible flow past the deforming objects is solved using the velocity ($\mathbf{u}$)-vorticity ($\boldsymbol{\omega} = \nabla \times \mathbf{u}$) formulation of the Navier-Stokes equations (i.e. $\nabla \cdot \mathbf{u} = 0$)

$$\frac{D\boldsymbol{\omega}}{Dt} = (\boldsymbol{\omega} \cdot \nabla)\,\mathbf{u} + \nu \nabla^2 \boldsymbol{\omega} \tag{2.1}$$

$$\nabla \cdot \mathbf{u} = 0 \tag{2.2}$$

where $\frac{D}{Dt} = \frac{\partial}{\partial t} + \mathbf{u} \cdot \nabla$ denotes the Lagrangian derivative, $\mathbf{u}$ is the velocity field, $\boldsymbol{\omega}$ the vorticity field and ν the kinematic viscosity. The velocity field is recovered from the vorticity by solving the Poisson equation

$$\nabla^2 \mathbf{u} = -\nabla \times \boldsymbol{\omega}\,. \tag{2.3}$$

The advection of vorticity is handled in a Lagrangian fashion using particles, as schematize in Fig. 1.2, characterized by a position $\mathbf{x}_p$, a volume V_p and a vorticity integral $\boldsymbol{\alpha}_p = \int_{V_p} \boldsymbol{\omega} d\mathbf{x}$

$$\frac{d\mathbf{x}_p}{dt} = \mathbf{u}_p \tag{2.4}$$

$$\begin{aligned} \frac{d\boldsymbol{\alpha}_p}{dt} &= \int_{V_p} (\boldsymbol{\omega} \cdot \nabla)\mathbf{u} + \nu \nabla^2 \boldsymbol{\omega} d\mathbf{x}\,, \\ &= \left[(\boldsymbol{\omega} \cdot \nabla)\mathbf{u} + \nu \nabla^2 \boldsymbol{\omega} \right]_p V_p \end{aligned} \tag{2.5}$$

where we identify the roles of the velocity field in the advection (Eq. (2.4)), and of the vortex stretching and diffusion for the evolution of vorticity (Eq. (2.5)). The stretching term is omitted in the remainder of this article because it is identically equal to zero in a two-dimensional setting. The diffusion part of (2.1), illustrated in Fig. 1.2, is efficiently evaluated on a regular mesh [51]. The diffusion operator uses second order centered finite difference schemes. The Poisson solver operates in Fourier space for unbounded domain. To this end, information is made available on the mesh, and retrieved from the mesh, by interpolating back and forth between the particles and the grid using high order interpolation schemes. Advantageously, this hybridization does not affect the good numerical accuracy (in terms of diffusion and dispersion errors) and the stability properties of a particle method [52]. The method adapts the time step according to the diffusion Fourier number defined by $\Delta t \leq \frac{h^2}{2\nu}$ and to a Lagrangian CFL condition (LCFL) for the explicit time integration of advection [53], e.g. $\Delta t < \mathrm{LCFL}/\|\nabla \mathbf{u}\|_{\max}$. Additionally, imposing $LCFL < 1$ prevents particle trajectories from crossing each other.

2.2 Brinkman penalization

The immersed objects are described by mollified characteristic functions, χ_s (see A.1 for more details). Each of these functions is built upon a level set function that specifies the signed distance to the surface of the body, d. This geometric information is carried by a specific deformable grid associated with the object, and the resulting color function is interpolated onto the regular computational mesh (see [5] for further details).

The no-slip boundary condition enforcement is achieved by means of the Brinkman penalization technique (for a detailed proof of convergence see [54]). This approach extends the fluid domain into the solid region and thus considers the fluid and solid as a global continuous domain Υ, combining the solid domain Ω and the fluid domain Σ. The approximation of the no-slip boundary condition is achieved by extending the momentum equation with a term that drives the fluid velocity $\mathbf{u}$ inside the solid region to a prescribed body velocity $\mathbf{u}_s$. The penalized Navier-Stokes equations then read

$$\frac{D\mathbf{u}}{Dt} = -\frac{1}{\rho}\nabla p + \nu\nabla^2\mathbf{u} + \lambda\chi_s(\mathbf{u}_s - \mathbf{u}),\ \mathbf{x} \in \Upsilon \tag{2.6}$$

where $\lambda \gg 1$ is the penalization factor and $\lambda\chi_s(\mathbf{u}_s - \mathbf{u})$ is the penalization term. The value of λ can be fixed arbitrarily, this directly governs the error in the penalized solution: $\|\mathbf{u} - \mathbf{u}_\lambda\| \leq C\lambda^{-1/2}\|\mathbf{u}\|$, as shown in [55]. A larger value enforces the wall boundary condition more strictly, although at the cost of a stiffer term that needs to be integrated in time.

By taking the curl, we obtain the corresponding penalized velocity-vorticity formulation,

$$\frac{D\omega}{Dt} = (\omega \cdot \nabla)\mathbf{u} + \nu\nabla^2\omega + \frac{1}{\rho^2}\nabla\rho \times \nabla p + \lambda\nabla \times (\chi_s(\mathbf{u}_s - \mathbf{u})) \tag{2.7}$$

where we identify the additional terms (with respect to Eq. (2.1)) related to the baroclinic generation of vorticity and the penalization. The baroclinic generation of vorticity will appear in the case of a fluid with a space-varying density. In the present work, the density is considered uniform across the fluid and the solid bodies as we leave the handling of any density difference to the MBS solver. This treatment is allowed by the fact that the effects of a density difference can be well-identified; they are twofold and consist of inertial and gravity effects. On the one hand, inertial effects are treated by the use of the specific body density in the integration of the body dynamics by the MBS solver, as discussed in Section 2.4.2. On the other, the effect of a gravity force can be isolated as it generates a constant hydrostatic pressure gradient in the fluid. In the case of a density difference, this gradient in turn generates a constantly active baroclinic vorticity generation term at the fluid-body interface, which is equal to the buoyancy force. This means that the buoyancy force can be computed exactly as $(\rho_s - \rho_f)V_s\boldsymbol{g}$ and be simply added to the forces that need to be treated by the MBS. It is worth mentioning that such a treatment is also followed in the Immersed Interface Method (IIM) in velocity-pressure formulation of Xu and Wang [56].

2.3 Projection technique

The projection technique captures the effect of the fluid on the solid body. At each time step, the fluid evolves freely over the whole domain – i.e. like if no body was there – according to the current velocity field. The momentum acquired by the footprint of the body on the domain correctly captures the flux of momentum between the fluid and the body (for detailed proof see [36]). The captured flux of momentum allows to recover the correct body velocity, which is then used in the penalization step to make the flow field consistent again. The body velocity is then composed of the translational, and rotational velocity, u_T and u_R described as follows

$$
\begin{aligned}
\mathbf{u}_T &= \frac{1}{M_s}\int_\Omega \rho\chi_s \mathbf{u}\, d\mathbf{x}, &(2.8)\\
\dot{\theta} &= \frac{1}{J_s}\int_\Omega \rho\chi_s (\mathbf{x}-\mathbf{x}_{cm})\times \mathbf{u}\, d\mathbf{x}, &(2.9)\\
\mathbf{u}_R &= \dot{\theta}\times(\mathbf{x}-\mathbf{x}_{cm}), &(2.10)
\end{aligned}
$$

with M_s the mass of the body, J_s the inertia taken at the center of mass of the body and $\mathbf{x}_{cm}$ the center of mass of the body.

This original algorithm does not explicitly provide the efforts applied to the body but rather their time integral over a time step, i.e. the changes in linear and angular momenta. Unlike the approach of Eldredge [45], this approach does not treat the added mass effects implicitly. It thus exhibits a lower convergence in the capture of forces produced by the acceleration of the bodies, as investigated in [5]. Additionally, the body has prescribed kinematics and the solver does not provide any information about the actuation required to achieve that motion.

2.4 Extension to an articulated system

We here modify the method presented in Sections 2.1 to 2.3 in order to treat an articulated system of solid elements with embedded actuation. This entails the computation of hydrodynamic forces and moments on each element of the structure to solve the dynamics of the degrees of freedom related to the multy-body joints. In this section, we detail and discuss the components of this extension: the description of the articulated structure, the multi-body system (MBS) solver and the computation of the hydrodynamic efforts from the penalization (Section 2.2) and projection (Section 2.3) schemes.

2.4.1 Free articulated system

We focus on a two-dimensional MBS composed of N linked rigid bodies, here elliptical elements, immersed in a fluid (Fig. 2.1, $N = 3$) and connected by means of rotational joints, being here virtual. Each joint entails a degree of freedom that is represented by a generalized coordinate q_i, i.e. the angle between two successive elements. The three first coordinates, q_1, q_2, q_3, (2 linear and 1 rotational coordinates) describe the floating base, providing the global structure with the three translational and rotational degrees of freedom related to the x, y plane. The

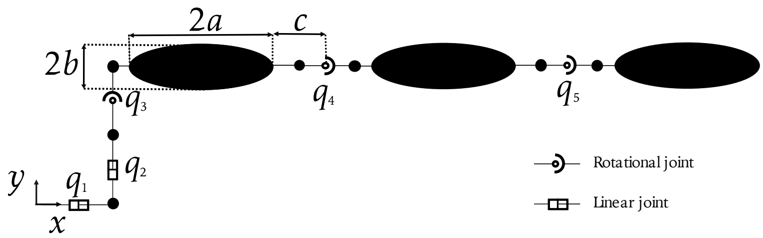

Figure 2.1: Multi-body diagram of three segmented two-dimensional eel-like structure: floating base generalized coordinates, q_1, q_2, q_3, and the joints generalized coordinates, q_4, q_5; $2a$ the length, $2b$ the width and c the distance from the tip to the hinge joint of each element.

articulated structure is then described by the generalized coordinates: $\mathbf{q} = [q_1\ q_2 ...\ q_n]^T$, with $n = N + 2$. The footprint of the structure in space is then described by a set of characteristic functions, $\chi_{s,j}$, each one representing an elliptical element j, as in Eq. (A.1).

2.4.2 Multi-body dynamics equations

In this section, we establish the dynamic equations governing for the actuated structure. The linear and angular velocities of each body j, $\mathbf{v}_{c,j}$ and $\omega_{c,j}$, are measured with respect to its center of mass and are computed from the generalized coordinates as

$$\begin{aligned} \mathbf{v}_{c,j} &= \mathbf{J}_{v,j}(\mathbf{q})\dot{\mathbf{q}} && (2.11)\\ \omega_{c,i} &= \mathbf{J}_{\omega,j}(\mathbf{q})\dot{\mathbf{q}} && (2.12) \end{aligned}$$

where $\mathbf{J}_{v,j}(\mathbf{q})$ and $\mathbf{J}_{\omega,i}(\mathbf{q})$ are the Jacobian matrices associated into the linear and angular velocities, respectively. Following a classical approach from robotics, we derive the governing equations for the whole system dynamics through the Euler-Lagrange formalism. The complete dynamic system is then described by the following matrix equation, derived in [57]

$$\mathbf{D}(\mathbf{q})\ddot{\mathbf{q}} + \mathbf{C}(\mathbf{q}, \dot{\mathbf{q}})\dot{\mathbf{q}} = \boldsymbol{\tau}. \tag{2.13}$$

$\mathbf{D}(\mathbf{q})$ is the inertia matrix:

$$\mathbf{D}(\mathbf{q}) = \sum_{j=1}^{N} \left\{ m_i \mathbf{J}_{v,j}^T \mathbf{J}_{v,j} + \mathbf{J}_{\omega,j}^T \mathbf{R}_j(\mathbf{q}) \mathbf{I}_j \mathbf{R}_j^T(\mathbf{q}) \mathbf{J}_{\omega,i} \right\} \tag{2.14}$$

where we dropped the explicit dependencies on $\mathbf{q}$ of the matrices $\mathbf{J}_{v,j}$ and $\mathbf{J}_{\omega,j}$ for the sake of clarity. The mass of body j and its inertia about a frame fixed to its center of mass are denoted m_j and $\mathbf{I}_j$, respectively; $R_j(\mathbf{q})$ is the rotation matrix capturing the body orientation with respect to the inertial frame. The matrix $\mathbf{C}(\mathbf{q},\dot{\mathbf{q}})$ gathers the Coriolis and centripetal term; its elements are given by

$$C_{lm} = \sum_{i=1}^{n} \frac{1}{2} \left\{ \frac{\partial D_{lm}}{\partial q_i} + \frac{\partial D_{li}}{\partial q_m} - \frac{\partial D_{im}}{\partial q_l} \right\} \dot{q}_i \, . \tag{2.15}$$

$\boldsymbol{\tau}$ is the effort applied in each joint $(q_1, q_2, \ldots, q_{N+2})$ and is defined as

$$\boldsymbol{\tau} = \boldsymbol{\tau}_{\text{hyd}} + \boldsymbol{\tau}_{\text{act}} \tag{2.16}$$

where $\boldsymbol{\tau}_{\text{hyd}}$ is the equivalent force for q_1 and q_2 or torque for $q_3, \ldots, q_{N+2}$ due the hydrodynamic forces and torques applied to the elements and $\boldsymbol{\tau}_{\text{act}}$ is the actuation effort transmitted by the body, see figure 2.2 for a graphical representation. For a rotational joint i, τ_i represents the applied torque and for a linear one, it is the force collinear to the joint direction.

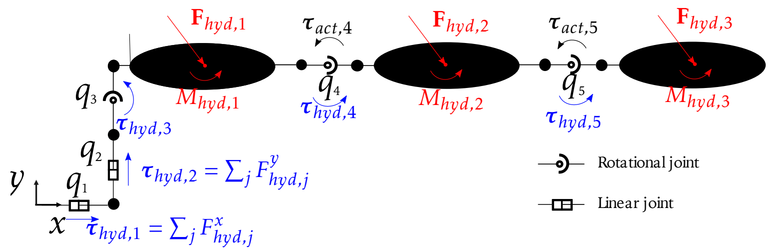

Figure 2.2: Multi-body diagram of three segmented two-dimensional eel-like structure: floating base generalized coordinates, q_1, q_2, q_3, and the joints generalized coordinates, q_4, q_5; $2a$ the length, $2b$ the width and c the distance from the tip to the hinge joint of each element.

2.4.3 Fluid-structure interaction efforts

We now derive the extraction of the hydrodynamic efforts $\boldsymbol{\tau}_{hyd}$ on the structure elements. The original method (Appendix A) solves the FSI problem through the combined use of penalization and projection techniques. As a result, the resulting approach does not explicitly compute the forces exerted on the immersed bodies.

A first departure from the original technique concerns the extension of the flow field inside the solid structure. The fluid properties will be taken as uniform, with viscosity and density values ν, ρ_f everywhere, unlike the original spatially-dependent quantities of Eq. (A.2). This is motivated by the fact that the whole dynamics of the solid will be handled explicitly by the MBS solver through the hydrodynamic forces $\boldsymbol{\tau}$ in Eq. (2.13). The extended domain simply provides a support for the computation of rates of momentum transfer, as shown below.

We recover the hydrodynamic forces and moments from the penalization and projection steps, as shown in B:

$$\mathbf{F}_{\text{hyd},j} = \frac{d}{dt}\int_{\Omega_{mat,j}} \rho_f \mathbf{u}\, dV + \int_{\Omega_j} \rho_f \lambda \chi_s (\mathbf{u}-\mathbf{u}_s)\, dV \tag{2.17}$$

$$\mathbf{M}_{\text{hyd},j} = \frac{d}{dt}\int_{\Omega_{mat,j}} \rho_f \,(\mathbf{x}\times\mathbf{u})\, dV + \int_{\Omega_j} \mathbf{x}\times(\rho_f \lambda \chi_s (\mathbf{u}-\mathbf{u}_s))\, dV \tag{2.18}$$

The resulting efforts, $\mathbf{F}_{hyd}$ and $\mathbf{M}_{\text{hyd}}$, are each composed of two terms. The first term is associated with the projection step, since the projection scheme effectively performs the time integration contained in this term. Conversely, the present approach will perform the evaluation of the time derivatives of these volume integrals. The second term is straightforwardly identified as the contribution due to the penalization technique. Note that the moment $\mathbf{M}_{\text{hyd}}$ is computed with respect to the origin frame of reference (x,y) ; it still needs to be translated to each body center of mass $\mathbf{x}_{\text{cm}}$ through $\mathbf{M}_{\text{hyd, cm}} = \mathbf{M}_{\text{hyd}} - \mathbf{x}_{\text{cm}} \times \mathbf{F}_{\text{hyd}}$ in order to be used in the MBS solver (Section 2.4.2).

The uniform density extension has additional consequences. Because the baroclinic term in the vorticity evolution equation (Eq. (2.7)), $1/\rho^2 \nabla\rho \times \nabla p$ vanishes, the efforts of Eqs. (2.17) and (2.18) are missing the hydrostatic component exerted on a body lighter or heavier than the ambient fluid. This component will need to be accounted for within the multi-body system solver through the straightforward addition of corresponding forces and moments, i.e. $\mathbf{F}_{\text{stat},j} = (\rho_s - \rho_f)\, V_j\, \mathbf{g}$ and $\mathbf{M}_{\text{stat},j} = (\rho_s - \rho_f) V_j\, \mathbf{x}_{\text{cm}} \times \mathbf{g}$.

2.4.4 Computational aspects

In the following, we describe the implementation of the above methodology into a full algorithm. We recall that the forces and moments $\mathbf{F}_{\text{hyd},j}$ and $\mathbf{M}_{\text{hyd},j}$ are computed independently for each sub-body. Each element j of the structure then needs to be characterized by a characteristic function $\chi_{s,j}$. For the sake of notation simplicity, the subscript j of the sub-body will be omitted in the remainder of this section. Forces and moments will then have to be understood as the set of forces and moments applied to each system element.

The whole coupled method is summarized in Algorithm 1 and a simplified schematic is presented in Fig. 2.4. The superscript n denotes the evaluation time t^n of fields and variables. We then denote the velocity, vorticity, characteristic function, generalized coordinates, forces, moments and density fields at time t^n as $\mathbf{u}^n$, ω^n, χ_s^n, $\mathbf{q}^n$, $\mathbf{F}^n$, M^n and ρ^n, respectively.

The second order differential equation for the MBS (Eq. (2.13)) is integrated by means of a fourth order Runge-Kutta-Fehlberg method. This method offers error control through an adaptive time step: a local error is estimated from solutions obtained with a fourth and fifth order Runge-Kutta method; the time step is reduced if the error is larger than a threshold value ξ. In this work, we used $\xi = 10^{-6}$ for all simulations. The high order integration of our MBS solver is motivated by its stability region: these systems often present little or zero damping and high stiffness. Additionally, the associated computational overhead is affordable given the limited number of variables in the MBS ($\mathcal{O}(10^1 - 10^2)$).

Step 1: Velocity update The fluid velocity field is recovered from the Poisson equation (Eqs. (2.19) and (2.20)), solved by an unbounded Fourier solver. The time step is constrained by the diffusion Fourier number and the advection CFL condition. Especially the lagrangian CFL condition (2.21) is used in order to control the Lagrangian distortion of particles over a time step due to the remeshing of the particles [53, 58].

Step 2: Projection forces The projection step consists in letting the whole flow (i.e. including the extension inside the body) evolve freely over a part of the time step Δt^n as if the structure was not there. It is done through the use of a Godunov splitting approach in the step 2 of this algorithm where the vorticity field ultimately violates the rigid motion. The resulting velocity field $\mathbf{u}^n$ corresponds to a gain in linear and angular momentum for each element of the immersed bodies. This predicted momentum is used to compute the flux of momentum between two time steps by performing the time differentiation of Eqs. (2.17) and (2.18); these steps correspond to Eqs. (2.22) and (2.23).

Step 3: Solving the MBS The hydrostatic and hydrodynamic torques acting at the joints are obtained through a free body diagram method

Algorithm 1 Coupled Method

WHILE $t^n \leq T_{end}$

Step 1 : Velocity update

$$\nabla^2 \psi^n = -\omega^n \tag{2.19}$$

$$\mathbf{u}^n = \nabla \times \psi^n \tag{2.20}$$

$$\|\nabla \mathbf{u}^n\| \Delta t^n \leq LCFL \text{ and } \Delta t^n \leq \frac{h^2}{2\nu} \tag{2.21}$$

Step 2 : Projection forces

$$\mathbf{p}^{*,n+1}_{proj} = \int_{\Omega_{mat}} \rho_f \chi_s^n \mathbf{u}^{n+1} d\mathbf{x} \quad \text{with} \quad \mathbf{F}^{n+1}_{proj} = \frac{\mathbf{p}^{*,n+1}_{proj} - \mathbf{p}^{*,n}_{proj}}{\Delta t^n} \tag{2.22}$$

$$\mathbf{l}^{*,n+1}_{proj} = \int_{\Omega_{mat}} \rho_f \chi_s^n \, (\mathbf{x} \times \mathbf{u}^{n+1}) \, d\mathbf{x} + \mathbf{x}^n_{cm} \times \mathbf{F}^{n+1}_{proj} \quad \text{with} \quad \mathbf{M}^{n+1}_{proj} = \frac{\mathbf{l}^{*,n+1}_{proj} - \mathbf{l}^{*,n}_{proj}}{\Delta t^n} \tag{2.23}$$

Step 3 : Time integration of the MBS

$$\boldsymbol{\tau}^{n+1}_{stat} = \mathcal{F}(\mathbf{F}^{n+1}_{stat}, \mathbf{M}^{n+1}_{stat}) \quad \text{with} \quad \mathbf{F}^{n+1}_{\text{stat},j} = (\rho_s - \rho_f) V_j \, \mathbf{g} \quad \text{and} \quad \mathbf{M}^{n+1}_{\text{stat},j} = (\rho_s - \rho_f) V_j \, \mathbf{x}_{\text{cm}} \times \mathbf{g} \tag{2.24}$$

$$\boldsymbol{\tau}^{n+1}_{hyd} = \mathcal{F}(\mathbf{F}^{n+1}_{proj} + \mathbf{F}^n_{pen}, \mathbf{M}^{n+1}_{proj} + \mathbf{M}^n_{pen}) \tag{2.25}$$

$\boldsymbol{\tau}^{n+1}_{act}$ provided by a control law

$$D(\mathbf{q})\ddot{\mathbf{q}} + C(\mathbf{q}, \dot{\mathbf{q}})\dot{\mathbf{q}} = \boldsymbol{\tau}^{n+1}_{hyd} + \boldsymbol{\tau}^{n+1}_{act} + \boldsymbol{\tau}^{n+1}_{stat} \tag{2.26}$$

Compute $\mathbf{q}^{n+1}$ and $\dot{\mathbf{q}}^{n+1}$ for $t^{n+1} = t^n + \Delta t^n$

$$\chi_s^{n+1} = \mathcal{G}(\mathbf{q}^{n+1}) \tag{2.27}$$

$$\mathbf{u}_s^{n+1} = \mathcal{H}(\mathbf{q}^{n+1}, \dot{\mathbf{q}}^{n+1}) \tag{2.28}$$

Step 4 : Penalization

$$\mathbf{u}^{n+1}_\lambda = \frac{\mathbf{u}^n + \lambda \Delta t \chi_s^{n+1} \mathbf{u}_s^{n+1}}{1 + \lambda \Delta t \chi_s^{n+1}} \tag{2.29}$$

$$\omega_\lambda = \nabla \times \mathbf{u}^{n+1}_\lambda \tag{2.30}$$

$$\mathbf{F}^{n+1}_{pen} = \int_\Omega \lambda \rho_f \chi_s^{n+1} (\mathbf{u}^{n+1}_\lambda - \mathbf{u}^{n+1}_s) d\mathbf{x} \tag{2.31}$$

$$\mathbf{M}^{n+1}_{pen} = \int_\Omega \lambda \rho_f \chi_s^{n+1} \mathbf{x} \times (\mathbf{u}^{n+1}_\lambda - \mathbf{u}^{n+1}_s) d\mathbf{x} + \mathbf{x}^{n+1}_{cm} \times F^{n+1}_{pen} \tag{2.32}$$

Step 5 : Time integration of the vorticity field

$$\frac{\partial \omega_\lambda}{\partial t} = \nu \nabla^2 \omega_\lambda - \nabla \cdot (\mathbf{u}_\lambda \omega_\lambda) \tag{2.33}$$

$$\omega^{n+1} = \omega^{n+1}_\lambda \tag{2.34}$$

$t^{n+1} = t^n + \Delta t^n$

$n = n + 1$

ENDWHILE

(see Fig. 2.3). They are computed from the applied forces and moments, both hydrostatic (Eq. (2.24)) and hydrodynamic (Eq. (2.25)), through a mapping $\mathcal{F}$. The MBS solver uses these torques and the actuation torques provided by a control law, $\boldsymbol{\tau}_{\text{act}}$, to advance the structure to a new configuration $\mathbf{q}^{\mathbf{n+1}}$.

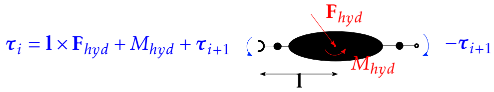

Figure 2.3: Free body diagram of one structure's segment: only the last segment differs as there is no right rotational joint.

This configuration is then translated into a characteristic function that describes the structure shape at t^{n+1}, χ_s^{n+1}. This step is summarized by a mapping function $\mathcal{G}$ in Eq. (2.27). Similarly, the velocity field of the structure is also found through the function $\mathcal{H}$ in Eq. (2.28).

Step 4: Penalization The no-slip condition is enforced at the interfaces approximately through the penalization of the velocity field. A first order implicit Euler time discretization scheme is used see Eq. (2.29). The penalized vorticity is then recovered from the penalized velocity (Eq. (2.30)). The forces due to this constraint are computed via the integration of the penalization term over the body surface via an implicit Euler scheme; these penalization forces, Eqs. (2.31) and (2.32), will be used in step 3 of the next time step.

Step 5: Solving the vorticity field Step 5 describes the vorticity field update. The vorticity field is diffused and advected through Eq. (2.33) with an explicit second order scheme as in the original method [5].

2.5 Conclusion

In this chapter, the elements allowing to combine the VPM solver with a multi-body system solver were presented. The method is simple and efficient, since it does not require the computation of local wall stresses and their subsequent integration. Incidentally, we note that the recovery of wall stresses in vortex methods has always been challenging. It indeed entails the evaluation of vorticity at the wall, i.e. in a region of high gradients, and the solution of a specific Poisson equation for the pressure at the wall [43]. In contrast, the method presented here only involves integrals over the body and it highly reduces the computational cost to evaluate the effort on a solid body.

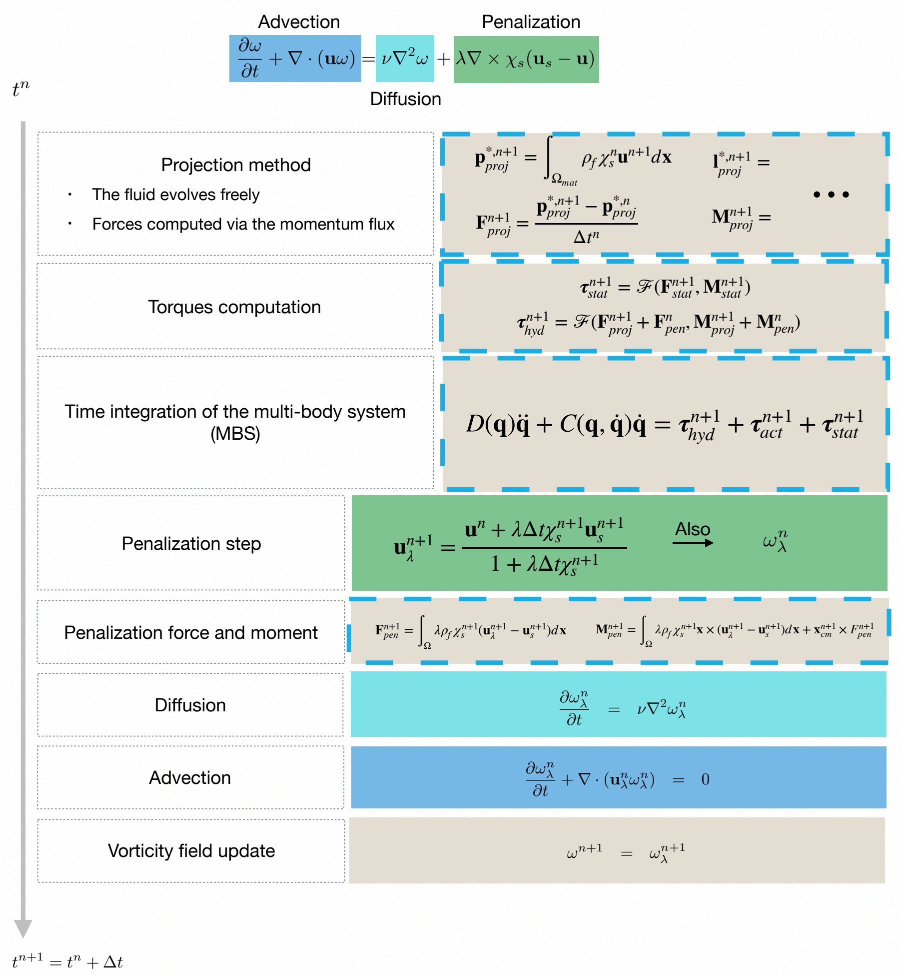

Figure 2.4: Schematic representation of the resolution over one time step of the algorithm : the various steps corresponding to the advection, diffusion and penalization are highlight in color. The blue dashed rectangles show the new step in the algorithm compared to the original method of [5].

Chapter 3

Validation of the methodology

In this Chapter, the coupled methodology will be applied to a series of test cases. We verify that the method is able to recover smooth hydrodynamics efforts and that it can be used in combination with a MBS approach. To do so, several well-documented test cases are reproduced and compared to the performance of competing techniques. These cases include the sedimentation of a 2D cylinder, efforts comparison with Noca formulas, the flow past an elastically-mounted cylinder, the free swimming of an articulated fish, and the passive propulsion of a fish in a wake. We use the case of the elastically-mounted cylinder for a convergence study.

3.1 Sedimentation of a 2D cylinder

We first test the two-way fluid-solid coupling for a rigid body subject to gravity using the case of a falling 2D cylinder. We compare the results to Gazzola et al. [5] and Namkoong et al. [59].

3.1.1 Configuration

A rigid 2D cylinder of diameter $D = 0.005\ m$ and with $\rho_s/\rho_f = 1.01$ is released from rest and accelerates due to gravity ($g = 9.81 m/s^2$), see Fig. 3.1 until it reaches its asymptotic terminal velocity, corresponding to a $Re = 156$ in water ($\nu = 8 \cdot 10^{-7}\, m^2/s, \rho_f = 996\, kg/m^3$). The domain size was set to $[0; 8.75\ D] \times [0; 70\ D]$ discretized by a 1024×8192 grid. The following numerical parameters for VPM and the penalization are used: LCFL $= 10^{-1}$, $\epsilon = 2\sqrt{2}h$, $\lambda = 10^4$ with h being the mesh spacing.

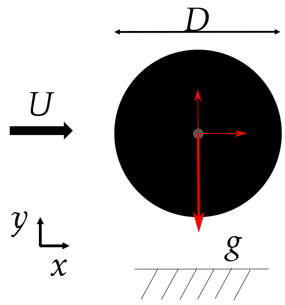

Figure 3.1: Sedimentation of a 2D cylinder: configuration parameters.

This resolution of 117 mesh points per cylinder diameter is similar to the 128 points used in [5].

3.1.2 Results

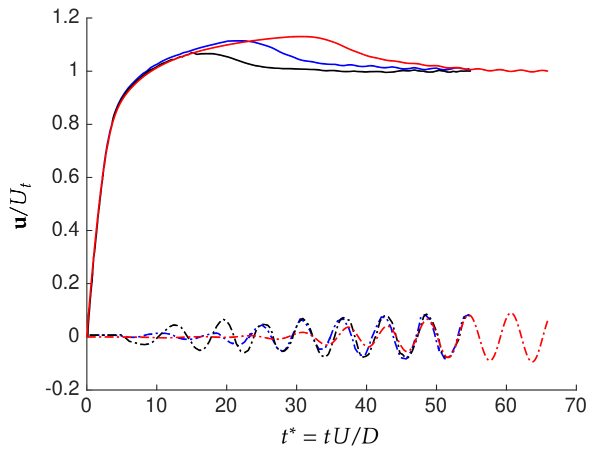

Figure 3.2: Sedimentation of a 2D cylinder: Normalized streamwise velocity u_y/U_t (solid lines) and lateral u_{lat}/U_t (dashed lines); present method (red lines), Gazzola et al. [5] (blue lines) and Namkoong et al. [59] (black lines).

Fig. 3.2 shows the time evolution of the normalized vertical, u_y/U_t, and lateral, u_{lat}/U_t, velocities obtained by the present method and by the references. U_t represents the reference terminal velocity $U_t = 2.501$ cm/s achieved by [59]. Similar dynamics are observed. Specifically, the falling velocity overshoots the terminal velocity and then slows down when the shedding starts. The terminal velocity is seen to differ from the reference by less than 1%. A snapshot of the vorticity around the cylinder is presented at Fig. 3.3. The lateral and angular (not shown) velocities in the steady regime also agree both in amplitude and frequency. The initial transient is triggered by numerical noise when symmetry of the flow is broken. This effect is not controlled and depends on the grid and implementation of the method. This effect explains the delay and overshoot observed for the falling velocity, as well as the transient of the lateral velocity.

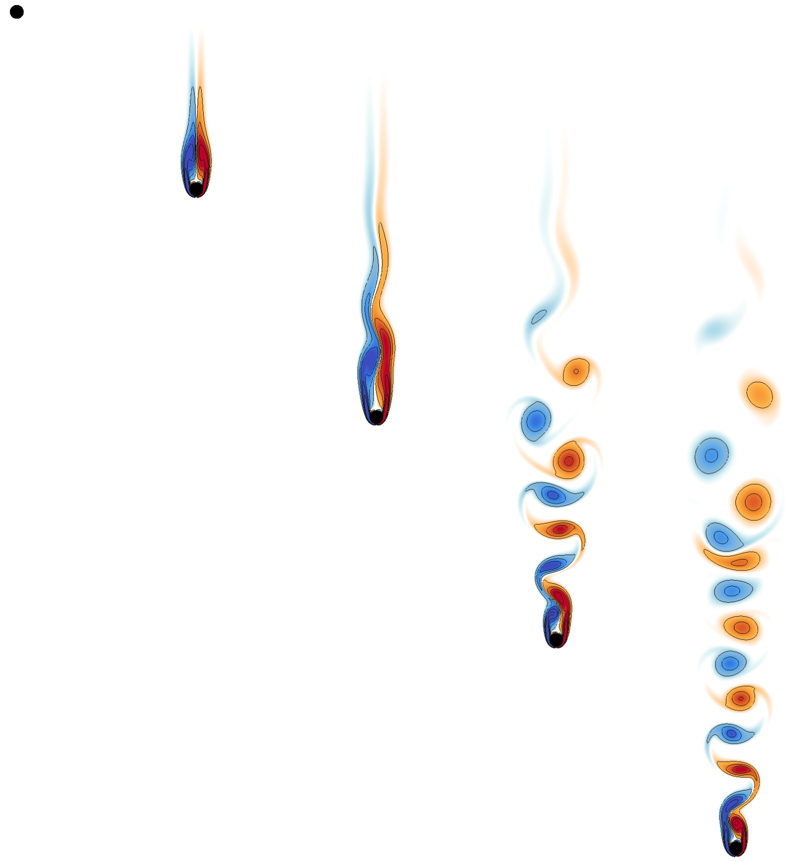

(a) $t^* = 0$ (b) $t^* = 15$ (c) $t^* = 30$ (d) $t^* = 45$ (e) $t^* = 60$

Figure 3.3: Sedimentation of a 2D cylinder: snapshots of the configuration and the vorticity around the cylinder at various $t^* = tU/D$. Dimensionless vorticity contours have values from -15 to 15 in 10 uniform increments with negative and positive vorticity in blue and red respectively.

3.2 Comparison with vorticity-based Noca formulas

In order to compare the two effort calculation methods, the force formula (81) of Noca et al. [60], further developped in [61], was chosen to find the drag and lift of a moving body. We chose to take an example representative of what our method is capable: enforce actuation efforts, compute hydrodynamics efforts and impose kinematic constraints thanks to the MBS solver within the fluid solver.

3.2.1 Configuration

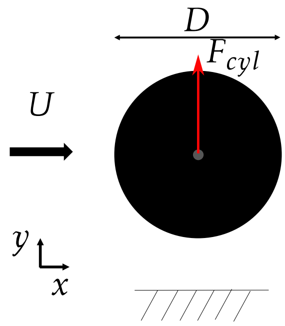

Figure 3.4: Comparison with vorticity-based Noca formulas: configuration parameters.

The setup is composed by a neutrally buoyant cylinder of diameter D with only one degree of freedom, the vertical one in the y direction, immersed in a uniform free stream with a velocity U (see Fig. 3.4). The Reynolds number, based on cylinder diameter and free-stream velocity, is taken to $Re = \frac{UD}{\nu} = 100$. An actuation force F_{cyl} is applied on the cylinder in the free motion direction and is controlled to enforce the cylinder kinematic to follow a sinusoidal movement.

The MBS framework presented in Section 2.4.2 simplifies into an ordinary differential equation for the cylinder position $y(t)$

$$m\ddot{y} = F(t) = F_y(t) + F_{cyl}(t) \tag{3.1}$$

where the mass coefficient is m and the Coriolis and centrifugal effects vanish because of a single actuated degree of freedom. The total force applied to the system $\mathbf{F}(t)$ contains the hydrodynamic force $F_y(t)$ and the actuation force F_{cyl}. The control of the actuation force is done through a Proportional-Derivative controller (PD controller) defined by:

$$F_{cyl}(t) = K_p'(y_{ref} - \mathrm{y}) + K_i'(v_{ref} - v);$$

where $y_{ref} = 0.1\sin(\frac{t}{2})$ and $v_{ref} = 0.05\cos(\frac{t}{2})$ are the reference motion and velocity, and, $K_p' = \frac{K_p}{\rho U^2 D} = 750$ and $K_i' = \frac{K_p}{\rho U D^2} = 50$ are the dimensionless proportional and derivative coefficients.

The simulation uses a computational domain size of [0; 10 D] × [0; 10 D] discretized by a 512×512 grid. The cylinder initial position is located at (3.5 D, 5 D). The following numerical parameters for VPM and the penalization are used: $LCFL = 5.10^{-2}$, $\epsilon = 2\sqrt{2}h$, $\lambda = 1.10^4$.

3.2.2 Results

Fig. 3.5(a), shows the time evolution of the movement followed by the cylinder by the present method compared to the reference motion. The initial transient is due to the parameter of the controller that does not manage to follow exactly the imposed curve due to the value of the coefficient chosen that are not too stiff. The drag coefficient and the lift coefficient are shown on Figs. 3.5(b) and 3.5(c). Similar dynamics are observed compared to the one obtained via the Noca formula. The drag coefficient is subject to small oscillations which is explained by the coarse mesh used for this validation test (see Section 3.3.3 for more insight on the convergence of this method).

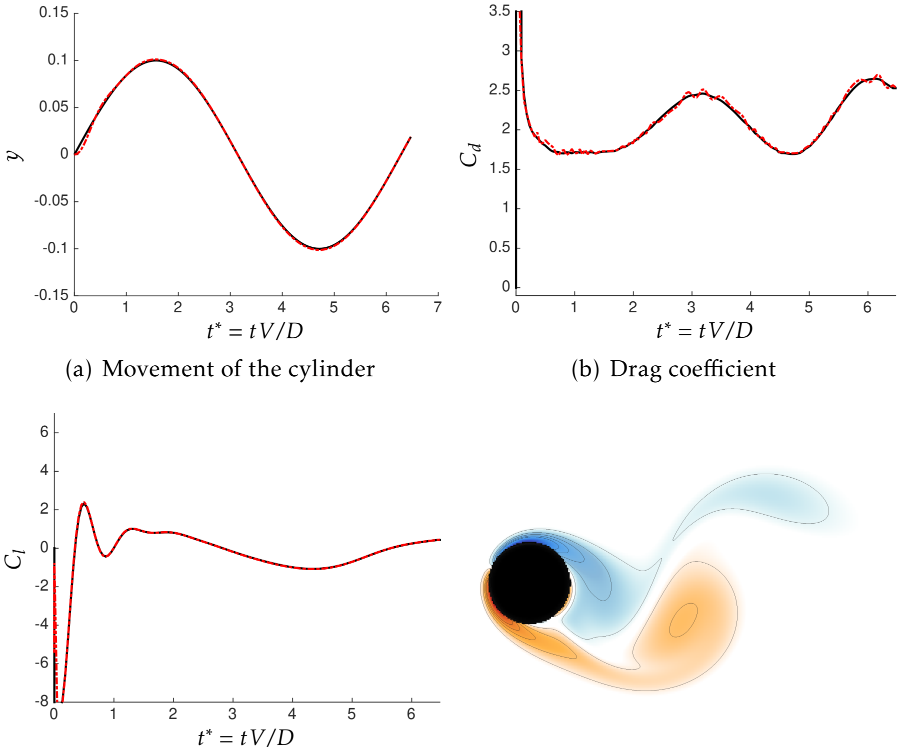

(a) Movement of the cylinder

(b) Drag coefficient

(c) Lift coefficient

(d) Vorticity at $t^* = 6$

Figure 3.5: Forces calculation method comparison on an actuated cylinder: present method (dashed red) and reference movement/force coefficient (solid black). Dimensionless vorticity contours have values from -5 to 5 in 10 uniform increments with negative and positive vorticity in blue and red respectively.

3.3 Flow past an elastically-mounted cylinder

The vortex shedding generated by the flow past a circular cylinder is a quite common study case in fluid mechanics. Here, we focus on the transverse oscillations induced on an elastically mounted circular cylinder (Fig. 3.6) due to its vortex shedding, and more specifically on the characterization of these oscillations as the mounting stiffness and the ratio between the fluid and solid densities vary. This validates the handling of the external force, i.e. the elastic spring, on the body by our algorithm as well as the effect of the density difference between the fluid and the body.

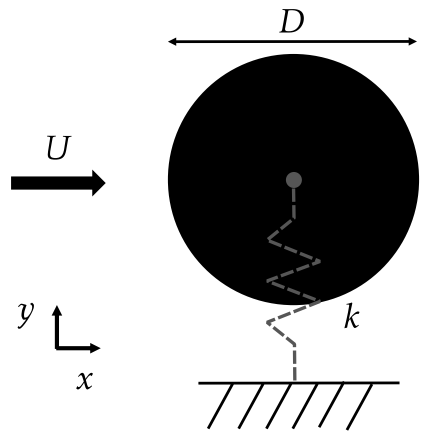

Figure 3.6: Elastically-mounted cylinder in a free stream at Re = 100: configuration parameters.

3.3.1 Configuration

We use the problem setup considered in the work of Shiels et al. [44], also based on a vortex method but with a panel-based boundary condition enforcement. The Reynolds number is fixed at $Re = \frac{UD}{\nu} = 100$, with D the diameter of the cylinder, U the velocity of the induced flow and ν the kinematic viscosity of the fluid. The cylinder is constrained to move only in the transverse direction, along the y-axis.

The MBS framework presented in Section 2.4.2 simplifies into an ordinary differential equation for the cylinder position $y(t)$

$$m\ddot{y} = F(t) = F_y(t) - k\,y(t) \tag{3.2}$$

where the mass coefficient is m and the Coriolis and centrifugal effects vanish because of a single actuated degree of freedom. The total force applied to the system $\mathbf{F}(t)$ contains the hydrodynamic force $F_y(t)$ and the actuation force $-k\mathrm{y}(t)$, derived from a simple Hooke's law with k the spring stiffness.

We verify the extraction of the hydrodynamic force and the coupling of the flow and MBS solvers through the reproduction of a set of results reported in [44]. The shedding cycle is triggered through a brief starting phase in which the cylinder is rotated with an angular velocity $\Omega = \sin(0.125\pi t^*)$ during the dimensionless time ($t^* = \frac{tU}{D}$) interval $[0;4]$, in a way similar to [44]. After this period the cylinder is prevented from rotating and is freed in the y direction to undergo the external forces.

All simulations uses a computational domain size of $[0;21\ D] \times [0;3.5\ D]$ discretized by a 3072×512 grid. We chose a large domain due to the use of a purely unbounded solver for the Poisson equation and to capture the wake evolution over a long time, thus distance. The cylinder rest position is located at $(0.63\,D, 1.75\,D)$. The following numerical parameters for VPM and the penalization are used: LCFL $= 10^{-1}$, $\epsilon = h$, $\lambda = 10^4$.

3.3.2 Results

Fig. 3.7 shows a representative result in terms of kinematics and dynamics. As expected, the adopted motion converges to a periodic oscillation.

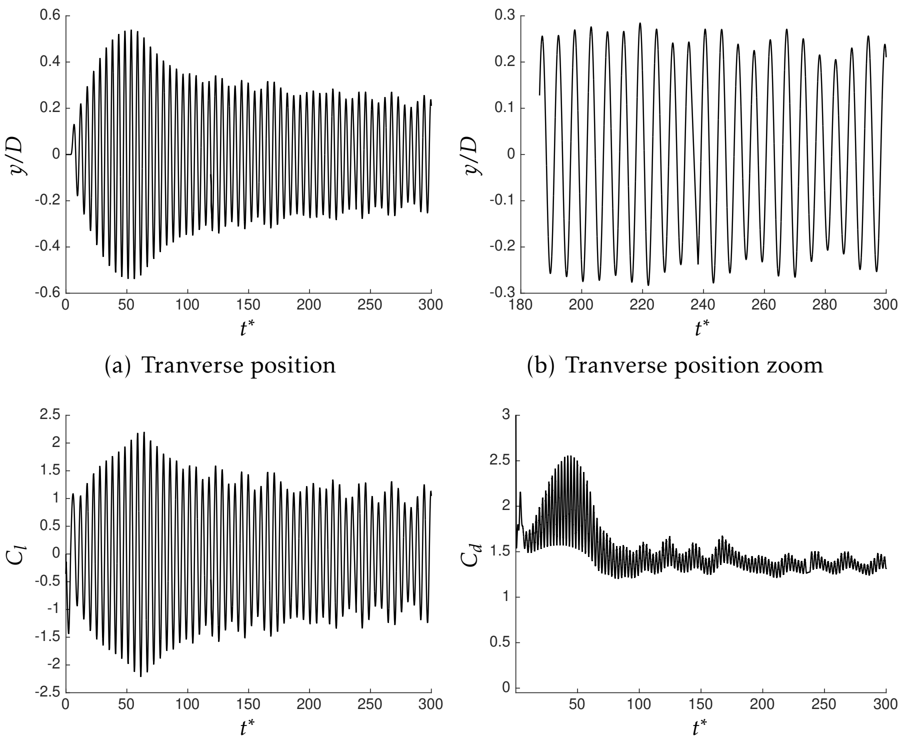

(a) Tranverse position (b) Tranverse position zoom (c) Lift coefficient (d) Drag coefficient

Figure 3.7: Elastically-mounted cylinder in a free stream at $Re = 100$: case $m^* = 7.5$ and $k^* = 14.84$, (a,b) trajectory and (c) lift coefficient and (d) drag coefficient, as a function of dimensionless time.

Figure 3.8 and Table 3.1 gather several cylinder and stiffness configurations and compare them to the reference [44]. Each configuration corresponds to dimensionless numbers $m^* = \frac{\pi\rho_s}{2\rho_f}$ and $k^* = \frac{k}{\frac{1}{2}\rho_f U^2}$

Case	k^*	k^*_{eff}	m^*	f^*	A^*	C_l'	$\overline{C}_d$
Present work	0	-3.79	4	0.155	0.08	0.17	1.32
Reference [44]		-3.94		0.158	0.05	0.20	1.32
Present work	2.48	0.863	1.25	0.181	0.56	0.50	2.08
Reference [44]		0.810		0.184	0.57	0.45	2.16
Present work	14.84	4.46	7.5	0.1872	0.32	1.49	1.38
Reference [44]		4.37		0.188	0.34	1.52	1.42
Present work	29.68	9.80	15	0.183	0.10	0.78	1.37
Reference [44]		12.96		0.168	0.06	0.55	1.35

Table 3.1: Elastically-mounted cylinder in a free stream at $Re = 100$: dimensionless kinematic and dynamic coefficients.

for mass and stiffness, respectively. The resulting cylinder dynamics and kinematics are characterized by the oscillatory part of the lift coefficient $C_l' = \frac{2F_y'}{\rho U^2 D}$, the mean drag coefficient, $\overline{C}_d = \frac{2\overline{F}_x}{\rho U^2 D}$, the dimensionless amplitude $A^* = A/D$ and frequency $f^* = fD/U$; these values are estimated from the last fifteen cycles of the simulation results. Following [44], the effects of inertia and elasticity can be gathered into an effective stiffness $k^*_{\text{eff}} = (k^* - 4\pi^2 f^{*2} m^*)$ under the assumption of a purely sinusoidal motion.

The present results are in a satisfactory agreement with the reference. The kinematics and dynamics, in raw form, mostly follow the reference and the global response, as a function of the effective stiffness, reproduces the same highly non-linear response. Our result for the highest mass ratio exhibits a slight departure from the reference. It can be explained by several factors: (i) the computational domain and the simulation time of Shiels are longer (50 dimensionless times compared to our 21); (ii) our simulation (as seen in Fig. Fig. 3.7) is still settling towards an asymptotic regime: the amplitude A is still decreasing; (iii) the translation of the results to an effective stiffness makes the comparison quite severe as it uses the square of the frequency.

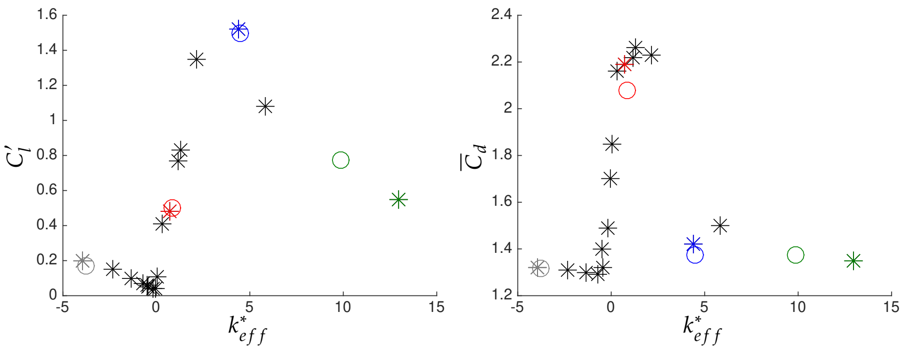

(a) Lift coefficient $C_l' = \frac{2F_y'}{\rho U^2 D}$ (b) Drag coefficient $\overline{C}_d = \frac{2\overline{F}_x}{\rho U^2 D}$

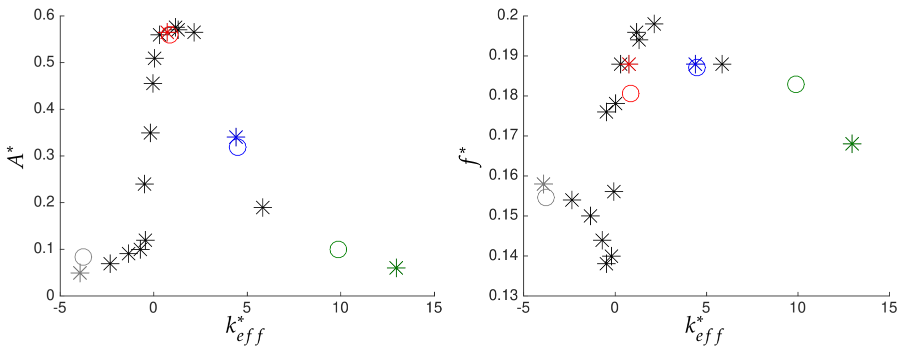

(c) Dimensionless amplitude A^* (d) Dimensionless frequency f^*

Figure 3.8: Elastically-mounted cylinder in a free stream at $Re = 100$: dimensionless kinematic and dynamic coefficients: reference data [44] (star), present results (circles, with matching colors for the same input parameters).

3.3.3 Convergence

We use the case with $m^* = 1.25$ and $k* = 2.48$ to assess the convergence of the method. We compute the solution at $t^* = 0.5$ using a tighter computational domain: $[0; 3\ D] \times [0; 3\ D]$ as the wake has not developed yet. We set the ratio $\epsilon/h = 1$ and maintain the Lagrangian CFL at $LCFL = 0.002$. This $LCFL$ value was chosen such that the time step was essentially constant across all resolutions, thus maintaining a similar and very low time integration error. The penalization parameter is kept at $\lambda = 10^4$. We vary the space resolution from 128×128 to 2048×2048, which we use as our reference solution.

The convergence order was determined by considering the L^2 and L^∞ norms of the error $e(\mathbf{x})$ of the vorticity field with respect to the reference solution

$$e(\mathbf{x}) = \|\omega(\mathbf{x}) - \omega_{\text{reference}}(\mathbf{x})\|. \tag{3.3}$$

Both these errors (shown in Fig. 3.9) exhibit first order convergence; this behavior is consistent with the mollification of the immersed object (using a fixed ϵ/h) in the penalization technique.

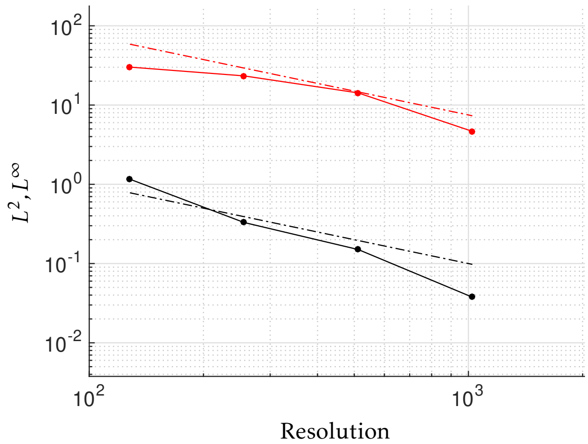

Figure 3.9: Elastically-mounted cylinder in a free stream at $Re = 100$, convergence study: L^∞ (red) and L^2 (black) errors; dashed lines indicate first order.

3.4 Articulated eel-like swimmer

We verify the handling of a chain of several elements with the case of an eel-like self-propelled swimmer. The contributions of Eldredge [32] and Kanso et al. [13] who assembled swimmers from articulated ellipses with prescribed kinematics are taken as references. This setup allows to assess the extraction of hydrodynamic forces within a MBS and the application of joint kinematics to a complex structure.

3.4.1 Configuration

We consider a swimmer composed of three ellipses, see Fig. 3.10, with an aspect ratio of $\frac{a}{b} = 10$. The distance that separates a hinge from the ellipse tips c is taken equal to $0.2a$. We impose the same prescribed kinematic patterns as in the references

$$q_4(t) = -\cos(t - \pi/2) \quad \text{and} \quad q_5(t) = -\cos(t). \tag{3.4}$$

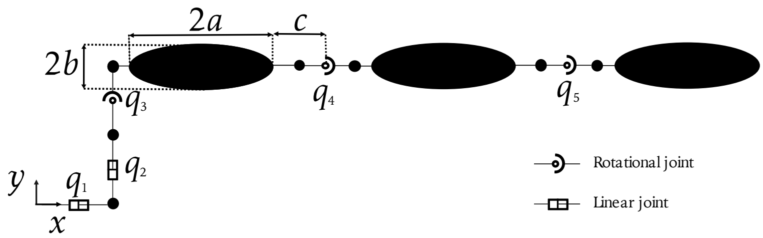

Figure 3.10: Articulated eel-like swimmer: floating base generalized coordinates, q_1, q_2, q_3, and the joints with imposed kinematic, q_4, q_5; $2a$ the length, $2b$ the width and c the distance from the tip to the hinge joint of each element.

The initial velocities are chosen to match the ones of the reference article by taking the same initial values $\dot{q}_{i,\text{init}}$. Our simulations match the *undulation* Reynolds number proposed by Eldredge [32], based on the peak joint angular velocity $\dot{q}_{max}$ and the total length of one ellipse, i.e. $Re = \frac{\dot{q}_{max}(2a)^2}{\nu} = 200$, whereas the results of Kanso et al. [13] provide a theoretical inviscid reference as they are based on the theory for slender bodies. Furthermore, we note that both these references assume massless bodies while the present study considers them as neutrally-buoyant. We still expect the comparison to be relevant as inertial effects are dominated by the added masses of the ellipses along their minor axes ($m_{22} = \rho_f \pi a^2$); the ellipse mass difference ($m = \rho_f \pi ab$ instead of $m = 0$) can then be seen to be a 10% discrepancy.

The characteristic length and velocity scales used for the nondimensionalization are respectively $L = 2a$ and $\mathrm{U} = \dot{q}_{max} L$. The simulation uses a computational domain size of $[0; 2.04\ L] \times [0; 1.53\ L]$ discretized by a 768×576 grid. The swimmer starting position is located at $(0.48\ L, 1.06\ L)$. The following numerical parameters for VPM and the penalization are used: LCFL $= 2.0\,10^{-2}$, $\epsilon = 2h$, $\lambda = 1.0\,10^4$.

3.4.2 Results

The resulting motion over the course of four undulation periods are compared to [32] and [13] in Fig. 3.11. The path of our swimmer was rotated so that its asymptotic direction matches the one of the viscous reference [32]. As a consequence, the steady-state behavior and the initial error can be assessed separately. This correction corresponds to an angle of 5.14°. This mismatch has two potential causes: a more accurate treatment of added mass effects and a body mass exactly zero in the references. The added mass effects are indeed significant and

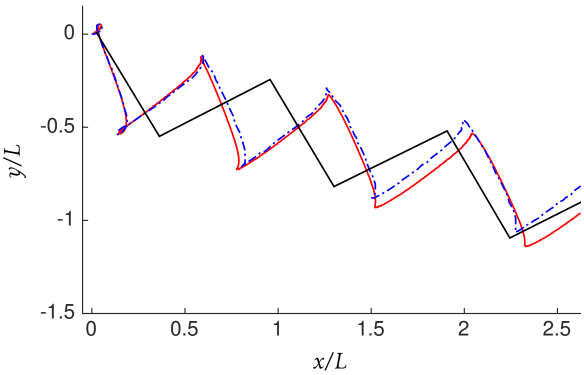

Figure 3.11: Articulated eel-like swimmer: trajectory of the central body centroid: rotated present results (solid red), viscous reference [32] (dashed blue) and inviscid reference [13] (solid black).

govern the initial motion of the swimmer and we recall that the original method, on which our algorithm is based, only exhibited first order temporal convergence for added mass effects [5]. Concerning the density, numerical tests with a smaller density $\rho_s = 0.5\rho_f$ indicate that this angular mismatch in the asymptotic trajectory reduces to 3.6^o, thus hinting at a substantial role of the body density.

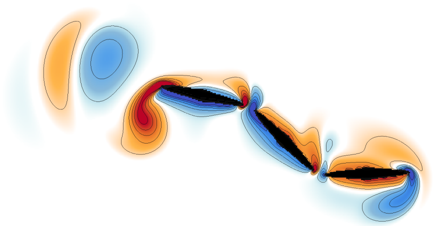

Figure 3.12: Articulated eel-like swimmer: vorticity snapshot around the swimmer at $t^* = 15$. Dimensionless vorticity contours have values from -5 to 5 in 10 uniform increments with negative and positive vorticity in blue and red respectively.

The steady motion appears to be in very good agreement with the viscous reference, both regarding the longitudinal velocity and the lateral oscillations, including their shape and the cusp-like features at the direction changes. The inviscid reference produces a faster swimmer

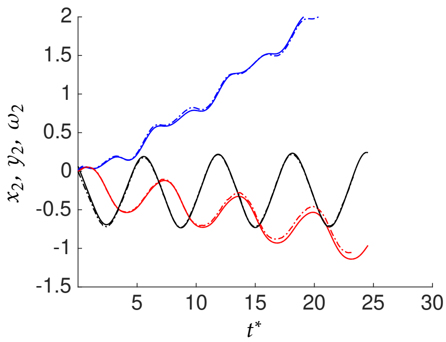

(a) Position

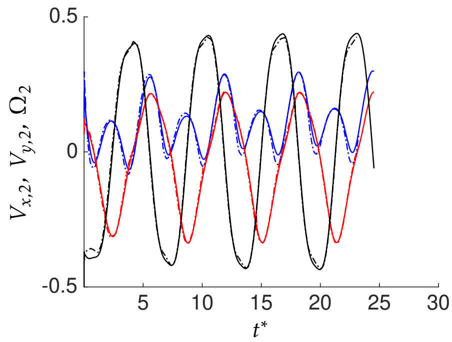

(b) Velocity

Figure 3.13: Articulated eel-like swimmer: velocity components of central body; present results (solid), viscous reference [32] (dashed). Position (velocity) plot depicts x_2 ($V_{x,2}$): in blue, y_2 ($V_{y,2}$): in black and ω_2 (Ω_2): in red.

with very similar lateral oscillations. The reason is twofold: (i) viscous effects play an important role in the longitudinal dynamics of the present results and the viscous reference [32] and (ii) the lateral dynamics are dominated by potential flow effects, which are correctly predicted by the inviscid reference.

Fig. 3.13 offers further insight into the resulting kinematics of the swimmer and confirms the good agreement with the viscous reference in the steady state regime. Forces and moments exerted by the fluid on each constituent body are shown in Fig. 3.14. Force histories confirm the excellent agreement with the reference in spite of the different densities for the swimmers (null in the case of [32]). Again, we recall that the present slender geometries cause the added mass effects to overwhelm the inertia effects and dominate the dynamics. Finally, let us mention that the forces are presented in terms of their raw data for the present work, unlike for the reference where some smoothing is applied [32]; the noise in the forces extracted from the penalization and projection steps thus appear quite moderate.

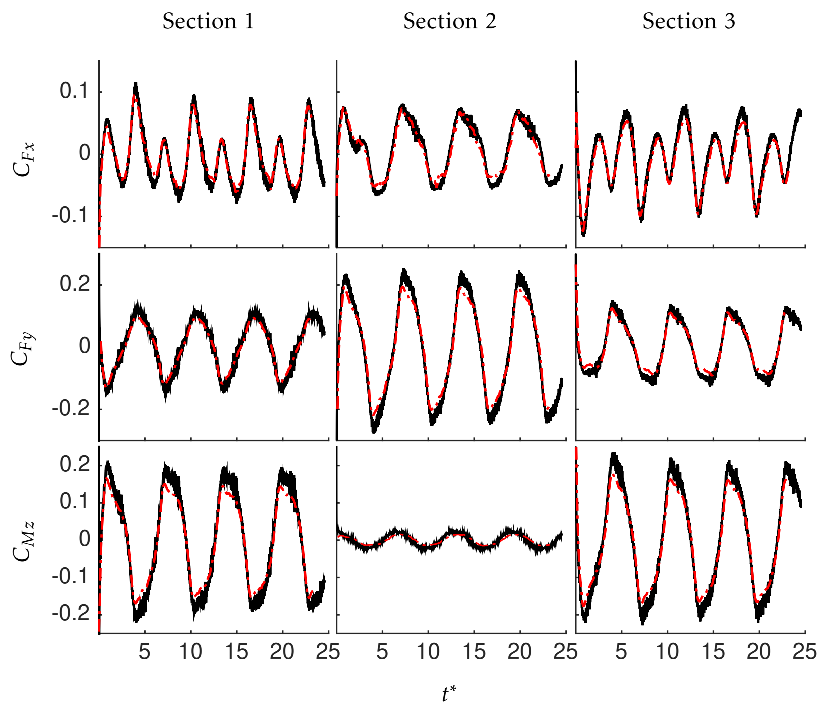

Figure 3.14: Articulated eel-like swimmer: histories of the forces and moments coefficients; present results (solid black), viscous reference [32] (dashed red).

3.5 Passive propulsion in vortex wakes

This fifth test case considers an articulated swimmer similar to the one used in the fourth test case. The swimmer is initially set in a uniform flow past a cylinder as depicted in Fig. 3.15 and its joints are free to rotate, i.e. there is no actuation torque. This setup allows to validate the influence of upstream perturbations on the behavior of a complex system and the application of kinematic constraint between serial body joints.

3.5.1 Configuration

We use the problem setup considered in the work of Eldredge [45]. A cylinder of diameter D and a three segmented swimmer are immersed in a uniform free stream with a velocity U (see Fig. 3.15). The passive swimmer is neutrally buoyant and placed at a distance d downstream of the cylinder. In order to break the symmetry, the fish is placed above the central line at a distance $H = 0.25\ D$. The swimmer is composed of three identical ellipses, $a = 0.3125\ D$, of aspect ratio 5, and the distance from tip to hinge c is set to $0.1D$. The separation distance d is fixed at $3D$. The fish is constrained to stay behind its initial position in the horizontal direction to prevent it from being swept away due to the incident flow. The Reynolds number, based on cylinder diameter and free-stream velocity, is taken as $Re = \frac{UD}{\nu} = 100$.

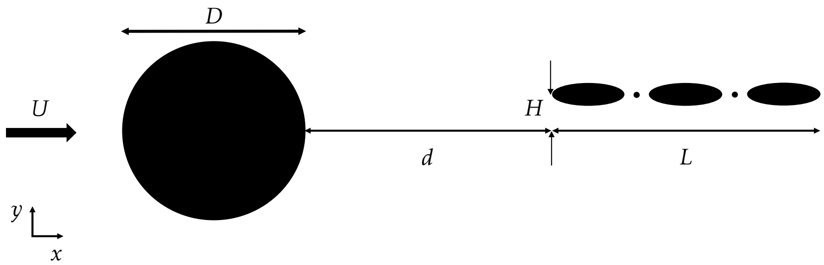

Figure 3.15: Passive propulsion in vortex wakes: configuration setup; cylinder of diameter D and a three-link passive swimmer of length L.

The simulation uses a computational domain size of $[0; 9.9\ D] \times [0; 4.95\ D]$ discretized by a 1536×768 grid. The cylinder rest position is located at $(1.485\ D, 2.475\ D)$. The following numerical parameters for VPM and the penalization are used: LCFL $= 2.0\,10^{-2}$, $\epsilon = 2h$, $\lambda = 1.0\,10^{4}$.

3.5.2 Results

Figure 3.16 depicts the vorticity field and the instantaneous configuration of the system for a fish of length $L = 2.275D$. The joints of the swimmer are free to rotate without frictional or elastic resistance.

After the vortical wake of the cylinder reaches and surrounds it, the fish moves downward towards the central line. At approximately $t^* = tU/D = 15$, the fish begins to move towards the cylinder (Fig. 3.17(a)). The reference and the present result begin to move towards the cylinder at the same time, although our swimmer does not move as far upstream. This quantitative mismatch is due to the fact that this forward movement is affected by a flow instability which break the symmetry of the wake. The onset of this flow instability is very sensitive to the numerical method used; a sensitivity to the spatial and temporal resolutions was also confirmed by numerical experiments. When the fish begins to move towards the cylinder, the symmetry of the wake is broken, and alternating von Kàrmàn vortex shedding begins.

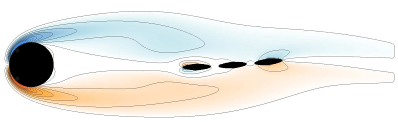

(a) $tU/D = 15$

(b) $tU/D = 24.64$

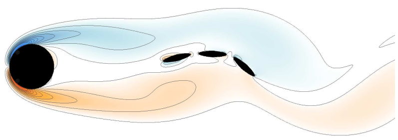

(c) $tU/D = 26.4$

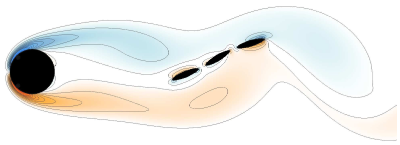

(d) $tU/D = 28.08$

Figure 3.16: Passive propulsion in vortex wakes: snapshots of the configuration and the vorticity around the free swimmer at various $t^* = tU/D$. Dimensionless vorticity contours have values from -5 to 5 in 20 uniform increments with negative and positive vorticity in blue and red respectively.

The induced vortical flow affects the shape of the swimmer and generates an undulation of the articulated body. The histories of the angles of the individual bodies are plotted in Fig. 3.17; they offer a fairer and more meaningful comparison as the swimmer responds to similar flow structures once the vortex shedding has started. The simulations are in a quantitative agreement and one can observe a traveling deformation wave through the phase shift of the consecutive joints.

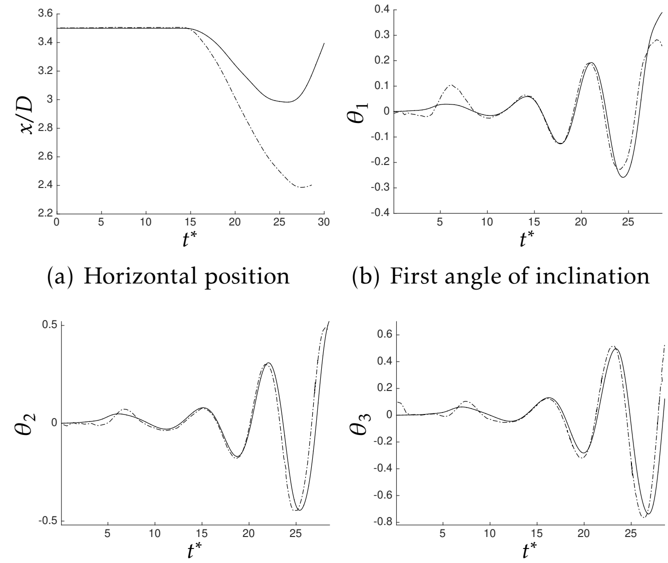

(a) Horizontal position (b) First angle of inclination

(c) Second angle of inclination (d) Third angle of inclination

Figure 3.17: Passive propulsion in vortex wakes: horizontal position of the left-most point of the articulated chain; angle of inclination of each body along the fish with respect to the x axis θ_i; present results (solid), reference [45] (dashed).

3.6 Conclusion

This chapter confirms that the VPM method is able to compute the efforts exchanged between fluid and solid whatever the shape of the solid and its motion. Moreover, these examples demonstrate the effectiveness of the method to reproduce the dynamics of fluid/solid interaction, especially when the latter is subjected to an actuation mostly achieved through the use of springs throughout this chapter.

Chapter 4

An optimization of energy harvesting structure

In this chapter, we investigate an energy harvesting application where a dynamic interdependence scheme is exploit to extract energy. It shows that the present FSI technique can be used to simulate complex interactions between an articulated structure and a vortical flow.

In Section 4.1, we present the configuration of the haverster composed of damping element that carry out the harvesting process. Then, we describe the results and discuss the optimization of those differents dampers. Finally, in the last Section we present the harvester with individually tuned damping coefficient.

4.1 Configuration

This application relies on nearly the same setup as for the validation of Section 3.5 (Fig. 3.15). We consider a three-body swimmer immersed in the wake of a cylinder. The novel structure includes passive mechanical elements. As in the previous test case, the Reynolds number, based on the cylinder diameter D and free-stream velocity U, is taken to be $Re = \frac{UD}{\nu} = 100$. To restrain the degrees of freedom, we reduce the floating base of the swimming structure by removing the first generalized coordinate q_1. The swimmer is fixed at $d = 3D$ in the x direction. The other generalized coordinates are set up in parallel with passive elements such as dampers and spring.

Figure 4.1 shows the new setup and illustrates the parallel springs k_1 and k_2 and the dampers C. The initial vertical eccentricity of the swimmer with respect to the cylinder H and the initial angular position

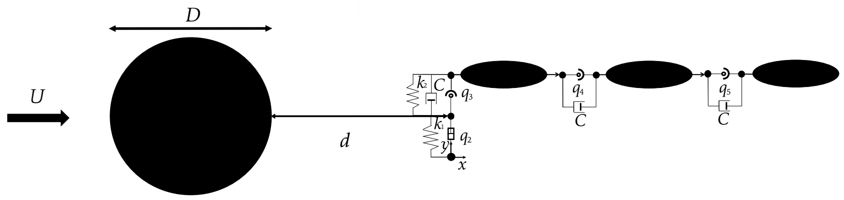

Figure 4.1: Energy harvesting in vortex wakes: multi-body diagram of 3 bodies eel-like structure with damping.

of the joints are set to zero. These damping elements are in charge of carrying out the energy harvesting process. Indeed, damping elements dissipate energy through a reactive torque proportional to the angular velocity of the joint: $\boldsymbol{\tau}_{act} = C\dot{q}_i$, where C is the damping coefficient. The parallel dampers added to each joint are described via a coefficient value C common to the three damping elements. A new dimensionless coefficient captures this damping: $C_g = \frac{2\ C}{\rho U D^3}$. As in the first verification case, the shedding cycle of the induced flow is triggered via a brief starting phase in which the cylinder is rotated (Section 3.3).

Here, we investigate the interaction between the harvester and the vortical structures depending on the damping coefficient. We used several damping values: $C_g =$ 25, 5, 2.5, 0.5, 0.25, 0.05, 0.025, 0.005 and 0. The spring values are described by the following spring coefficients: $k_1^* = \frac{2k_1}{\rho U^2}$ for linear spring and $k_2^* = \frac{2k_2}{\rho U^2 D}$ for angular spring. For the simulations, we choose $k_1^* = 0.8$ and $k_2^* = 0.1$. The spring are chosen in arbitrary fashion, they are not the focus on this specific study and could be also optimise in another research study. The simulation uses a computational domain size of $[0;14.85\ D] \times [0;4.95\ D]$ discretized by a 1536×768 grid. The cylinder rest position is located at $(4.45\ D, 2.475\ D)$. The following numerical parameters for the VPM method and the penalization are used: LCFL $= 2.0\,10^{-2}$, $\epsilon = 2h$, $\lambda = 1.0\,10^4$.

4.2 Results

In order to describe the results, several dimensionless coefficients are introduced:

- the drag coefficients of the cylinder, the harvester and the system as a whole: $C_{D,\text{cyl/har/sys}} = \frac{2F_{D,\text{cyl/har/sys}}}{\rho U^2 D}$ and where $F_{D,\text{cyl/har/sys}}$ is the applied streamwise hydrodynamic force;

- the lift coefficients of the cylinder, the harvester and the system as a whole: $C_{L,\mathrm{cyl/har/sys}} = \frac{2F_{L,\mathrm{cyl/har/sys}}}{\rho U^2 D}$ where $F_{L,\mathrm{cyl/har/sys}}$ is the applied transverse hydrodynamic force; note that the structural force applied on the harvester is recovered from

$$\begin{pmatrix} F_{D,\mathrm{har}} \\ F_{L,\mathrm{har}} \end{pmatrix} = \mathbf{D}(\mathbf{q}) \begin{pmatrix} \ddot{q}_1 \\ \ddot{q}_2 \end{pmatrix} + \mathbf{C}(\mathbf{q}, \dot{\mathbf{q}}) \begin{pmatrix} \dot{q}_1 \\ \dot{q}_2 \end{pmatrix} - \begin{pmatrix} F_{x,hyd} \\ F_{y,hyd} \end{pmatrix};$$

- the mean power coefficient recovered by the damping elements : $\overline{P}^*_{harvest} = \frac{2C\sum_{i=3}^{5} \overline{\dot{q}_i}^2}{\rho U^3 D}$;

- the dimensionless mean power required to tow the cylinder-harvester at a velocity U: $\overline{P}^*_F = \frac{2(\overline{F}_{D,\mathrm{cyl}} + \overline{F}_{D,\mathrm{har}})}{\rho U^2 D} = \frac{2(\overline{F}_{D,\mathrm{sys}})}{\rho U^2 D}$; note that this is identical to $C_{D,\mathrm{sys}}$;

- the harvesting efficiency: $\eta_h = \frac{\overline{P}^*_{harvest}}{\overline{P}^*_F}$.

4.2.1 Harvesting performances

Table 4.1 gathers the values of the mean power recovered by the dampers, the mean power spent to constrain the longitudinal position of the structures – or equivalently to tow the cylinder-harvester in the ambient fluid – and the harvesting efficiency as a function of the damping coefficient. Figure 4.2 highlights the dependency between the mean recovered power and the damping coefficient of the system. We can observe that the maximum power is generated for the C_2 case where $C_g = 2.5$, corresponding to a harvesting efficiency of 29.14%.

Case	C_0	C_1	C_2	C_3	C_4	C_5	C_6	C_7	C_8
C_g	25	5	2.5	0.5	0.25	0.05	0.025	0.005	0
$\overline{P}^*_{harvest}$	0.090	0.430	0.520	0.279	0.279	0.154	0.134	0.012	0
$\overline{P}^*_F$	1.71	1.73	1.78	2.01	1.96	1.98	2.08	2.25	0
η_h	5.26%	24.87%	29.14%	13.90%	14.24%	7.79%	6.43%	0.54%	0

Table 4.1: Energy harvesting in vortex wakes: dimensionless mean power coefficients for several C_g values.

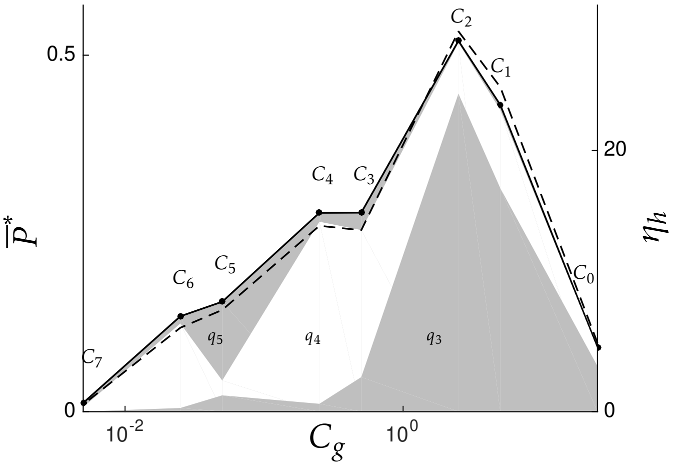

Figure 4.2: Energy harvesting in vortex wakes: mean power coefficient (solid) and efficiency (dashed) versus damping coefficient; the distribution among the joints of the mean harvested power is denoted by the shaded areas.

The distribution of the harvested power among the joints is also highlighted and the resulting values are presented in Table 4.2. The power distribution varies substantially depending on the case tested and the trend is non-trivial: the optimum configuration C_2 relies mostly on the first joint while the softer C_4 configuration exploits the second joint. Finally, if we consider that the cylinder cross-section is the representative scale of our device, we can see that the cylinder-harvester system can extract energy at a rate ($\overline{P}^*_{harvest,max} = 0.52$) that is comparable to Betz' optimum for wind turbines ($\overline{P}^*_{Betz} = 0.59$).

Case	C_0	C_1	C_2	C_3	C_4	C_5	C_6	C_7	C_8
C_g	25	5	2.5	0.5	0.25	0.05	0.025	0.005	0
$\overline{P}^*_{q_3}$	70.68 %	72.85 %	85.75 %	17.33 %	3.91 %	14.78 %	3.77 %	0.61 %	0
$\overline{P}^*_{q_4}$	27.64 %	25.45 %	13.69 %	73.92 %	91.61 %	13.50 %	88.66 %	50.22 %	0
$\overline{P}^*_{q_5}$	1.68 %	1.70 %	0.56 %	8.75 %	4.48 %	71.71 %	7.57 %	49.17 %	0

Table 4.2: Energy harvesting in vortex wakes: distribution of the mean harvested power among the joints for all the C_g values.

4.2.2 Dynamics

The resulting hydrodynamic forces can be studied from two perspectives, considering either (i) the harvester and the cylinder as two separate entities, and thus the effects of the harvester presence on the cylinder forces, or (ii) the cylinder-harvester system as a whole.

Cylinder forces We consider the drag and lift coefficients, and more specifically, the amplitude of their oscillatory parts $C'_{L,\mathrm{cyl}}$ & $C'_{D,\mathrm{cyl}}$ and their means $\overline{C}_{L,cyl}$ & $\overline{C}_{D,\mathrm{cyl}}$ (Table 4.3). Figure 4.4 shows the evolution of these coefficients according to the damping coefficient. The mean drag coefficient only decreases slightly whereas the oscillatory component appears to go through a more substantial reduction over the investigated damping coefficients. For the lift force, its mean remains at small values for all the configurations while its oscillatory part exhibits a notable reduction. This very small mean lift and the periodicity of the oscillatory part (a representative history is provided in Fig. 4.3) indicate that the found asymptotic regimes are symmetric: there is no bias in the kinematics or dynamics in the transverse direction.

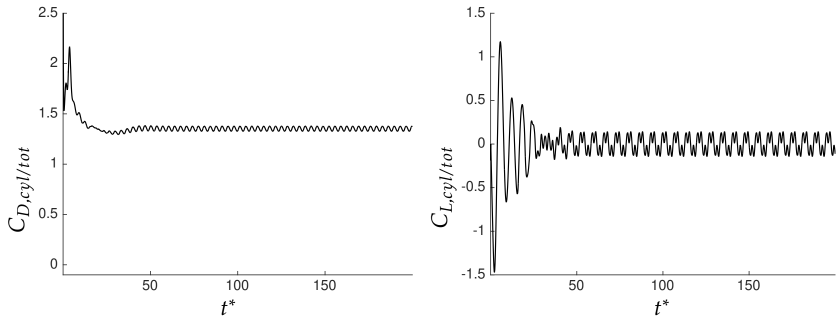

(a) Drag coefficient (b) Lift Coefficient

Figure 4.3: Energy harvesting in vortex wakes: histories of the drag and lift coefficient of the system for the C_2 case.

All these force parameters decrease with the damping coefficient but in a non-monotonic fashion, with a local-minimum for the configuration C_4. If we compare those values to those of an isolated cylinder, the *no harvester* case of Table 4.3, we can observe decreases of up to 7.6% for the mean drag coefficient and of 58% for the oscillatory lift coefficient; however, the oscillatory part of the drag coefficient exhibits an increase up to 51%.

These modified hydrodynamic forces for the cylinder also translate in a modification of the shedding cycle of the cylinder. Figure 4.4(d) shows the Strouhal numbers computed for the cylinder and the harvester, $S_{t,\mathrm{cyl/har}} = \frac{f_{\mathrm{cyl/har}} D}{U}$ where the frequency is extracted either from

Case	No harvester	C_0	C_1	C_2	C_3	C_4	C_5	C_6	C_7	C_8
C_g	/	25	5	2.5	0.5	0.25	0.05	0.025	0.005	0
$\overline{C}_{D,cyl}$	1.45	1.34	1.35	1.35	1.36	1.36	1.37	1.38	1.39	1.39
$C'_{D,cyl} \times 10^2$	2.23	1.99	2.33	2.49	2.70	2.40	3.04	3.31	3.38	3.37
$\overline{C}_{L,cyl} \times 10^2$	-0.54	0.11	0.04	0.09	-0.16	-0.07	-0.10	-0.08	-0.06	-0.05
$C'_{L,cyl}$	0.31	0.13	0.13	0.14	0.15	0.14	0.14	0.16	0.18	0.19

Table 4.3: Energy harvesting in vortex wakes: force coefficients of the cylinder for all the C_g values.

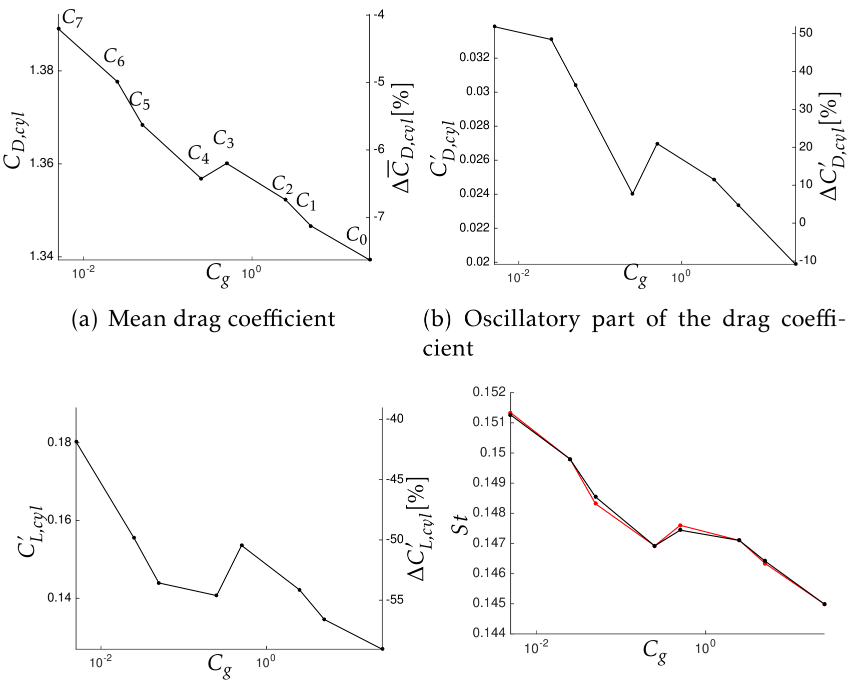

(a) Mean drag coefficient

(b) Oscillatory part of the drag coefficient

(c) Oscillatory part of the lift coefficient

(d) Strouhal number of the cylinder (red) and harvester (black)

Figure 4.4: Energy harvesting in vortex wakes: evolutions of the cylinder force coefficients, also in terms of the relative differences with respect to an isolated cylinder, and of the Strouhal number versus the damping coefficient.

the lift coefficient of the cylinder f_{cyl} or in the motion pattern of the harvester f_{har}. The two bodies get essentially synchronized; we can therefore consider a single Strouhal number, which covers the range $[0.145; 0.151]$. These values are only slightly smaller than the one that was computed for the isolated cylinder $S_t = 0.154$.

System forces Figure 4.5 and Table 4.4 give the evolution of the system force coefficients with damping. The mean total drag coefficient shows a clear decrease over the investigated range of damping coefficients; this drag is larger than for an isolated cylinder for all the cases and specifically, this difference amounts to 27% for the optimal harvesting case (C_2). The oscillatory component appears to go through a more complex evolution. In particular, the oscillatory drag can show a 30-fold increase for the lower damping values. For the lift force, its mean remains at small values for all the configurations while its oscillatory part exhibits a more intricate course. All cases increase the lift oscillations with respect to the isolated cylinder (up to 120%) with the exception of the case C_0 where the oscillatory part is reduced by 26%: the harvester is then quite stiff and tends to act as a fin.

Case	No harvester	C_0	C_1	C_2	C_3	C_4	C_5	C_6	C_7	C_8
C_g	/	25	5	2.5	0.5	0.25	0.05	0.025	0.005	0
$\overline{C}_{D,\mathrm{sys}}$	1.45	1.65	1.75	1.84	1.97	2.00	2.21	2.28	2.28	2.27
$C'_{D,\mathrm{sys}} \times 10^2$	2.23	8.87	6.68	9.26	9.57	11.45	68.02	59.59	35.00	27.78
$\overline{C}_{L,\mathrm{sys}} \times 10^2$	-0.54	0.06	0.73	0.61	-0.80	-0.40	-0.31	-0.20	0.03	-0.04
$C'_{L,\mathrm{sys}}$	0.31	0.23	0.45	0.59	0.68	0.56	0.45	0.52	0.57	0.58

Table 4.4: Energy harvesting in vortex wakes: force coefficients of the system for all the C_g values.

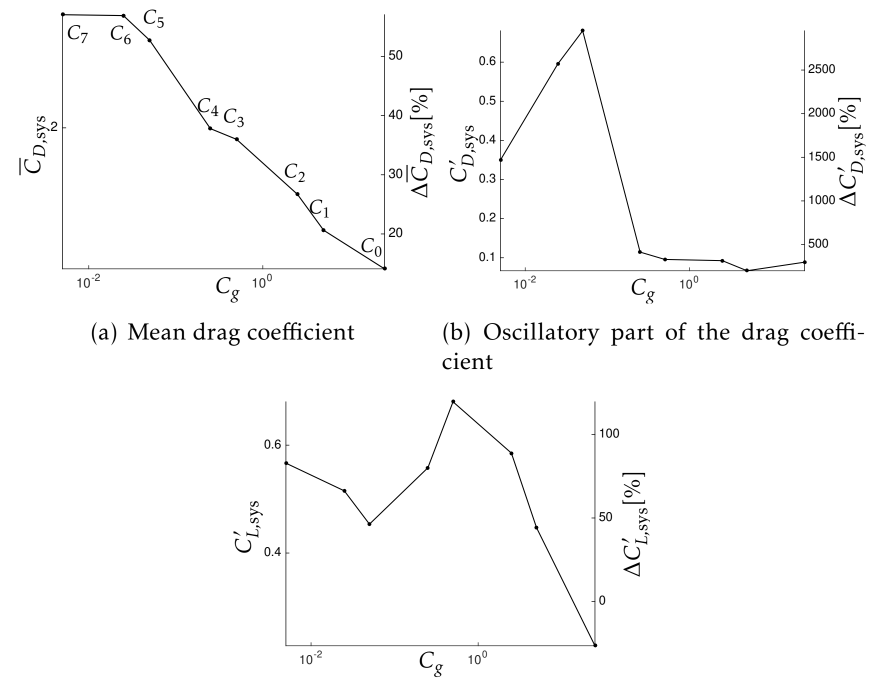

(a) Mean drag coefficient

(b) Oscillatory part of the drag coefficient

(c) Oscillatory part of the lift coefficient

Figure 4.5: Energy harvesting in vortex wakes: evolutions of the system force coefficients, also in terms of the relative differences with respect to an isolated cylinder, versus the damping coefficient.

4.3 Harvester with individually-tuned dampers

We now waive the assumption of a constant damping coefficient for all the joints and, based on the results above, we investigate a configuration that combines the individual optimum values of the damping factors of the joints as identified in Fig. 4.2. Specifically, we pick the cases C_2, C_4 and C_5 as the ones that maximize the power generated for the joints q_3, q_4 and q_5 respectively. The new configuration is then characterized by the damping factors $C_g = 2.5$ for q_3, $C_g = 0.25$ for q_4 and $C_g = 0.05$ for q_5. By doing so, we intend to increase the power recovered by each joint and the total harvesting power.

Figure 4.6(a) shows the resulting damping torque histories at each joint presented as a dimensionless torque coefficient

$$C_{\tau_{Ci}} = \frac{2\tau_{C_i}}{\rho U^2 D^2}. \tag{4.1}$$

The associated instantaneous dimensionless powers are defined as

$$P_i^* = C_{\tau_{Ci}} \frac{\dot{q}_i \, D}{U} = \frac{2\tau_{Ci}\dot{q}_i}{\rho U^3 D}; \qquad (4.2)$$

they are shown in Fig. 4.6(b) and logically exhibit a frequency twice that of the torques. The mean power harvested is $P^*_{harvest} = 0.47$ with

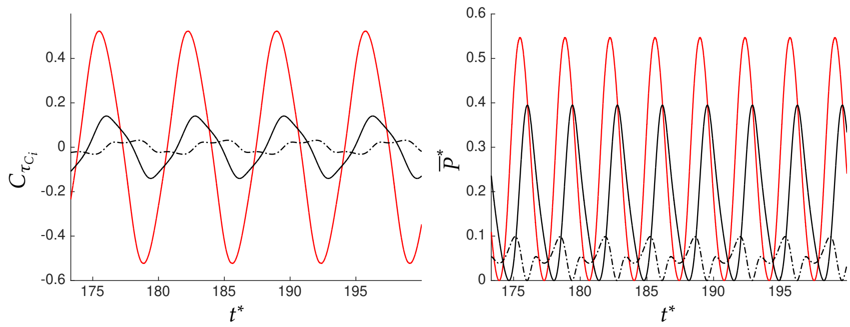

(a) Torque coefficient

(b) Power coefficient

Figure 4.6: Energy harvesting in vortex wakes, individually-tuned damping case: histories of the torque and harvested power for the first joint q_3 (solid black), second joint q_4 (dashed) and third joint q_5 (solid red).

an efficiency of $\eta_h = 22.7\%$. The power distribution among the joints is more uniform: $P^*_{q_3} = 53\%$, $P^*_{q_4} = 37\%$ and $P^*_{q_5} = 11\%$. The histories of the system force coefficients are provided in Fig. 4.3. The cylinder and the harvester are still well synchronized in this configuration and the corresponding Strouhal number is $S_{t,cyl} = 0.1482$. Figure 4.7 depicts the vorticity field and the instantaneous configuration of the system during a period of the motion. The system mean drag, and thus its power coefficient $\overline{P}^*_F$, are increased by 12% when compared to the C_2 case.

This individually-tuned damping therefore does not achieve the power production and the efficiency of the uniform damping case C_2. It still exhibits the interesting property of a more uniform utilization of the harvester devices. Finally, this case hints at the highly non-linear responses to be expected of such systems and it shows that a rigorous optimization procedure will be necessary in order to find and exploit the relevant modes of this configuration.

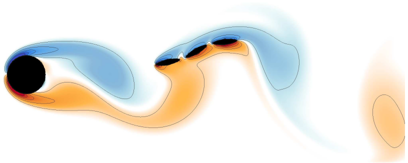

(a) $t^* = t_0^*$

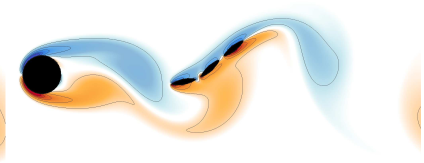

(b) $t^* = t_0^* + T/8$

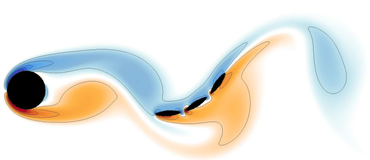

(c) $t^* = t_0^* + T/4$

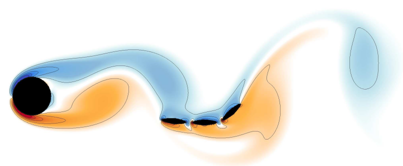

(d) $t^* = t_0^* + 3T/8$

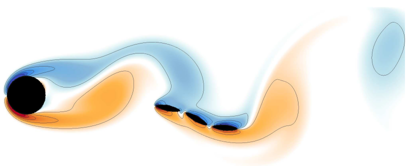

(e) $t^* = t_0^* + T/2$

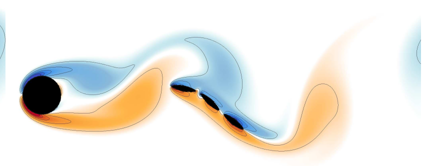

(f) $t^* = t_0^* + 5T/8$

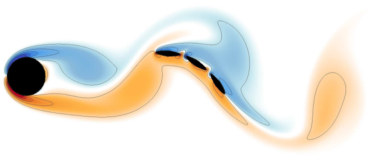

(g) $t^* = t_0^* + 3T/4$

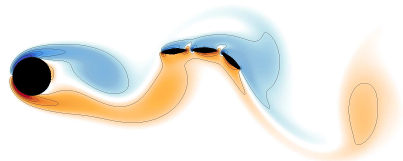

(h) $t^* = t_0^* + 7T/8$

Figure 4.7: Energy harvesting in vortex wakes: harvester configuration and vorticity field over a cycle starting at $t_0^* = t_0U/D = 176$ with individually tuned damping factors $C_g = 2.5$ for q_3, $C_g = 0.25$ for q_4 and $C_g = 0.05$ for q_5Dimensionless vorticity contours have values from -5 to 5 in 10 uniform increments with negative and positive vorticity in blue and red respectively.

Conclusions

In this chapter we have highlighted the great modularity of this method which allows to test a lot of configurations for the study of passive elements interacting with a flow. This energy harvesting case have shown that depending on the setup parameter, we can find damping values that either maximize the efficiency and the recovered power or minimize the drag and lift coefficient on the cylinder.

The last part, Section 4.3, devoted to a rough optimization of the harvester was not presented in the paper [46].

Chapter 5

Swimmer drafting strategies in a perturbed flow

Biological locomotion in fluids studies promises great advances in hydrodynamics, flow control, and efficient underwater vehicles (UVs) propulsion. Nowadays UVs are thrust by means of propellers: those are barred from achieving high efficiency due to the high velocities, hence energy losses, in the jets being produced.

A closer look at fish swimming techniques, for instance anguilliform ones, reveals that undulatory gaits achieve higher efficiency because of effective linear momentum transfer to the flow in the forward direction [62]. Moreover, fish can sense the flow in order to adapt their gait to unsteady conditions and exploit beneficial flow structure. Such behaviors have only recently begun to be uncovered by biologists and engineers alike [1]. An intuitive illustration is represented by the energy saving behavior of fishes resting behind rocks in rivers [63]. On the way to reproduce and understand such intriguing flow-structure interplay, an increasing number of robotic platforms emerged in the last decades [3, 9, 64].

Numerical flow solvers were also applied to self-propelled swimmers in order to investigate swimming gaits and bio-inspired sensorimotor mechanisms. Several methods were proposed, ranging from quasi-analytical theoretical models in potential flow [11,12,13] to more computationally-intensive numerical methods for viscous flows [5,65]. Interestingly, very few can actually be used to study self-propelled structures, their actuation principles, and their dynamical control in a unified framework [8, 9, 47].

In the present chapter, we extend the methodology to the development of a controller that allows a swimmer to draft behind an obstacle. Such a behavior is actually a simplified version of collective motions in actual schools of fish, where the individuals are believed to exploit flow structures generated by their neighbors [66, 67].

In our simulations, the virtual swimmer entails flow sensors, which are used to track the wake of a cylinder in a uniform flow. We investigate the energy saving through this drafting technique by comparing its cost to that of stationary gait in an uniform flow. We also assess the performance of the drafting technique if the wake generator is moving in order to reproduce a leader-follower scenario.

In Section 5.1, we present a bio-inspired control framework. Then, we describe the results and discuss the efficiency of each drafting strategy compare to the free swimming (in Section 5.2.1).

5.1 Drafting benchmark

In this section, we describe a bio-inspired control framework aimed at tracking a wake structure to achieve energy savings. We consider the evolution of a swimmer's configuration in the wake generated by a uniform flow past a cylinder (fixed or moving). Indeed the flow past a cylinder features a wake region, characterized by velocities favorable to the swimmer, increasing its propulsion efficiency. However, the swimmer has to stay close to the cylinder in order to exploit this wake.

We focus on a case where a cylinder of diameter D and a four-element swimmer interact in a uniform free stream of velocity U (see Fig. 5.1). The swimmer is neutrally buoyant and located at a distance d downstream of the cylinder at the beginning of each simulation. The swimmer is composed of four segments, each characterized by $2a = 0.625D$, $b = 0.1a$ and $c = 0.1D$ (Fig. 2.1).

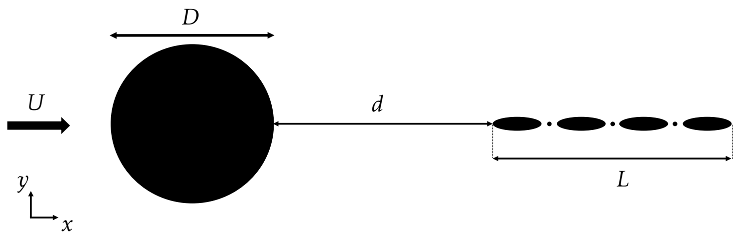

Figure 5.1: Simulation setup: cylinder of diameter D and a four-elements swimmer of total length L. The incoming uniform stream flow has a velocity equal to U.©2018 IEEE

In order to feel the flow, the swimmer is equipped with virtual antennas attached to its head at a distance $d_a = 2a$ of its front segment (Fig. 5.2). The position is chosen to allow the swimmer to feel the external flow and not the boundary layer present near the body surface. The antennas provide an absolute measurement of the flow vorticity V_R and V_L.

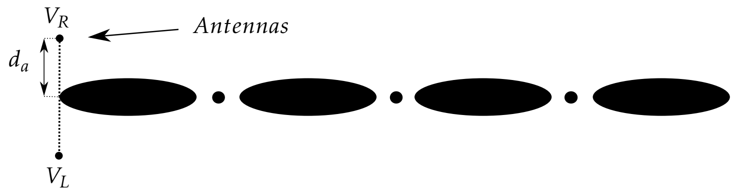

Figure 5.2: Simulation setup: the swimmer is equipped with virtual antennas measuring the vorticity on the right V_R and on the left V_L of its first segment.©2018 IEEE

In the remainder of this section, we develop three nested control laws that are combined in order to stabilize the swimmer in the wake. The three controllers are described as :

- the propulsion controller: it gives a sinusoidal movement to each articulation of the body allowing the actual swimming propulsion;
- the position controller: it manages the distance with regard to the cylinder by modulating the amplitude of movement used for the propulsion;
- the steering controller: it is used to manage the rotation of the swimmer so that it remains align with respect to the wake of the upstream cylinder.

Altogether as shown in Fig. 5.3, the three control loops thus drive the swimmer to maintain a position within the wake of the cylinder and thus should contribute to decrease the energy spent for its locomotion.

5.1.1 Propulsion controller

The fish is propelled by imposing an eel-like movement to its body; the elements generalized coordinates follow the trajectory given by:

$$\begin{aligned} &\text{For } i = 4, \dots, N+2 \ : \\ &q_{i,ref} \ = \ \alpha \, \frac{s_i}{L+0.25} \quad \sin\left(2\pi\left(\omega_f t + \tfrac{s_i}{L+0.25}\right)\right), \end{aligned} \tag{5.1}$$

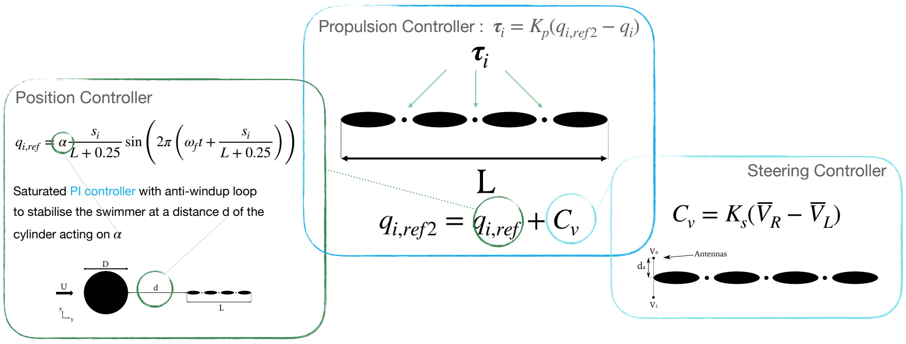

Figure 5.3: Schematic of the three control loops: propulsion, position and steering controllers.

where α is the motion amplitude, L is the length of the fish, s_i is the position of the joint i along the body and ω_f is the global movement angular frequency.

The coordinates kinematics tracking is achieved through a simple proportional controller, i.e.:

$$\begin{aligned} &\text{For } i = 4, \ldots, N+2 \ : \\ &\tau_i = K_{prop}(q_{i,ref2} - q_i). \end{aligned} \tag{5.2}$$

Expressed in dimensionless form, this proportional gain is taken equal to $K'_{prop} = \frac{K_{prop}}{\rho U^2 D} = 100$ in all reported simulations. This value was chosen by trial and error to provide a good kinematic tracking.

5.1.2 Position controller

The distance to the cylinder, d is controlled via the the overall movement amplitude, α, in Eq. (5.1). This parameter makes the swimmer move faster or slower. Closed-loop control is achieved through the use of a saturated PI controller combined with an anti-windup loop, see Fig. 5.4. The coefficients of this controller are the gains K_p and K_i, and the saturation limit S. These gains are adjusted according to the application scenarios that were tested (see Section 5.2).

5.1.3 Steering controller

Finally, a steering controller is in charge of maintaining the swimmer aligned with the cylinder motion relative to the fluid and within the shed vortices, through virtual sensory inputs collected by both antennas. The instantaneously measured values are first filtered through a

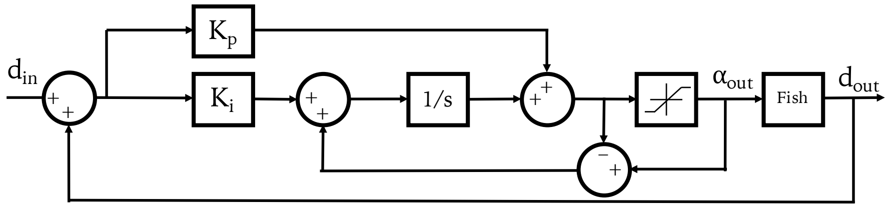

Figure 5.4: Position controller: Proportional/Integral control of the gait amplitude α stabilizing the distance to the cylinder d. An anti-windup loop cancels the integral action when the control input reaches the saturation zone. ©2018 IEEE

second-order exponential smoothing filter with a cutoff frequency f_f. The filtered signals are denoted as $\overline{V}_R$ and $\overline{V}_L$. Steering is achieved by modulating the reference motion of the generalized coordinates by

$$q_{i,ref2} = q_{i,ref} + C_v, \tag{5.3}$$

with C_v being the desired body curvature. This curvature is controlled towards achieving balancing of the absolute vorticities sensed by the the left and right antennas, thus driving the swimmer to an alignment with the vortex shedding

$$C_v = K_s(\overline{V}_R - \overline{V}_L). \tag{5.4}$$

In [43], the swimmer learn by employing a Reinforcement Learning algorithm, how to stay in the wake of a leader. The *Actions* taken by the follower involve manipulating its body curvature. This allows the swimmer to execute turns and to control its speed. This is achieved by introducing a linear superposition to the travelling wave apply on the mid-line curvature. In that approach the swimmer knows its *State* by using its displacement and orientation compared to the follower. Our approach also uses the distance to the upstream obstacle but the big novelty is that we do not use the absolute orientation between the obstacle and the swimmer but the vorticity at the vicinity of the swimmer head in order to give the steering command.

5.1.4 Simulations parameters

Simulations are performed on a domain size of $[0;13.2D]\times[0;6.6D]$ and discretized by a 512×256 grid. The cylinder diameter is taken equal to 0.2 m, its rest position being located at $(1.98D,\ 3.3D)$. The following numerical parameters for VPM and the penalization are used: $LCFL =$

2.10^{-2}, $\epsilon = 2h_{512}$, $\lambda = 1.10^{-4}$ where h_{512} is the spacing of the uniform grid.

The Reynolds number is set equal to $Re = \frac{UD}{\nu} = 100$ and the Strouhal number for the cylinder alone is found to be $St = \frac{f_c D}{U} = 0.23$, with f_c the shedding frequency. We chose the angular frequency of the imposed coordinates trajectory to be high compared to the frequency of shedding, i.e. $\omega_f = 2\pi f = 24\pi f_c$. This higher frequency allows the swimmer to maneuver within the wake vortices and track their motion adequately, as a small fish would surf into the wake of a whale.

All simulations start with an initial phase ($t^* = \frac{tU}{D} \leqslant t^*_{start}$) during which the swimmer is held stationary. This initial phase also contains a perturbation to accelerate the transition to the periodic shedding of vortices by the cylinder. This perturbation, which happens for $t^* \leqslant 4$, consists in a rotation of the cylinder at an angular velocity $\Omega = \sin(0.125\pi t^*)$. The remainder of the initial phase allows the shedding to reach its periodic regime and the shed vortices to interact with the still fixed swimmer.

5.2 Results

In this section, the controllers derived above are validated on three distinct test cases: a swimmer maintaining a stationary position in a uniform flow without a cylinder (1), evolving behind a stationary cylinder (2), and evolving behind a moving cylinder (3). The resulting dynamics are presented in the video attached to this paper.

Table 5.1 gathers the values of the controller coefficients for all the test cases; they are provided in dimensionless form for the sake of generality.

Table 5.1: Dimensionless controller coefficients (for case (1) $K_s'' = K_s' D$)

Cases	$K_i' = \frac{K_i D^2}{U}$	$K_p' = K_p D$	$K_s' = \frac{K_s D}{U}$	S	$f_f' = \frac{f_f D}{U}$
(1)	0.6	6	1.4	2.5	/
(2)	0.6	4	0.2	1.5	0.13
(3)	0.6	4	0.3	2.5	0.05

5.2.1 Position holding in a uniform flow

In this test case, since there was no vorticity upstream of the swimmer, we did not use the steering controller from Eq. (5.4). Instead, a proportional controller canceling the difference of bare vertical position between the swimmer and the reference was used to compute C_v:

$$C_v = K_s''(y_{ref} - y(t))$$

The swimmer goal was thus to remain centered at y_{ref}. Figure 5.5 shows that the swimmer reach a stable position but does not manage to reach the center of the domain. It has a steady-state error but for this specific test it is not of paramount importance because we just wanted to have a swimmer that stabilize horizontally in the flow.

Figure 5.6 reveals that the swimmer reached its reference position at the center of the domain in about 40 dimensionless time units. The average dimensionless power produced by the three joints was equal to $\overline{P}' = \frac{\overline{P}}{\rho U^3 D} = 15.53$ where $P = \sum_{i=4}^{6} \tau_i \dot{q}_i$ is the actuation power. This average was calculated when the swimmer reached its steady position and movement, i.e. when $t^* \geqslant 50$.

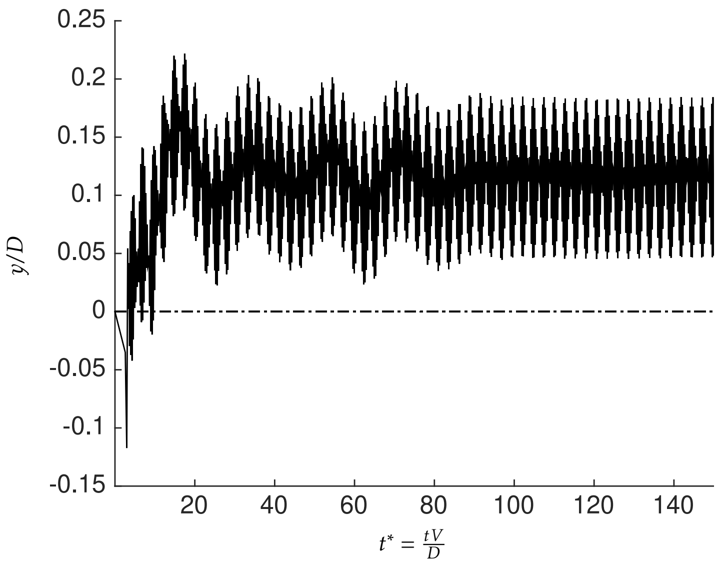

Figure 5.5: Position holding in uniform flow: vertical position of the first segment center of mass (solid) and reference value (dashed). ©2018 IEEE

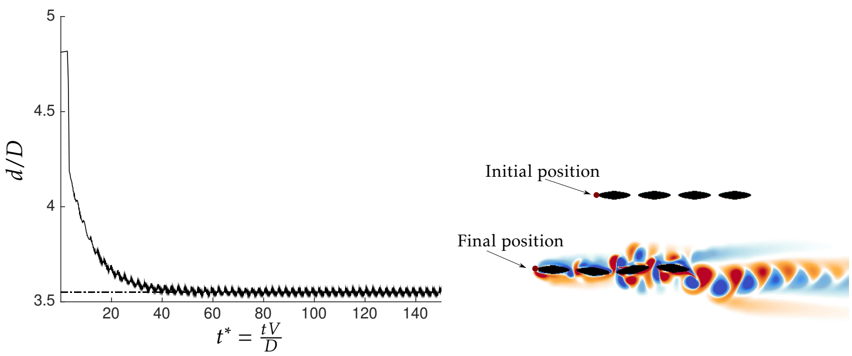

(a) Horizontal position (b) Vorticity snapshot

Figure 5.6: Position holding in uniform flow: horizontal position of the first segment center of mass (solid) and reference value (dashed). Vorticity snapshot at $t^* = tU/D = 40$. ©2018 IEEE

5.2.2 Stationary cylinder wake tracking

Figure 5.7(a) shows the results of the three nested controllers presented in Section 5.1 thus combining the stabilization of distance to the cylinder, and flow exploitation. It reveals that the swimmer reached its stationary position, $d_{ref} = 3.5D$, in the horizontal direction in about 20 dimensionless time and with no overshoot. Regarding the y direction, Fig. 5.7(b) reveals that the swimmer oscillated around the reference position, i.e. the one of the cylinder. The amplitude of these oscillations is about 0.6D. The average dimensionless power produced by the three articulated joints is equal to $\overline{P}' = 13.58$. This average was computed when the swimmer reached its steady position with respect to the cylinder, i.e. when $t^* \geqslant 40$. The average power is thus 12.56% smaller as compared to the first case where the swimmer did not interact with vortical perturbations to maintain its stationary position.

Figure 5.8 shows the vorticity contour around the swimmer when it stabilized in the wake.

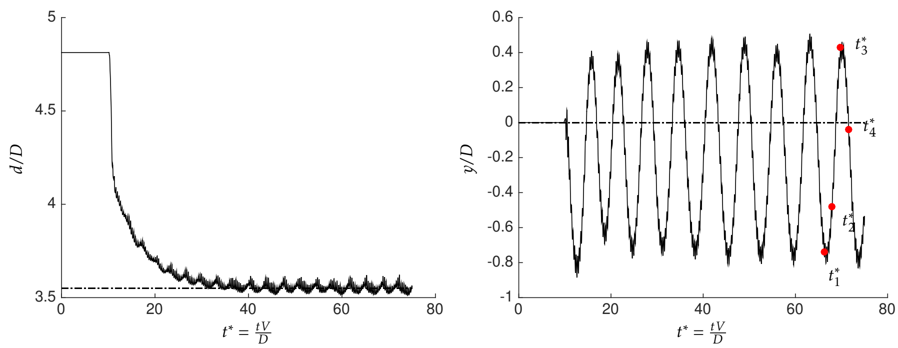

(a) horizontal (b) vertical

Figure 5.7: Stationary cylinder wake tracking: position of the first segment center of mass (solid) and reference value (dashed). The red dots shows the position where each vorticity snapshot have been taken see Fig. 5.8. ©2018 IEEE

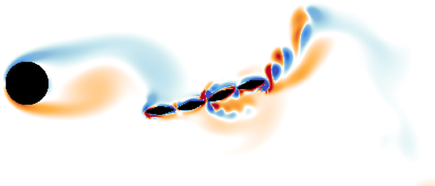

(a) $t_1^* = 66.2$

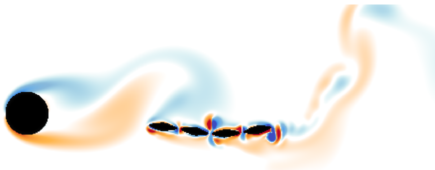

(b) $t_2^* = 68$

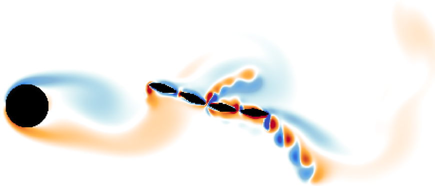

(c) $t_3^* = 70$

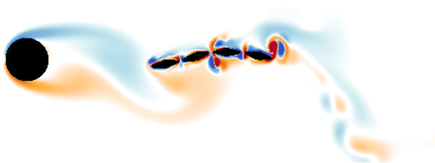

(d) $t_4^* = 71.5$

Figure 5.8: Stationary cylinder wake tracking: vorticity snapshots at different normalized times: $t^* = tU/D$ taken in the last period of the regime movement of the swimmer (Fig.5.7(b)). Negative and positive vorticity are denoted in blue and red respectively. ©2018 IEEE

5.2.3 Moving cylinder wake tracking

Here the kinematics of the cylinder are imposed to follow a vertical motion captured by

$$y_{cyl}(t) = \alpha_{cyl} \sin(2\pi f_{cyl} t)$$

where $\alpha'_{cyl} = \frac{\alpha_{cyl}}{D} = 1.5$ is the dimensionless amplitude and $f'_{cyl} = \frac{f_{cyl}D}{U} = 0.066$ the dimensionless frequency of this motion.

Figure 5.9: Simulation setup: cylinder of diameter D moving in the y direction.

Again the swimmer reaches its reference distance to the cylinder $d_{ref} = 3.5D$, although with larger oscillations as in the previous case, since the cylinder itself is oscillating. The average power in this case is $\overline{P}' = 15.03$. This was calculated when the swimmer reached its steady position with respect to the cylinder, i.e. when $t^* \geqslant 30$. Again the power consumed to stabilize behind the moving cylinder is 3.2% smaller as compared to swimming in a uniform flow.

Fig. 5.12 shows the vorticity plot around the swimmer when stabilized in the wake.

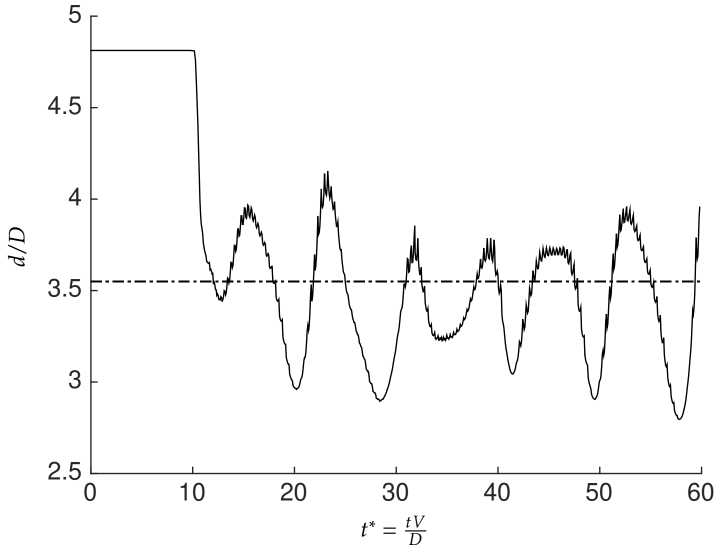

Figure 5.10: Moving cylinder wake tracking: horizontal position of the first segment center of mass (solid) and reference value (dashed).

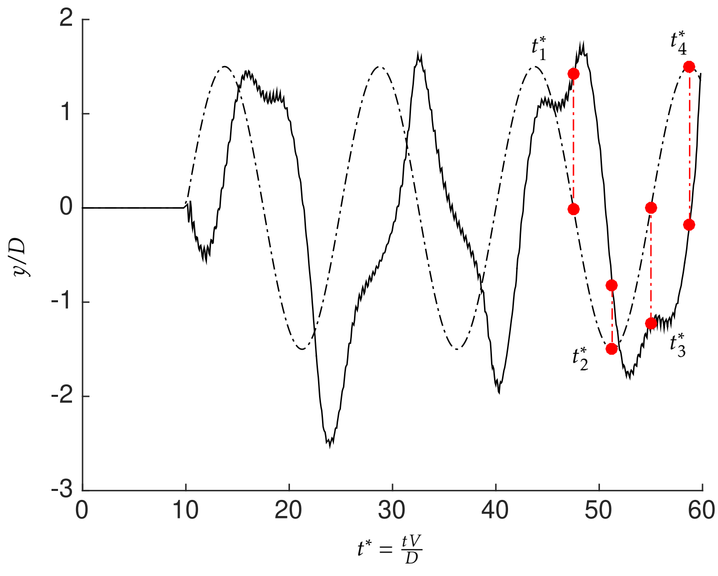

Figure 5.11: Moving cylinder wake tracking: vertical position of the first segment center of mass (solid) and of the cylinder (dashed).The red dots shows the position where each vorticity snapshot have been taken see Fig. 5.12. ©2018 IEEE

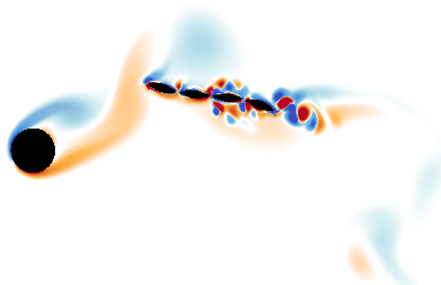

(a) $t_1^* = 47.5$

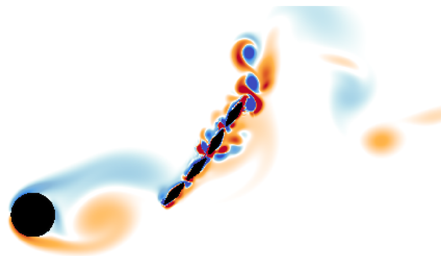

(b) $t_2^* = 51.25$

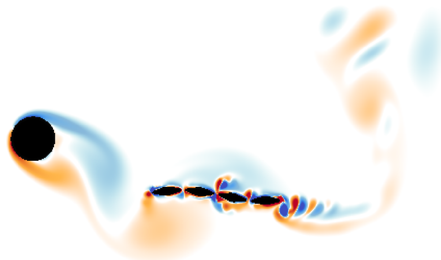

(c) $t_3^* = 55$

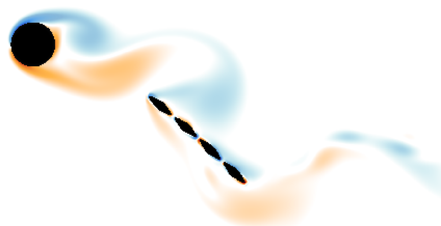

(d) $t_4^* = 58.75$

Figure 5.12: Moving cylinder wake tracking: vorticity snapshots at different normalized times: $t^* = tU/D$ taken in the last period of the regime movement of the swimmer (Fig.5.11). Colors are similar as in Fig. 5.8. ©2018 IEEE

Conclusions

Wakes involve very specific vortical structures (vortices, sheets, tubes) which can subject a downstream device to substantial forces as presented in previous chapter where those forces are used to harverst energy. In the specific case of a cylinder subject to an incoming flow at low Reynolds number, a von Kàrmàn vortex street is generated. This wake structure involves a low pressure region directly behind the cylinder and the shedding of well-separated vortices with alternating strengths. We have shown that it is possible, through a specific motion within the vortex street, to reduce the mean power required to propel the swimming device as it was already promising in Section 3.5 where a passive swimmer achieved a forward movement in the wake of a cylinder. The efficient exploitation of the shed vortical structures requires that the swimmer remains both synchronized with the vortex shedding and close to the cylinder. The last test case illustrates these requirements in a counter-example: the swimmer does not manage to stabilize well enough in the wake and loses most of the drafting benefit. The resulting tracking performance of the control algorithm is thus of paramount importance to stay synchronized with the vortical structures.

This work paves the way towards more complex energy efficient bio-inspired frameworks in complex flow scenarios, which could include many devices interacting through their wakes. Bio-inspired sensing mechanism measuring velocity or pressure along the body length could also be added to the swimmer in order to enhance its perception of the environment. This enhanced sensory apparatus could then be used to follow a specific stream or perturbations created by obstacles. The topic of bio-sensory mechanisms and the subsequent use of the perceived information is still an open problem in biology and engineering: the present simulation environment, which covers flow dynamics, structure dynamics and their control, enables, for the first time, the assessment of sensory and control hypotheses for biological or bio-inspired systems.

Chapter 6

Hydrodynamic effort computation on continuously deformable bodies

Continuous slender bodies are the focus of our attention in this Chapter. By studying continuous deformable bodies, we will be able to study in more detail the fluid/solid dynamics interaction actually at play in biological situations. Indeed, the examples presented in the previous chapters do not allow to reproduce the influence of an actuator between the sub-bodies describing the body. Our goal at the end of the manuscript thesis would be to derive an approach enabling the simulation of continuously actuated bodies. In this Chapter, we focus on the first step toward this goal: the validation of the hydrodynamic efforts formulas, meant for non-deformable sub-bodies, on continuous slender bodies with elastic deformation. The elastic deformation implies a non-solenoidal deformation velocity field: indeed the body deformation does not guarantee a constant volume of deformation. This method validation would be a huge improvement compared to usually used method that recover the effort via the vorticity at the wall, i.e. in a region of high gradients, needing the resolution of a specific Poisson equation for the pressure at the wall. Indeed this method only involve integrals computation on the body that are really simple to implement and computationally less expensive.

First in Sections 6.1 and 6.2, we consider a simple case of fluid/solid interaction with non-solenoidal continuous deformation motion and characterize whether the previously established hydrodynamic forces and moments formulas are still valid. In Section 6.3, those verified formulas are then used to extract the hydrodynamic efforts imposed on a body during its motion and compare them with the literature. Furthermore, we show that the method enables the extraction of the actuation needed for a specific deformation motion. This method could easily retrieve the actuation needed for any prescribed motion.

6.1 Implementation of test case on continuously deforming body

The idea of this test case is to fall back to the algorithm of Gazzola et al. [5] but with a simple difference on the resolution principle. This difference consist in applying the dynamics equation of movement based on the hydrodynamic efforts (see Section 2.4.3) on the swimmer. The swimmer deformation is still prescribed but its resulting motion is the result of the interaction with the fluid. By comparing the results with those of Gazzola, we can then verify if the calculation of forces and moments is valid on a deformable body and not only on rigid bodies.

This verification is the first step to create a fluid/solid interaction solver where the solid is a deformable body (presented in the next chapter). Indeed, if we want to work with deformable bodies we need to check if the way the efforts are computed are still valid.

This swimmer is the same as used in the biolocomotion study from [5] and is defined by a envelop containing the body and a prescribed kinematics of deformation with a non-solenoidal velocity field. The algorithm is modified in order to compute the dynamics equations on the whole body. This entails the computation of hydrodynamic forces and moments on the whole deforming body.

In this section, we detail and discuss the components of this new approach: the body definition and deformation, the divergence step that must be added to correctly capture the flux of momentum on non-solenoidal structure, the handling of the hydrodynamic efforts and the corresponding computational aspects.

6.1.1 The body : geometry and deformation

The geometrical aspect of the two dimensional swimmer is characterized by the half width $w(s)$ of the body along its midline s, $0 \leq s \leq L$ (see Fig. 6.1). Following the work of Kern and Koumoutsakos [10] and Carling et al. [16], the half width $w(s)$ is defined as

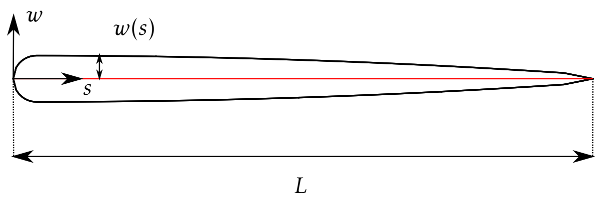

Figure 6.1: Anguilliform swimmer: geometrical definition of the swimmer.

$$w(s) = \begin{cases} \sqrt{2w_h s - s^2} & 0 \le s \le s_b \\ w_h - (w_h - w_t)\left(\frac{s-s_b}{s_t-s_b}\right)^2 & s_b \le s < s_t \\ w_t \frac{L-s}{L-s_t} & s_t \le s \le L \end{cases}$$

where L is the body length, $w_h = s_b = 0.04L$, $s_t = 0.95L$ and $w_t = 0.01L$.

Several analytical descriptions for the motion of anguilliform swimmers have been proposed in the past. In this chapter, we only focus on the lateral displacement of the mid-line, $y_s(s,t)$ (the red line in Fig. 6.1) in the head of the swimmer local frame of reference (w,s), defined as

$$y_s(s,t) = 0.125 \cdot \frac{0.03125 + s/L}{1.03125} \sin\left(2\pi\left(\frac{s}{L} - \frac{t}{T}\right)\right) \tag{6.1}$$

where L is the fish length, s is the arc length of the mid-line, t the time, and T the period.

The previous definition gives access to the position and the deformation velocity of the mid-line in the head frame of reference. In order to obtain a deformation field for the whole swimming body, it is necessary to extend position and velocities away from the mid-line. This is achieved by constructing a deformable mesh as described in Appendix A from [5]. This Cartesian computational grid sticks to the body and describes its deformation through the position and the velocities achieved by each point of the mesh (see Fig. 6.2).

6.1.2 Divergence step

In this study, the velocity deformation u_{def} of the shape is prescribed and varies in time. As this extended velocity field can be non-solenoidal inside the object as it will expand with its deformation, the continuity equation of Eq. (2.2) must be modified into

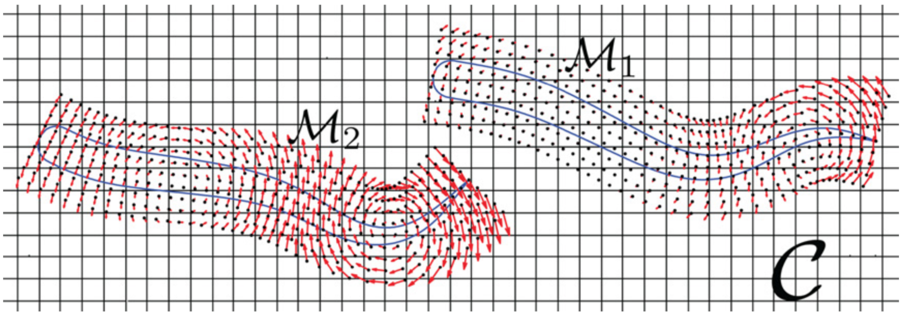

Figure 6.2: Continuous deformable bodies: Schematic of the use of the grids. Here two independents shapes are embedded in their corresponding deformable grids $\mathcal{M}_1$ and $\mathcal{M}_2$, the black dots, that carry the values of deformation velocity u_{def}, the red arrows, and characteristic function $\chi_{\mathcal{M}_1}$, $\chi_{\mathcal{M}_2}$, the blue contour, to be bilinearly interpolated onto the Cartesian computational grid $\mathcal{C}$, the black mesh (figure extracted from [5]).

$$\nabla \cdot \mathbf{u} = 0 \in \Sigma \setminus \Omega \tag{6.2}$$

$$\nabla \cdot \mathbf{u} = \nabla \cdot \mathbf{u}_{def} \in \Omega \tag{6.3}$$

where Σ, the whole domain of computation containing the fluid and body and Ω, the sub-domain containing only the body. Since the deformations u_{def} may not be locally volume-preserving, the recovery of a consistent velocity field across the extended domain requires evaluating the divergence field Eq. (6.4) and adding the corresponding dilatational term in the Helmholtz decomposition Eq. (6.7). Thus this will change the resolution of the velocity field inside the body where those equations must be solved for :

$$\sigma = \chi_s \left(\nabla \cdot \mathbf{u}_{def}\right) \tag{6.4}$$

$$\nabla^2 \psi = -\omega \tag{6.5}$$

$$\nabla^2 \varphi = \sigma \tag{6.6}$$

$$u = \nabla \times \psi + \nabla \varphi \tag{6.7}$$

6.1.3 Fluid-structure interaction efforts

We now derive the hydrodynamic efforts $\boldsymbol{\tau}_{hyd}$ to apply on the whole body. The original method (in Appendix A) solves the FSI problem through the combined use of penalization and projection techniques without explicitly computing the forces exerted on the immersed body.

In this setup, the deformation of the body is prescribed and we do not need to indentify (anglular) moments injected from the actuation component. As a consequence, the penalization contribution is no longer needed as compared to the Algorithm from Chapter 2. We show in Appendix C that the penalization identically oppose to the actuation effects. The only efforts to take into account are thus

$$\mathbf{F}_{\text{hyd,c}} = \frac{d}{dt}\int_{\Omega_{mat}} \rho_f \mathbf{u}\, dV = \mathbf{F}_{\text{proj}}, \tag{6.8}$$

$$\mathbf{M}_{\text{hyd,c}} = \frac{d}{dt}\int_{\Omega_{mat}} \rho_f \left(\mathbf{x}\times\mathbf{u}\right)\, dV = \mathbf{M}_{\text{proj}}. \tag{6.9}$$

6.1.4 Computational implementation

In the following, we describe the implementation of the above methodology into a full algorithm. We recall that the forces and moments $\mathbf{F}_{\text{proj}}$ and $\mathbf{M}_{\text{proj}}$ are computed on the whole body.

The new hybrid method is summarized in Algorithm 2. In red we highlight the lines that changed compared to the original Algorithm of Chapter 2. The superscript n denotes the evaluation time t^n of fields and variables. We then denote the velocity, vorticity, characteristic function, generalized coordinates, forces, moments and density fields at time t^n as $\mathbf{u}^n$, ω^n, χ_s^n, $\mathbf{q}^n$, $\mathbf{F}^n$, M^n and ρ^n, respectively.

Only Eqs. (6.11), (6.12) and (6.13) differ from the original Algorithm 4 in Appendix A. The projection efforts are computed as in the former segmented approach but on the whole body, see Eqs. (6.11) and (6.12).

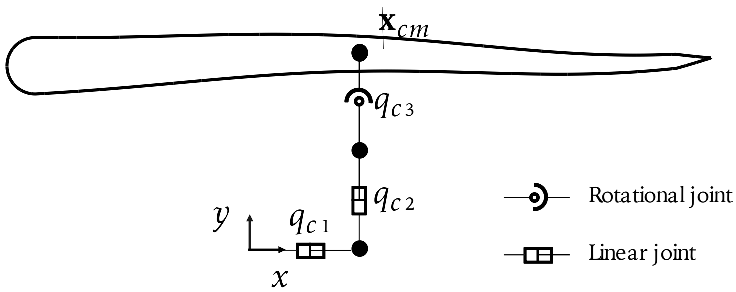

Figure 6.3: Multi-body diagram the new continuous eel-like structure: floating base generalized coordinates, $q_{c,1}$, $q_{c,2}$, $q_{c,3}$ where the reference point on the body is the center of mass.

Algorithm 2 Original method

WHILE $t^n \leq T_{end}$

χ_s^n given deformation

$\mathbf{u}_{DEF}^n$ given deformation velocity field

$\sigma = \chi_s^n(\nabla \cdot \mathbf{u}_{DEF}^n)$

$$\rho^n = \rho_s^n \chi_s^n + \rho_f(1-\chi_s^n) \tag{6.10}$$

$\nabla^2 \psi^n = -\omega^n$

$\nabla^2 \phi^n = \sigma^n$

$\mathbf{u}^n = \nabla \times \psi^n + \nabla \phi^n$

$$\mathbf{p}_{proj}^{*,n+1} = \int_{\Omega_{mat}} \rho_f \chi_s^n \mathbf{u}^{n+1} d\mathbf{x} \qquad \text{with} \qquad \mathbf{F}_{proj}^{n+1} = \frac{\mathbf{p}_{proj}^{*,n+1} - \mathbf{p}_{proj}^{*,n}}{\Delta t^n} \tag{6.11}$$

$$\mathbf{l}_{proj}^{*,n+1} = \int_{\Omega_{mat}} \rho_f \chi_s^n \, (\mathbf{x} \times \mathbf{u}^{n+1}) \, d\mathbf{x} + \mathbf{x}_{cm}^n \times \mathbf{F}_{proj}^{n+1} \qquad \text{with} \qquad \mathbf{M}_{proj}^{n+1} = \frac{\mathbf{l}_{proj}^{*,n+1} - \mathbf{l}_{proj}^{*,n}}{\Delta t^n} \tag{6.12}$$

$$\mathbf{u}_s^n = \mathbf{u}_T^n + \mathbf{u}_R^n = solve(F_{proj}, M_{proj}) \tag{6.13}$$

$$\mathbf{u}_\lambda^n = \frac{\mathbf{u}^n + \lambda \Delta t \chi_s^n (\mathbf{u}_s^n + \mathbf{u}_{DEF}^n)}{1 + \lambda \Delta t^n \chi_s^n} \tag{6.14}$$

$$\omega_\lambda^n = \nabla \times \mathbf{u}_\lambda^n \tag{6.15}$$

$$\frac{\partial \omega_\lambda^n}{\partial t} = -\frac{\nabla \rho^n}{\rho^n} \times \left(\frac{\partial \mathbf{u}_\lambda^n}{\partial t} + (\mathbf{u}_\lambda^n \cdot \nabla) \mathbf{u}_\lambda^n \right) \tag{6.16}$$

$$\frac{\partial \omega_\lambda^n}{\partial t} = \nu \nabla^2 \omega_\lambda^n \tag{6.17}$$

$$\frac{\partial \omega_\lambda^n}{\partial t} + \nabla \cdot (\mathbf{u}_\lambda^n \omega_\lambda^n) = 0 \tag{6.18}$$

$\omega^{n+1} = \omega_\lambda^{n+1}$

$\mathbf{x}_{cm}^{n+1} = \mathbf{x}_{cm}^n + \mathbf{u}_T^n \Delta t^n$

$\theta^{n+1} = \theta^n + \dot{\theta}^n \Delta t^n$

$t^{n+1} = t^n + \Delta t^n$

ENDWHILE

In Eq. (6.13), the solid motion of the deformable structure is solved only based on Newton equations of movement see Fig. 6.3 for notation reference. This is indicated by the function $solve()$ characterized by

$$\ddot{q}_{c,1} = \frac{\mathbf{F}^{n+1}_{x,proj}}{\text{Mass}^n}, \ddot{q}_{c,2} = \frac{\mathbf{F}^{n+1}_{y,proj}}{\text{Mass}^n}, \ddot{q}_{c,3} = \frac{\mathbf{M}^{n+1}_{proj}}{\text{Inertia}^n}. \tag{6.19}$$

where $\ddot{q}_{c,1}$, $\ddot{q}_{c,2}$ and $\ddot{q}_{c,3}$ represent the floating base generalized coordinates acceleration. The Mass and Inertia of the structure are recomputed at each time step based on the new characteristic function χ^n_s.

6.2 Swimming fish : kinematic and dynamics comparison

Based on this new algorithm, a comparison between our methodology and the method of Gazzola et al. [5] is shown for the simulation of 2D self-propelled anguilliform swimmers. The aim of this section is to validate the use of the hydrodynamic efforts on a continuous deforming body with a non-solenoidal deformation velocity field.

The motion pattern used for validation purposes in [5] was first introduced by [16], and consists of a two dimensional deformation of the swimmer mid-line. The lateral displacement of the mid-line, $y_s(s,t)$, in a local frame of reference is defined as in Eq. (6.1).The normals and velocities are approximated with a finite difference scheme.

All simulations are started with the body at rest and the motion is initialized by gradually increasing the displacement magnitude through a sinusoidal function from zero to its designated value during the first cycle. We set the viscosity of the fluid to be $\mu = 1.4\ 10^{-4}$, the body length to be $L = 1$ and the density to be $\rho_{fluid} = \rho_{body} = 1$, resulting in a Reynolds number of approximately 3800, given the final swimming velocity. The volume is conserved, therefore fluid and body densities are the same and the baroclinic term drops out. Simulations are carried out on a rectangular domain $[0,4L]\times[0,4L]$ with a resolution of 1024×1024 grid, $LCFL = 0.01$, $\lambda = 10^4$, and $\epsilon = 2\sqrt{2}h$.

Fig. 6.4 depicts the unsteady forward (u_x, solid line) and lateral (u_y, dashed line) velocities of the center of mass of the body, normalized by L. Similar kinematics are observed. The lateral and angular velocities in the steady regime also match both in amplitude and frequency. We can conclude that the hydrodynamic effort that we consider correctly capture the dynamics of interaction and reproduce correctly the same results.

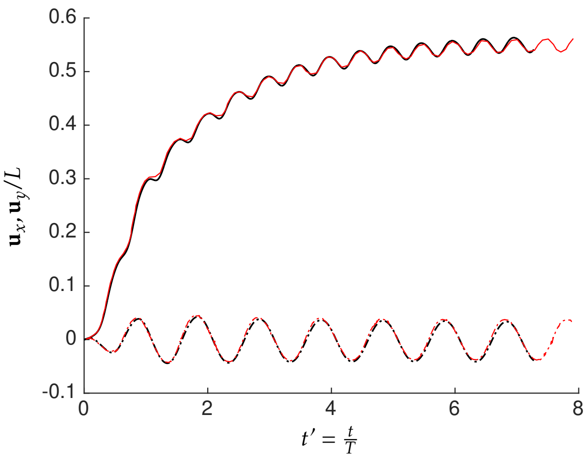

Figure 6.4: Anguilliform swimmer: Forward velocity u_x/L (solid line), lateral velocity u_y/L (dashed line). Black lines indicate 2D swimmer simulations with the proposed method and red lines reproduce the results from Gazzola et al. [5].

6.3 Extraction of fluid and actuation moments

The aim of this section is to compare the hydrodynamic efforts exerted on the continuous deformable swimming structure. The only other method that enables the computation of the hydrodynamic effort is done by Verma et al. [43] where they also use a VPM method combined with the calculation of pressure along the surface of the fish by the complex handling of another resolution of Poisson equation. The present method does only require the integration of the penalization term and projection term on the body domain no complex resolution is needed to recover the efforts on the body.

The second objective of this section is to show that our method is able to recover the hydrodynamic moment exerted on the midline, s, of the structure and ultimately the actuation moment needed to reproduce the same dynamic of motion.

6.3.1 Extraction of the hydrodynamic moments on the midline

In order to compute the hydrodynamic moment exerted on the midline of the swimmer, the body was cut in N sub-bodies which are used to compute the impact of the fluid with respect to the central line.

In Fig. 6.5 we can see the body subdivision. Each subdivision is represented by a characteristic function mollified at the cutting edge with the same mollification factor, $\epsilon = h$, as on the outer surface. Those sub-function are only used to compute the hydrodynamic effort and are not involved in the resolution of the motion dynamics as it is done only on the whole body.

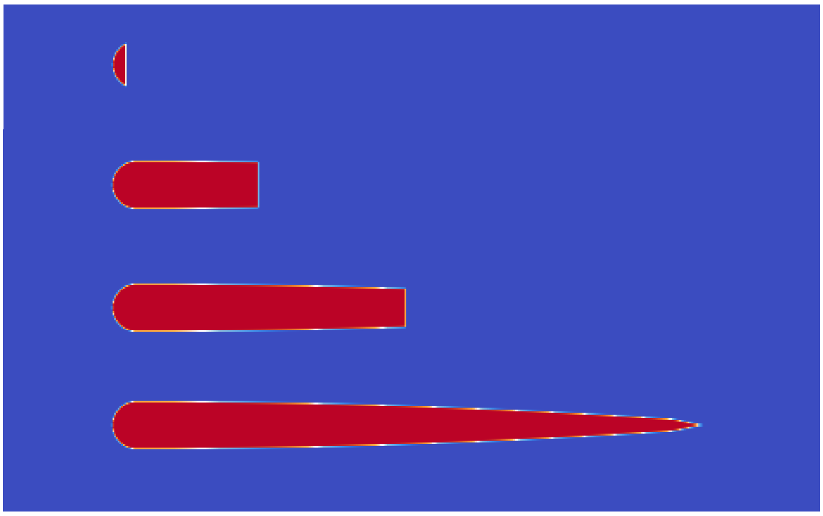

Figure 6.5: Anguilliform swimmer: characteristic function used to compute the resulting moment and forces on the midline. The colormap ranges from blue, ”no body” to red, ”body”, with the transition of color enabling the visualisation of the mollification of the body surface.

We see in Fig. 6.6 how the moments and forces are accounted for on the midline. The integral of the forces calculations are performed on each sub-bodies and the moment is calculated with respect to the red dot. This red dot is located on the midline at the cutting edge.

Concerning the result received from Verma, the forces were given on the outer surface of the body as exposed in Fig. 6.7. For each point of the midline we computed the forces and moments based only on the red colored outer surface in order to have the same hydrodynamic moments than for the present simulations.

$$\mathbf{M} = \sum \mathbf{x} \times \mathbf{F}_S \tag{6.20}$$

where $\mathbf{x}$ is the vector from the surface point of force and the red dot located on the midline.

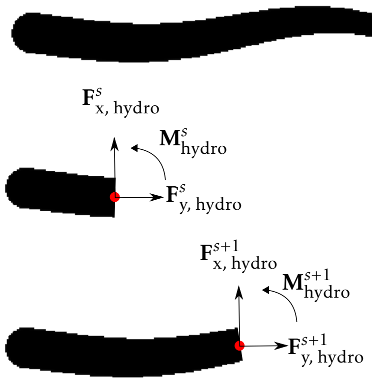

Figure 6.6: Anguilliform swimmer: schematic of the hydrodynamic effort computation on the continuous structure.

6.3.2 Hydrodynamic efforts comparison

Based on this new algorithm, a comparison between our methodology and the method of Verma et al. [43] is shown for the simulation of 2D self-propelled anguilliform swimmers. The motion pattern used for validation purposes in this section is the same as for the previous test (see Section 6.2) but the fluid parameters and dimensions are different: the viscosity of the fluid is set to $\mu = 2.5e^{-6}$, the body length to be $L = 0.1$ and the density is still $\rho_{fluid} = \rho_{body} = 1$, resulting in a Reynolds number of approximately 2600, given the final swimming velocity.

All simulations are started with the body at rest and the motion is initialized as in the last Section. Simulations are carried out on a rectangular domain $[0, 2L]\times[0, 2L]$ with a resolution of 1024×1024 grid, $LCFL = 0.01$, $\lambda = 10^4$, and $\epsilon = h$.

In Figs. 6.8(a) and 6.8(b), we compare total hydrodynamic force applied by the fluid on the structure from the reference curve and the current approach. We can see a slight difference that can be explained by the different methodology. The present methodology is less accurate due to the fact that it does only uses integrals over the body domain.

In Figs. 6.9 to 6.19, the evolution during one period of motion along the midline of the swimmer, s, is pictured. Moments are shown in Figures (a): in black we see the comparison of the hydrodynamic moment

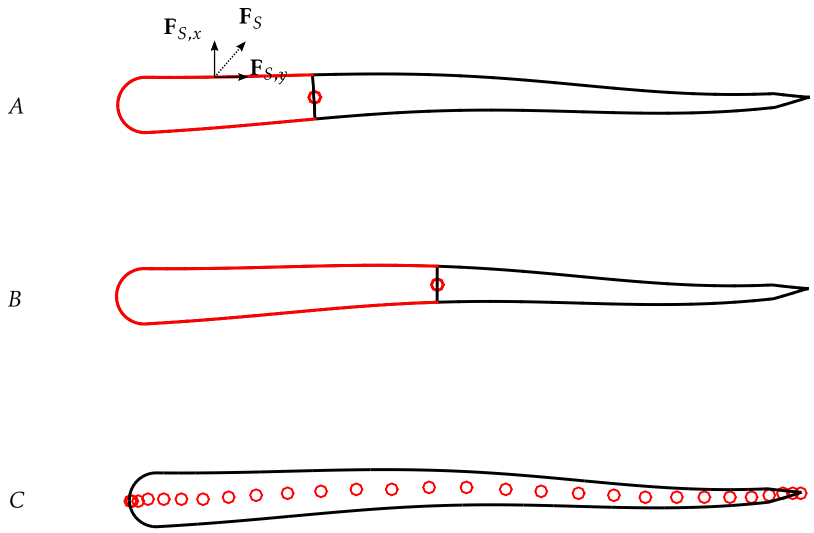

Figure 6.7: Anguilliform swimmer: computation of the hydrodynamic forces and moments on the swimmer form Verma et al. [43]. Subfigures A and B illustrate on two subdivision the outer surface in red where the $\mathbf{F}_S$ are taken into account in order to compute the equivalent force and moment on the red circle center. Subfigure C illustrate the various points taken on the midline used to compute the equivalent forces and moments.

between the reference, dashed line, and the present method, solid line. The result are quite well in agreement. In the same figures, another curve in red show the actuation moment extracted from the movement, the penalization component of force. Figures (b) and (c), show the comparison of force contribution in the forward and lateral direction between the reference, dashed, and the present method, solid. The results are consistent in shape and average value even though we observe a slight difference for the forward component of force. Furthermore, the present method does capture the efforts exchanged at the cutting edge for each sub-function while Verma's method takes into account only the efforts on the surface of the body. Figures (d) shows the vorticity plot around the propelling swimmer.

This method enables to compute the hydrodynamic efforts applied on a deformable body in contact with fluid. The original method of Gazzola et al. [5] did not allow to find these hydrodynamic forces. Through this work, we were able to extend this former work to reach the same result of Verma et al. [43] through a different approach which is less computationally costly but loses a slight precision.

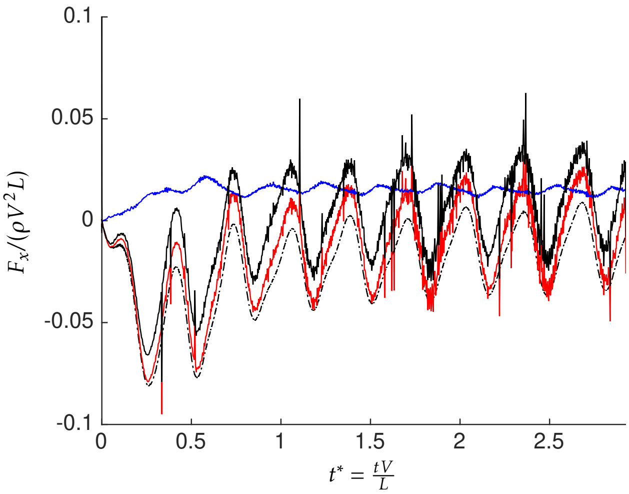

(a) Forward direction

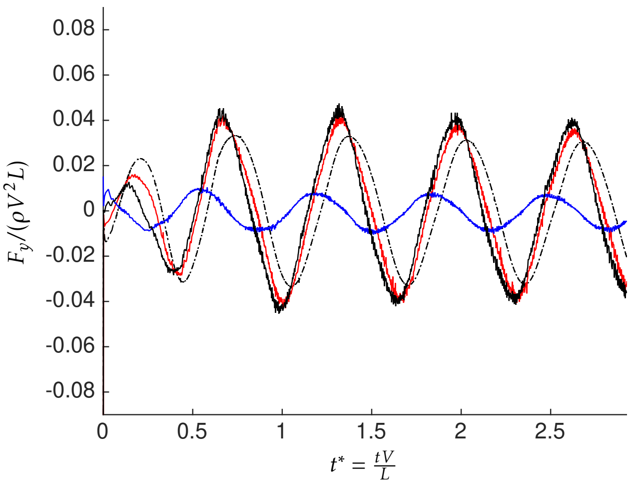

(b) Lateral direction

Figure 6.8: Anguilliform swimmer: hydrodynamic force exerted on the whole body, compared to data from Verma et al. [43]. Verma et al. is reproduced with dashed black lines. The present method is reproduced in solid black lines with the explicit components : projection component, solid blue, and penalization component, solid red.

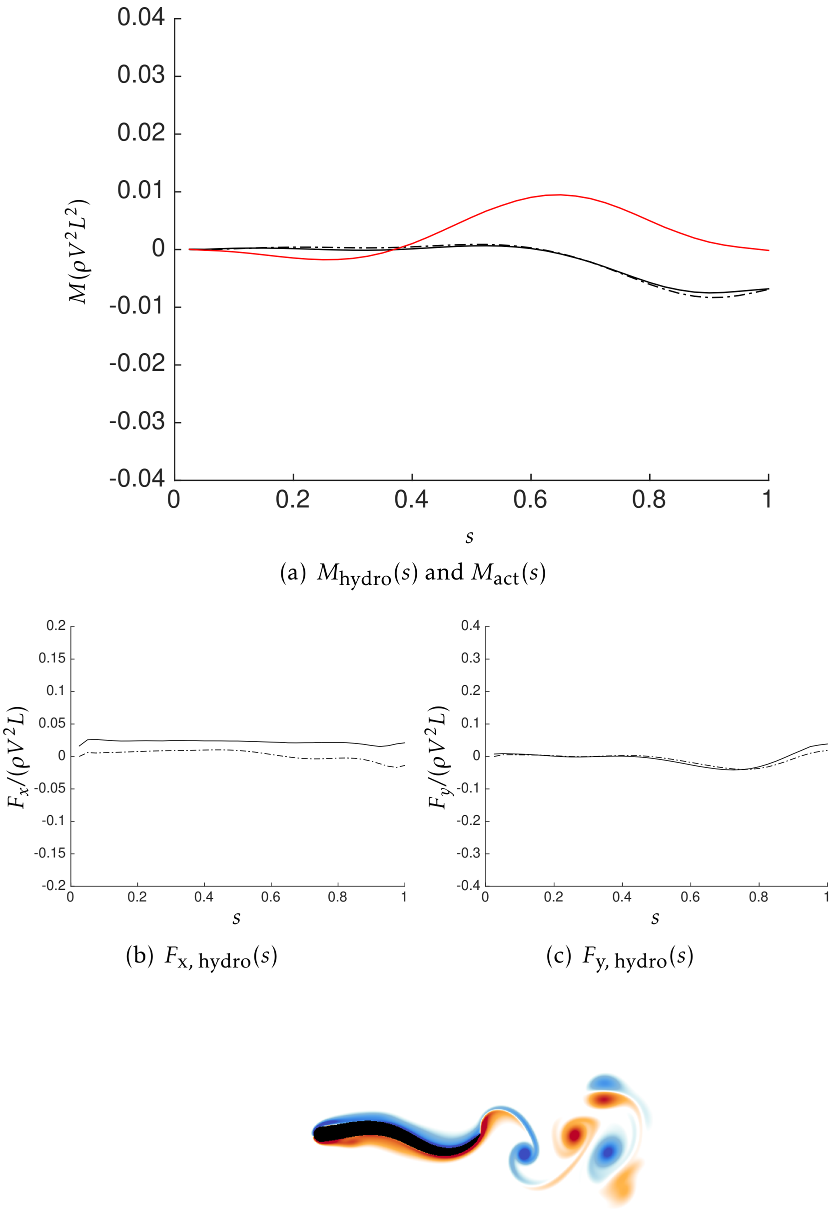

(a) $M_{\text{hydro}}(s)$ and $M_{\text{act}}(s)$

(b) $F_{\text{x, hydro}}(s)$

(c) $F_{\text{y, hydro}}(s)$

(d) Vorticity

Figure 6.9: Anguilliform swimmer: anguiliform swimming $t_1^* = 1.95$: present results, total forces : solid black line and actuation moment solid red line; reference curved from Verma et al. [43] (dashed black line).

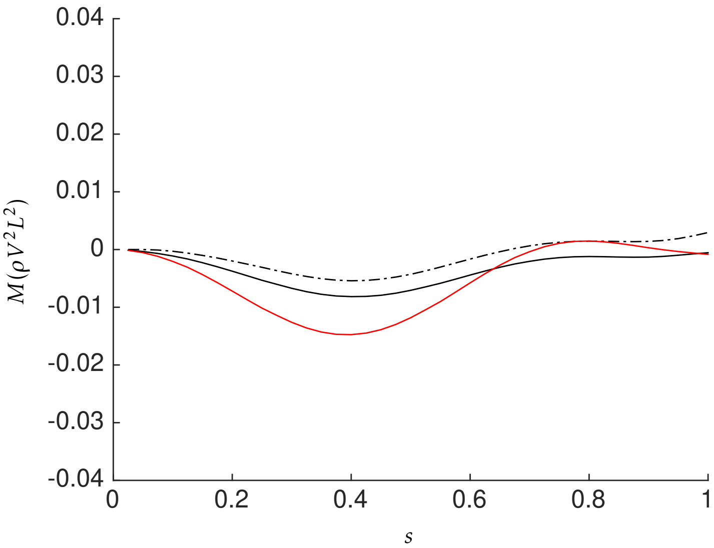

(a) $M_{\text{hydro}}(s)$ and $M_{\text{act}}(s)$

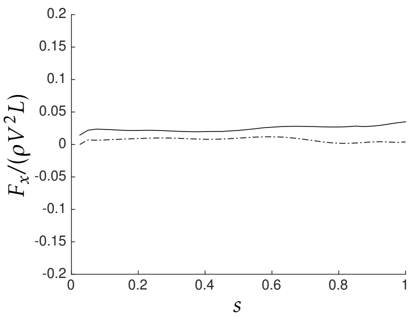

(b) $F_{\text{x, hydro}}(s)$

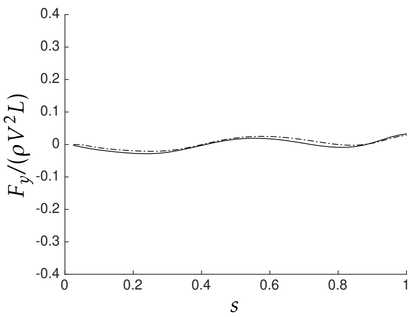

(c) $F_{\text{y, hydro}}(s)$

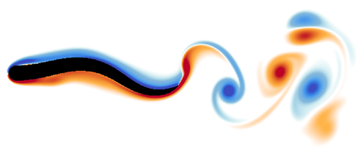

(d) Vorticity

Figure 6.10: Anguilliform swimmer: anguiliform swimming $t_2^* = 2.0$: present results, total forces : solid black line and actuation moment solid red line; reference curved from Verma et al. [43] (dashed black line).

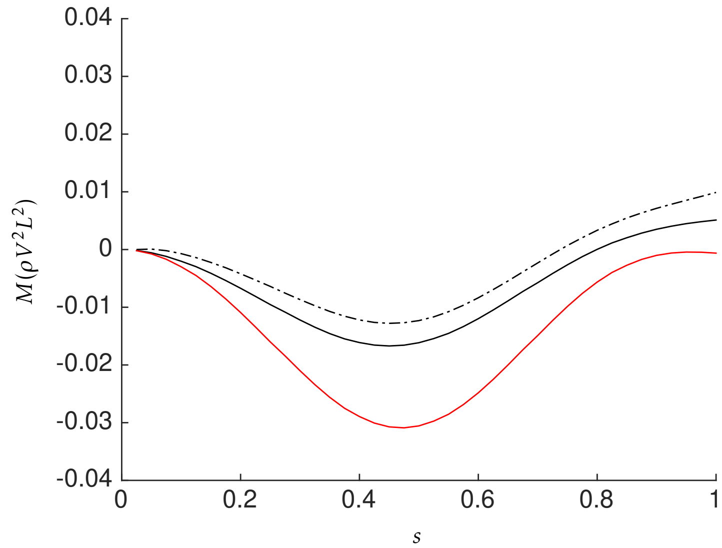

(a) $M_{\text{hydro}}(s)$ and $M_{\text{act}}(s)$

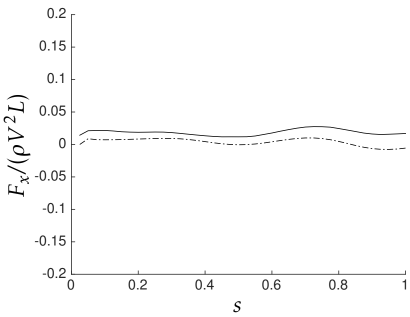

(b) $F_{\text{x, hydro}}(s)$

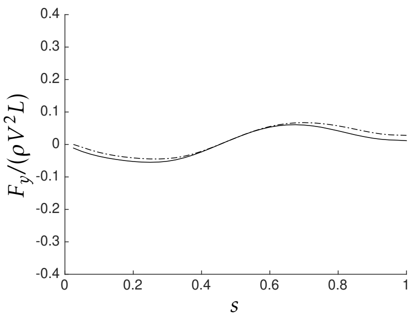

(c) $F_{\text{y, hydro}}(s)$

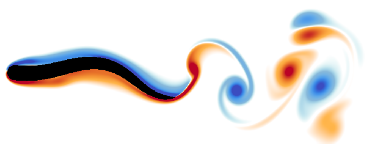

(d) Vorticity

Figure 6.11: Anguilliform swimmer: anguiliform swimming $t_3^* = 2.08$: present results, total forces : solid black line and actuation moment solid red line; reference curved from Verma et al. [43] (dashed black line).

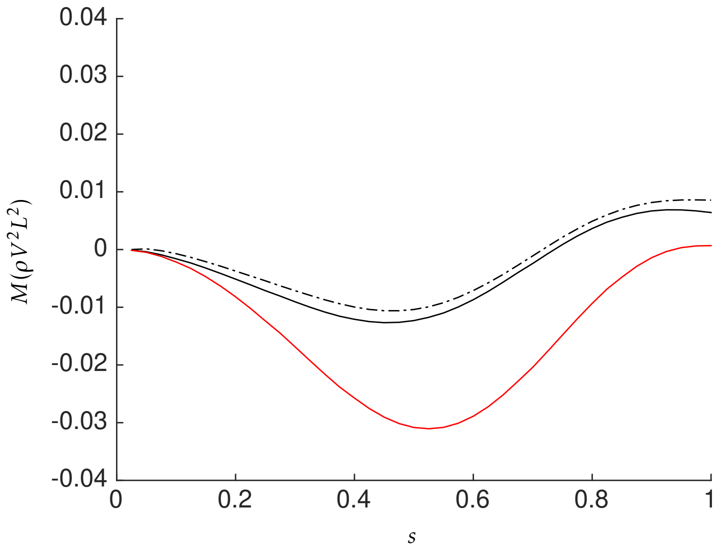

(a) $M_{\text{hydro}}(s)$ and $M_{\text{act}}(s)$

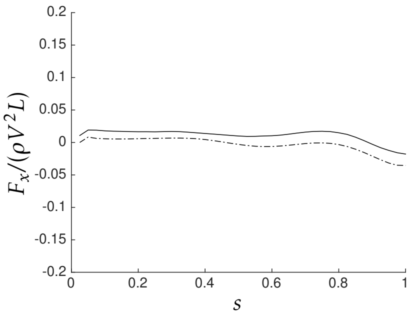

(b) $F_{\text{x, hydro}}(s)$

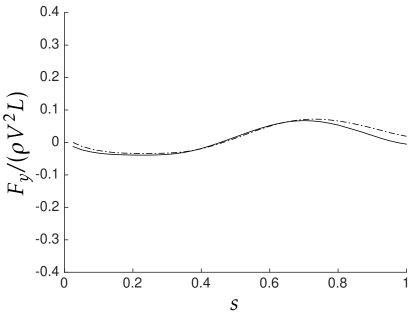

(c) $F_{\text{y, hydro}}(s)$

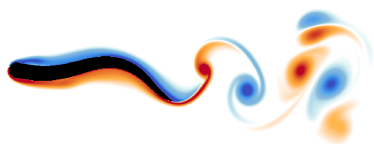

(d) Vorticity

Figure 6.12: Anguilliform swimmer: anguiliform swimming $t_4^* = 2.14$: present results, total forces : solid black line and actuation moment solid red line; reference curved from Verma et al. [43] (dashed black line).

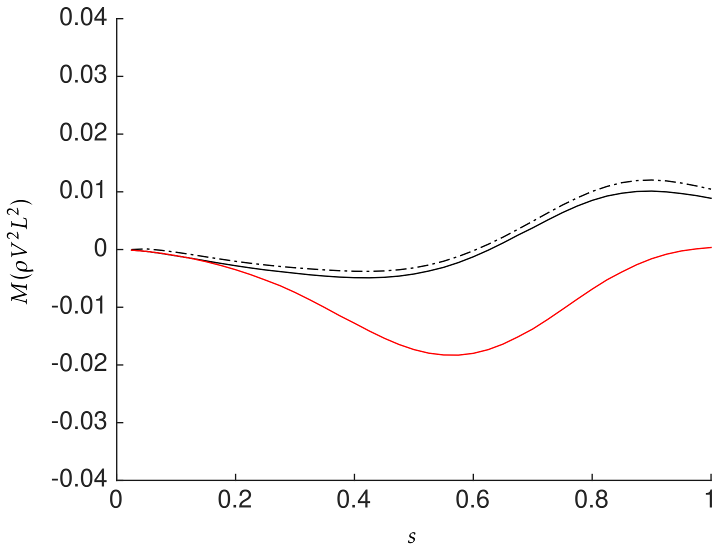

(a) $M_{\text{hydro}}(s)$ and $M_{\text{act}}(s)$

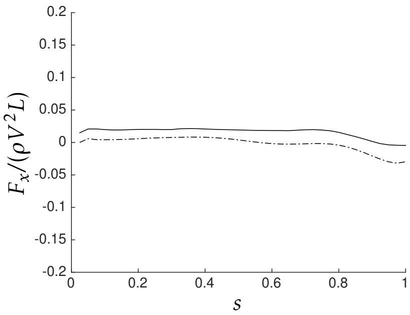

(b) $F_{\text{x, hydro}}(s)$

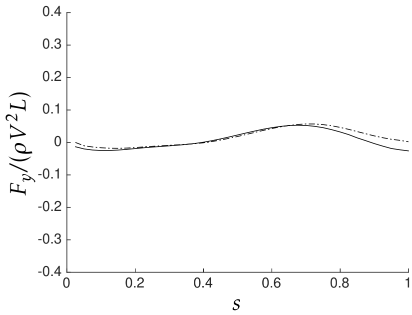

(c) $F_{\text{y, hydro}}(s)$

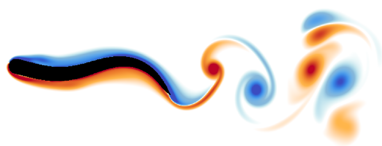

(d) Vorticity

Figure 6.13: Anguilliform swimmer: anguiliform swimming $t_5^* = 2.21$: present results, total forces : solid black line and actuation moment solid red line; reference curved from Verma et al. [43] (dashed black line).

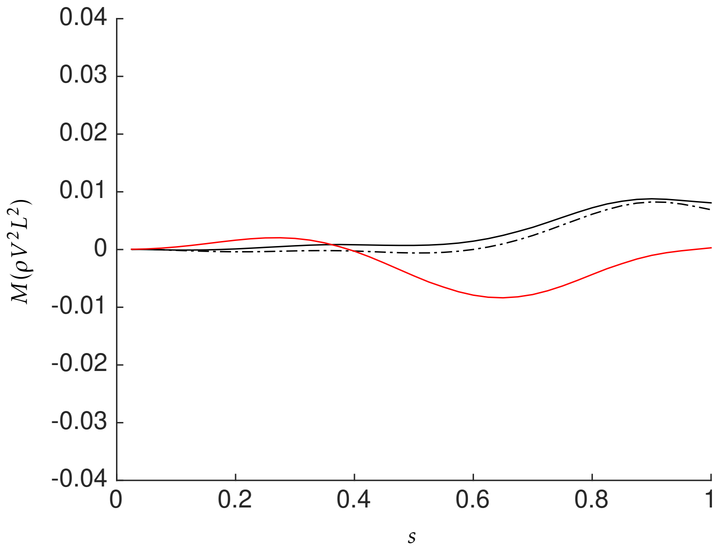

(a) $M_{\text{hydro}}(s)$ and $M_{\text{act}}(s)$

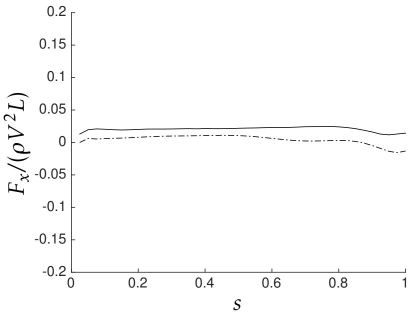

(b) $F_{\text{x, hydro}}(s)$

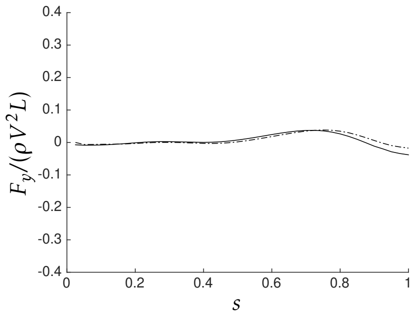

(c) $F_{\text{y, hydro}}(s)$

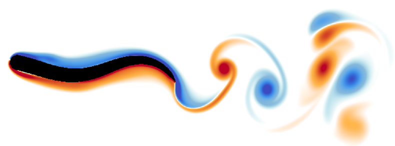

(d) Vorticity

Figure 6.14: Anguilliform swimmer: anguiliform swimming t_6^* =2.27 : present results, total forces : solid black line and actuation moment solid red line; reference curved from Verma et al. [43] (dashed black line).

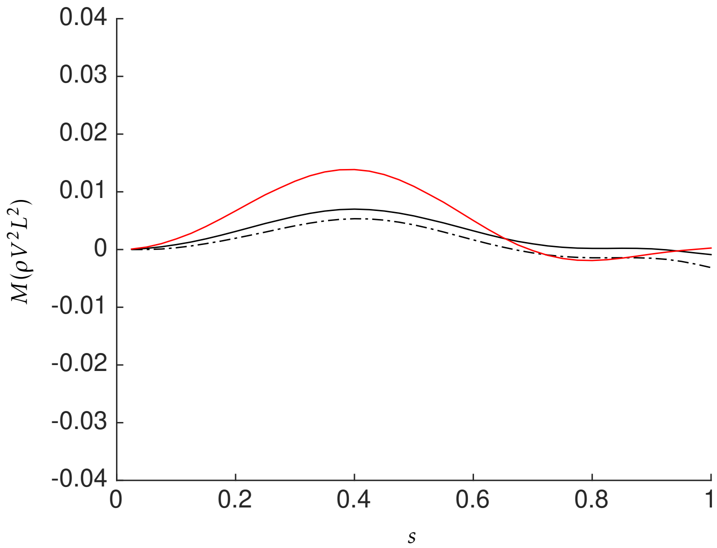

(a) $M_{\text{hydro}}(s)$ and $M_{\text{act}}(s)$

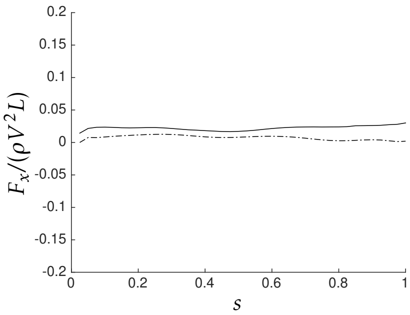

(b) $F_{\text{x, hydro}}(s)$

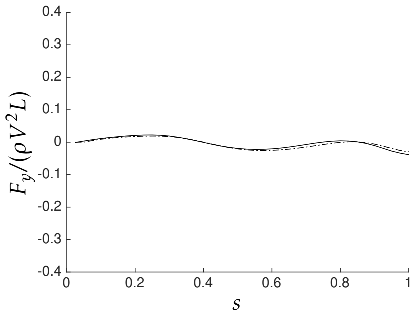

(c) $F_{\text{y, hydro}}(s)$

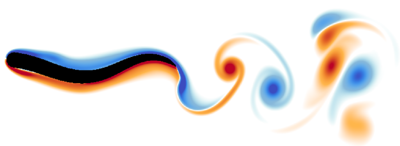

(d) Vorticity

Figure 6.15: Anguilliform swimmer: anguiliform swimming $t_7^* = 2.34$: present results, total forces : solid black line and actuation moment solid red line; reference curved from Verma et al. [43] (dashed black line).

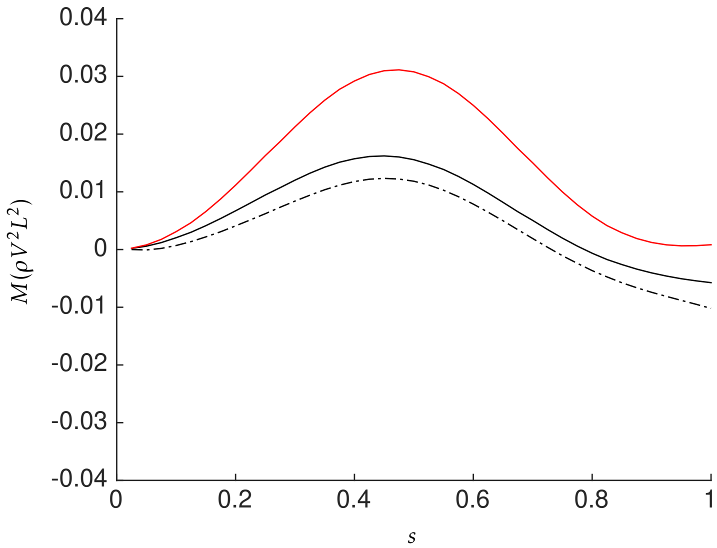

(a) $M_{\text{hydro}}(s)$ and $M_{\text{act}}(s)$

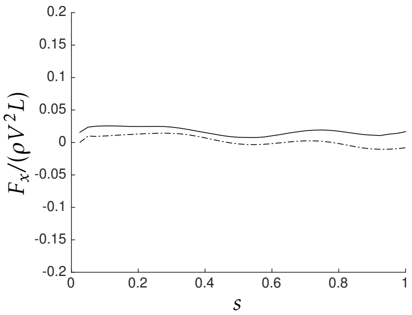

(b) $F_{\text{x, hydro}}(s)$

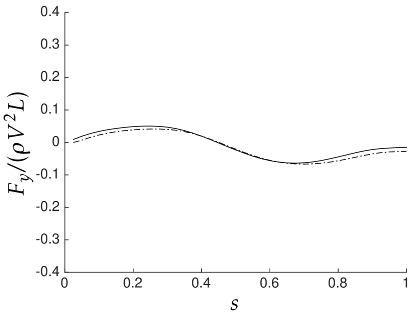

(c) $F_{\text{y, hydro}}(s)$

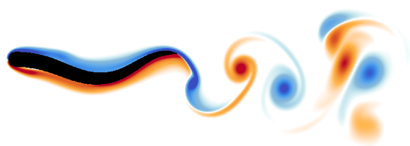

(d) Vorticity

Figure 6.16: Anguilliform swimmer: anguiliform swimming $t_8^* = 2.40$: present results, total forces : solid black line and actuation moment solid red line; reference curved from Verma et al. [43] (dashed black line).

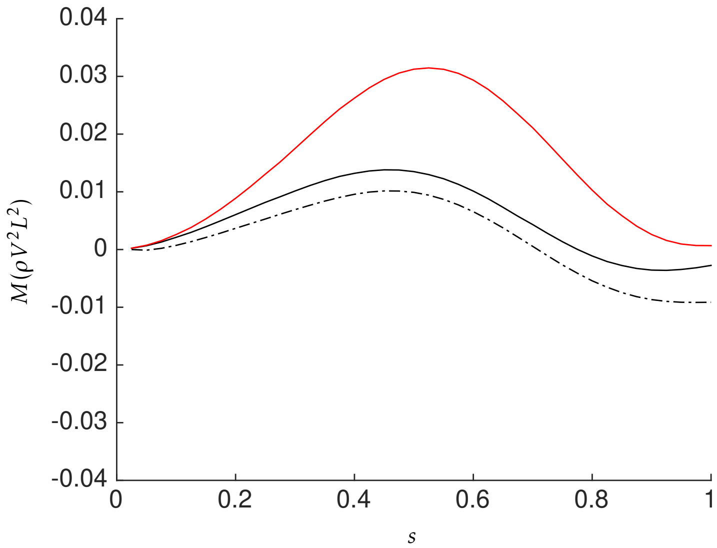

(a) $M_{\text{hydro}}(s)$ and $M_{\text{act}}(s)$

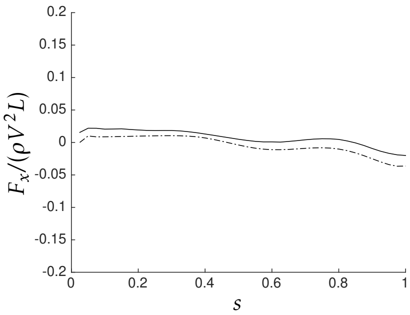

(b) $F_{\text{x, hydro}}(s)$

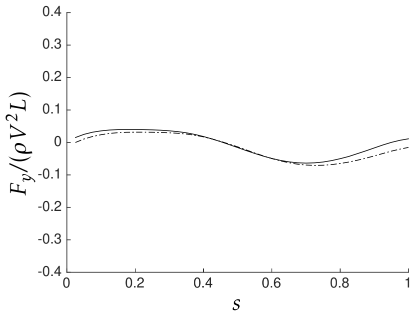

(c) $F_{\text{y, hydro}}(s)$

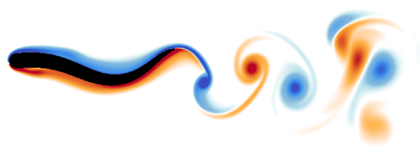

(d) Vorticity

Figure 6.17: Anguilliform swimmer: anguiliform swimming $t_9^* = 2.47$: present results, total forces : solid black line and actuation moment solid red line; reference curved from Verma et al. [43] (dashed black line).

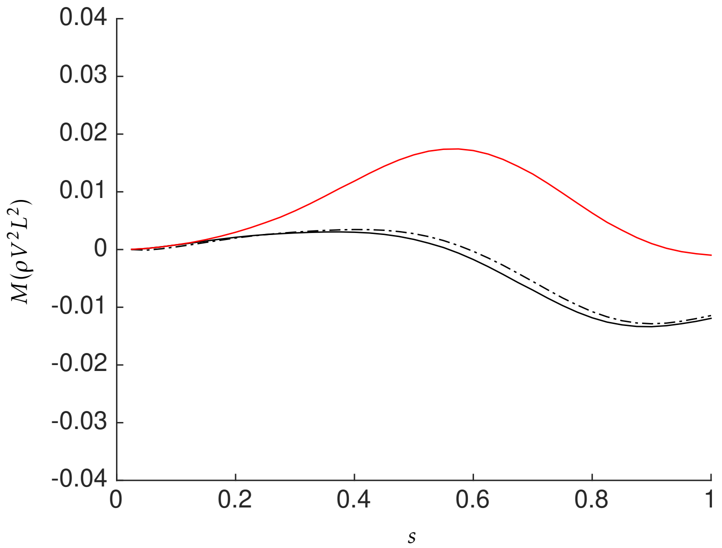

(a) $M_{\text{hydro}}(s)$ and $M_{\text{act}}(s)$

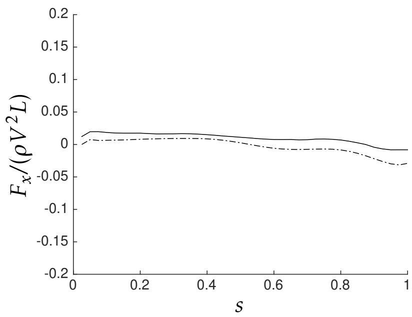

(b) $F_{\text{x, hydro}}(s)$

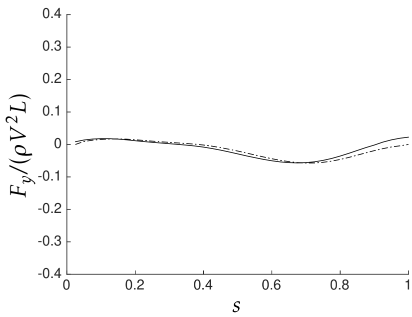

(c) $F_{\text{y, hydro}}(s)$

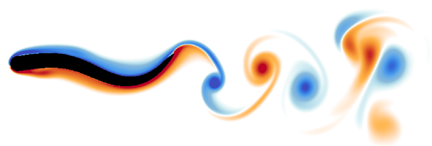

(d) Vorticity

Figure 6.18: Anguilliform swimmer: anguiliform swimming $t_1^*0 = 2.53$: present results, total forces : solid black line and actuation moment solid red line; reference curved from Verma et al. [43] (dashed black line).

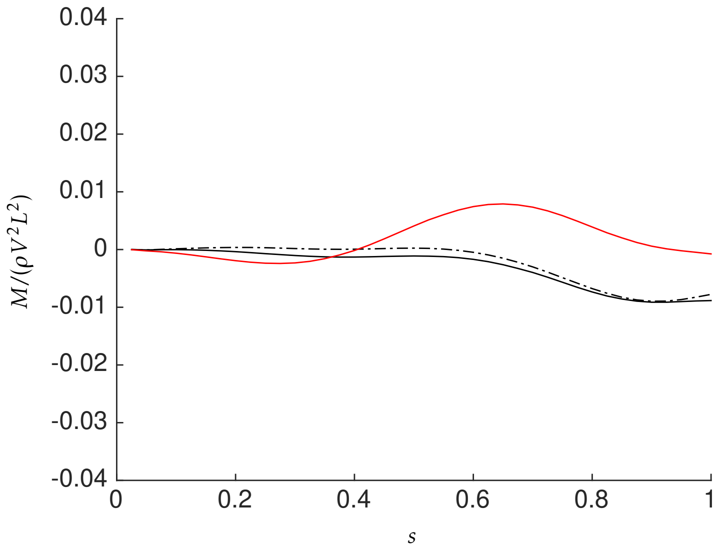

(a) $M_{\text{hydro}}(s)$ and $M_{\text{act}}(s)$

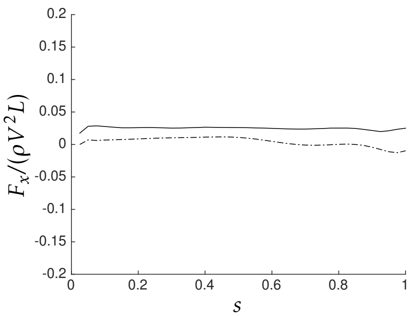

(b) $F_{\text{x, hydro}}(s)$

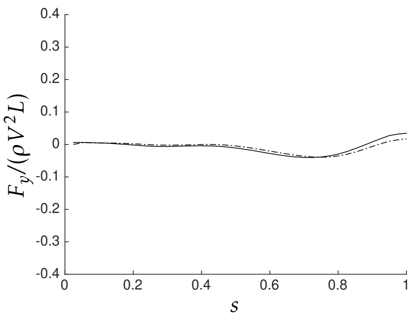

(c) $F_{\text{y, hydro}}(s)$

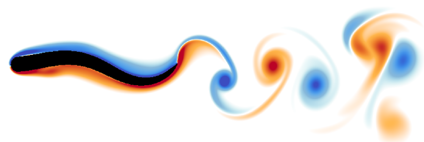

(d) Vorticity

Figure 6.19: Anguilliform swimmer: anguiliform swimming $t_1^* 1 = 2.6$: present results, total forces : solid black line and actuation moment solid red line; reference curved from Verma et al. [43] (dashed black line).

6.3.3 Recovery of the actuation moment on the midline

By observing more deeply the actuation moment obtained in this test shown in Figs. 6.9(a) to 6.19(a), we were able to establish an analytical approximation of this curve. This approximation is done by a parameter fit of the following function mainly depending on the position along the midline, s, and the frequency of motion, f (from Eq. (6.1)) :

$$
\begin{aligned}
M_{\mathrm{act}}(s,t)/(\rho V^2 L^2) &= A(s)\sin(2\pi f t + \phi), & (6.21)\\
A(s) &= \alpha \cdot (1+\beta s)(s-1)(s-1)s^2, & (6.22)\\
\phi &= \phi_0 + k, & (6.23)\\
k &= -2\pi\tau_{tail} s. & (6.24)
\end{aligned}
$$

with $\alpha = 0.4862$, $\beta = -0.1329$, $\tau_{tail} = 0.2326$ and $\phi_0 = 0.5986$, the parameter of adaptation. The result exposed as a 3D shape can be seen in Fig. 6.20. This moment will be used in the following Chapter to see if it is possible to generate a similar swimming gait by direct actuation of the body with this actuation torque pattern.

6.4 Conclusion

In conclusion, this chapter validates the force calculation method for a continuous deformable body with the same formulation as in the first part of this work concerning only rigid articulated bodies. The hydrodynamic effort are still valid even if the characteristic function overlap through the mollification zone. Another result is that the method remains valid if the body has a non-solenoidal deformation velocity field.

This method is really a huge improvement compared to usually used method that recovers the effort via the vorticity at the wall, i.e. in a region of high gradients, and the solution of a specific Poisson equation for the pressure at the wall. Indeed this method only involve integrals computation on the body that are really simple to implement and computationally less expensive than the resolution of the Poisson equation.

We were also able to show that the method allowed to find the actuation efforts necessary to produce a particular swimming gait by isolating the part related to the penalization of the effort computation. This is a great advance in the field and allows to study the efficiency of a swimming gait kinematic according to a chosen criterion (low energy consumption, fast, silent gait).

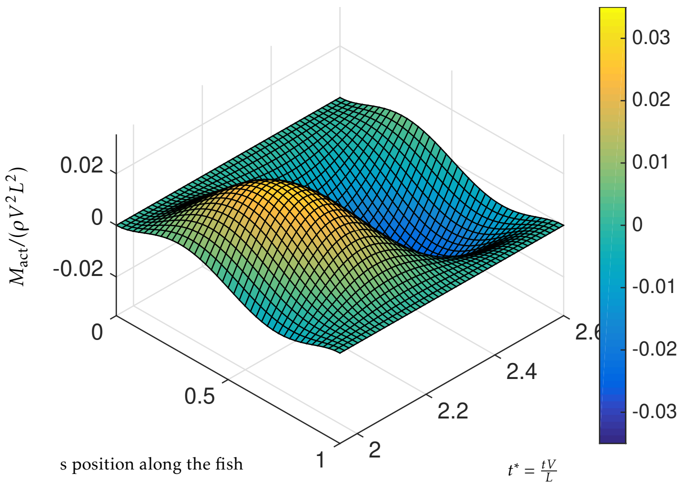

(a) Global view

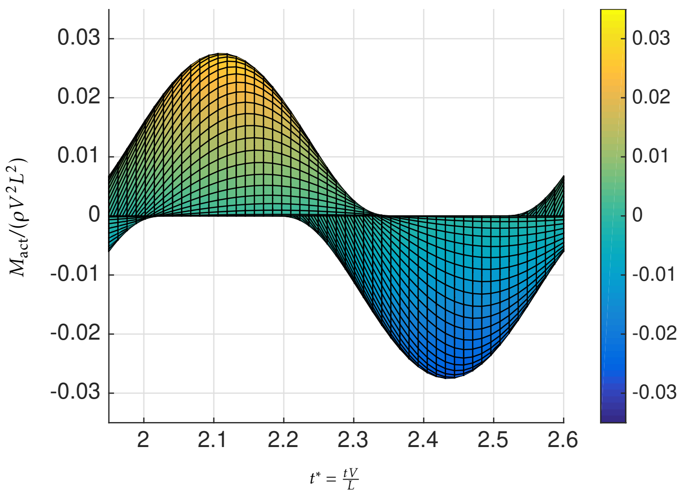

(b) Side view

Figure 6.20: Anguilliform swimmer: extraction of actuation moment needed for this motion configuration.

Chapter 7

Direct dynamics actuation of continuous bodies

This Chapter is devoted to the upgrade of the algorithm presented in Chapter 2 so that it can be adapted to a body with continuous deformations. Being able to reproduce bodies undergoing continuous deformation is interesting to better study the mechanisms of fluid-solid interaction in a biological way. Indeed, living organisms interacting with fluid are all deformable bodies. The first algorithm presented is not able to take into account articulated systems whose segments deform and overlap. This difference in the body definition influence the masses and inertias that must be used as well as the way the velocity field is calculated.

As in the previous method, the structure will be composed of different sub-bodies connected by means of rotational joints. These different sections will deform in order to guarantee that the body remains in one piece. This approach is very close to what is found in nature where the bodies of anguilliform swimmers are discretized in the spine by a finite number of segments, while still having a continuous skin. The changes made to the code are explained in the first Section.

In Section 7.2, we characterize this new method. We reproduce the swimming pattern presented in section 6.2 using the prescribed deformation mode of this new solver. To achieve this, we fit the angular profiles as well as their first and second derivatives to mathematical functions, based on the lateral deformation of the mid-line. The results show that our solver is able to reproduce a motion very close to the reference.

The last part of this Chapter is devoted to the study of the actuation moments necessary for generating the motion. To do this, we proceed by steps. First we observe the moments extracted from the simulation with prescribed kinematics and we compare them to the actuation moments retrieved with inverse dynamics analysis in the last section of the previous Chapter. We then proceed to two controlled tests by replaying the code in "direct dynamics" mode, i.e. without prescribing the deformation of the swimmer. The two test cases that we created are a very simplified version of a biomechanical simulator for anguiliform swimmer: continuous body and direct dynamics.

The first scenario is a pure feed-forward control where the swimmer movement is obtained by direct integration of the torque patterns. In the second one, we created a test where feed-forward and feed-back control are coupled in order to stabilize the resulting motion.

The last section of this chapter is devoted to pilot study of a different swimming scenario aiming at opening new avenues of simulations with the developed solver.

7.1 Extension to continuous systems

We here modify the algorithm presented in Section 2.4.4 in order to treat an articulated continuous system of deforming elements with embedded actuation. The body is discretized in segments connected via rotational joints. The segments deform in order to guarantee that the body remains in one piece. This entails the computation of hydrodynamic forces and moments on each deforming element of the structure to solve the dynamics of the degrees of freedom related to the body joints. In this section, we detail and discuss the addition to the main algorithm: the new description of the body articulated structure, the multi-body system (MBS) updated solver and the computation of the hydrodynamic efforts on the new setup from the penalization (Section 2.2) and projection (Section 2.3) schemes.

7.1.1 Free articulated system

We focus on a two-dimensional MBS composed of N linked rigid bodies, here more complex elements are used that can adapt to the deformation of each joints in order to ensure a continuous body (Fig. 7.1, $N = 3$). Each joint entails a degree of freedom that is represented by a generalized coordinate q_i, i.e. the angle between two successive elements. The three first coordinates, q_1, q_2, q_3, also describe the floating base, providing the global structure with the three translational

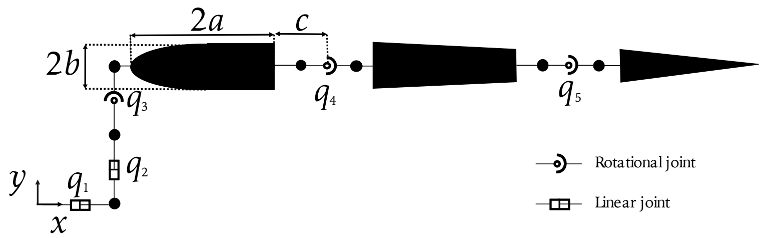

Figure 7.1: Continuous actuation scheme : Multi-body diagram of three segmented eel-like structure: floating base generalized coordinates, q_1, q_2, q_3, and the joints generalized coordinates, q_4, q_5; $2a$ the lenght, $2b$ the width and c the distance from the tip to the hinge joint of each element here set to 0 in order to have a continuous structure.

and rotational degrees of freedom related to the x, y plane. The articulated structure is then described by the generalized coordinates: $\mathbf{q} = [q_1\ q_2 ...\ q_n]^T$, with $n = N + 2$. The footprint of the structure in space is then described by a set of characteristic functions, $\chi_{s,j}$, each one representing a cutting element j, as in Eq. (A.1).

The geometrical aspect of the two dimensional swimmer is the same as in the previous Chapter, see Section 6.1.1. The cut between the segments is done at the middle of each transition in between generalized coodinates, $q_4\ q_5 ...\ q_{n-1}$ as represented in Fig. 7.3. This is done using a mollification parameter to create for each segment a characteristic function as it is presented in Fig. 7.2. If we sum all the characteristic functions the result will be equal to the characteristic function of the whole body without cutting edges and the transition in between the segments will not be visible.

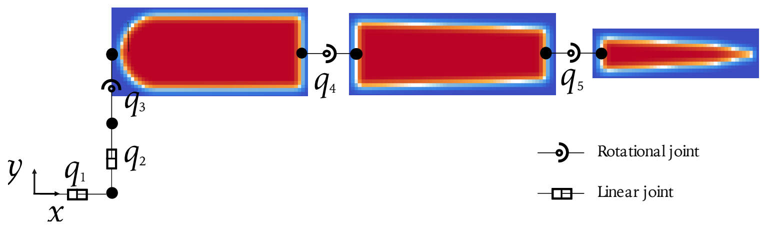

Figure 7.2: Free articulated system : Zoom on the characteristic function of 3 segments. Blue represent the absence of body where the characteristic function equals zero and red the present the body where the characteristic function equals 1. The transitioning colors represent the mollification zone where the characteristic function goes from 1 to zero gradually.

7.1.2 Multi-body dynamics equations

In this new scheme the only difference comes from the fact that the Inertia, $\mathbf{I}_j$, and the mass, m_i of each sub-element will be different and that they will change with time. It will only affect the inertia matrix, $\mathbf{D}(\mathbf{q})$ but we consider that this is negligible since we will take small elements subject to very small changes. Indeed, we can show that if we assume that at the transition between two segments the thickness of the section remains constant then the variation of inertia and mass is equal to zero, see Fig. 7.3.

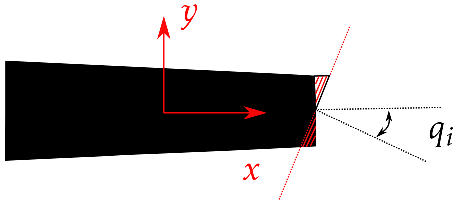

Figure 7.3: Multi-body dynamics equations : zoom on one deforming segment where the dashed red line show the transition between two segment of the structure. The hatched red zone represent the part that must be removed or added to the new deformed segment.

Moreover, we do not take into account the elasticity of the body structure in this thesis, i.e. there is no resistance to deformation due to the body's inherent structure which could come from the skin, tendons and other biological elements. This can be added in a later version of the code.

7.1.3 Computational aspects

It is the same algorithm as presented in the second Chapter (see Algorithm 1) except that we take into account the divergence of the deformation velocity field. The changes are highlight in red compared to the former algorithm. There is also a difference in the way that the deformation velocity field is computed. Each segment has its own velocity field, $\mathbf{u}_s$, they are then combined via the use of each characteristic function, $\mathbf{u}_{s,tot} = \sum \chi_{s,i} u_{s,i}$, see Eqs. (7.13) and (7.14). This guarantees a smooth transition of the velocity field in between segments.

Eqs. (7.1), (7.2), (7.4) and (7.5) differ from the original Algorithm 1 and make it possible to take into account the non-solenoidal deformation velocity field. In Eq. (7.1), the deformation velocity field, $\mathbf{u}^n_{def}$, is computed based on the function $momentFree()$ characterized by

Algorithm 3 Coupled Method for continuous actuated body

WHILE $t^n \leq T_{end}$

Step 1 : Velocity update

$$\mathbf{u}^n_{def} = momentFree(\chi^n_s, u^n_{s,tot}) \tag{7.1}$$

$$\sigma^n = \chi^n_s(\nabla \cdot \mathbf{u}^n_{def}) \tag{7.2}$$

$$\nabla^2 \psi^n = -\omega^n \tag{7.3}$$

$$\nabla^2 \varphi^n = \sigma^n \tag{7.4}$$

$$\mathbf{u}^n = \nabla \times \psi^n + \nabla \varphi^n \tag{7.5}$$

$$\|\nabla \mathbf{u}^n\| \Delta t^n \leq LCFL \text{ and } \Delta t^n \leq \frac{h^2}{2\nu} \tag{7.6}$$

Step 2 : Projection forces

$$\mathbf{p}^{*,n+1}_{proj} = \int_{\Omega_{mat}} \rho_f \chi^n_s \mathbf{u}^{n+1} d\mathbf{x} \quad \text{with} \quad \mathbf{F}^{n+1}_{proj} = \frac{\mathbf{p}^{*,n+1}_{proj} - \mathbf{p}^{*,n}_{proj}}{\Delta t^n} \tag{7.7}$$

$$\mathbf{l}^{*,n+1}_{proj} = \int_{\Omega_{mat}} \rho_f \chi^n_s \,(\mathbf{x} \times \mathbf{u}^{n+1})\, d\mathbf{x} + \mathbf{x}^n_{cm} \times \mathbf{F}^{n+1}_{proj} \quad \text{with} \quad \mathbf{M}^{n+1}_{proj} = \frac{\mathbf{l}^{*,n+1}_{proj} - \mathbf{l}^{*,n}_{proj}}{\Delta t^n} \tag{7.8}$$

Step 3 : Time integration of the MBS

$$\boldsymbol{\tau}^{n+1}_{stat} = \mathcal{F}(\mathbf{F}^{n+1}_{stat}, \mathbf{M}^{n+1}_{stat}) \tag{7.9}$$

$$\boldsymbol{\tau}^{n+1}_{hyd} = \mathcal{F}(\mathbf{F}^{n+1}_{proj} + \mathbf{F}^n_{pen}, \mathbf{M}^{n+1}_{proj} + \mathbf{M}^n_{pen}) \tag{7.10}$$

$\boldsymbol{\tau}^{n+1}_{act}$ provided by a control law

$$D(\mathbf{q})\ddot{\mathbf{q}} + C(\mathbf{q}, \dot{\mathbf{q}})\dot{\mathbf{q}} = \boldsymbol{\tau}^{n+1}_{hydro} + \boldsymbol{\tau}^{n+1}_{act} + \boldsymbol{\tau}^{n+1}_{stat} \tag{7.11}$$

Compute $\mathbf{q}^{n+1}$ and $\dot{\mathbf{q}}^{n+1}$ for $t^{n+1} = t^n + \Delta t^n$

$$\chi^{n+1}_s = \mathcal{G}(\mathbf{q}^{n+1}) \tag{7.12}$$

$$\mathbf{u}^{n+1}_s = \mathcal{H}(\mathbf{q}^{n+1}, \dot{\mathbf{q}}^{n+1}) \tag{7.13}$$

$$\mathbf{u}^{n+1}_{s,tot} = \sum \chi^{n+1}_s \mathbf{u}^{n+1}_s \tag{7.14}$$

Step 4 : Penalization

$$\mathbf{u}^{n+1}_\lambda = \frac{\mathbf{u}^n + \lambda \Delta t \chi^{n+1}_s \mathbf{u}^{n+1}_{s,tot}}{1 + \lambda \Delta t \chi^{n+1}_s} \tag{7.15}$$

$$\omega_\lambda = \nabla \times \mathbf{u}^{n+1}_\lambda \tag{7.16}$$

$$\mathbf{F}^{n+1}_{pen} = \int_\Omega \lambda \rho_f \chi^{n+1}_s (\mathbf{u}^{n+1}_\lambda - \mathbf{u}^{n+1}_s) d\mathbf{x} \tag{7.17}$$

$$\mathbf{M}^{n+1}_{pen} = \int_\Omega \lambda \rho_f \chi^{n+1}_s \mathbf{x} \times (\mathbf{u}^{n+1}_\lambda - \mathbf{u}^{n+1}_s) d\mathbf{x} + \mathbf{x}^{n+1}_{cm} \times F^{n+1}_{pen} \tag{7.18}$$

Step 5 : Time integration of the vorticity field

$$\frac{\partial \omega_\lambda}{\partial t} = \nu \nabla^2 \omega_\lambda - \nabla \cdot (\mathbf{u}_\lambda \omega_\lambda) \tag{7.19}$$

$$\omega^{n+1} = \omega^{n+1}_\lambda \tag{7.20}$$

$$t^{n+1} = t^n + \Delta t^n$$

$$n = n + 1$$

ENDWHILE

$$\begin{aligned}
\mathbf{u}_T^n &= \frac{1}{Mass}\int \rho^n \chi_s^n \mathbf{u}_{s,tot}^n \, d\mathbf{x}, && (7.21)\\
\dot{\Theta}^n &= \frac{1}{Inertia}\int \rho^n \chi_s^n (\mathbf{x}-\mathbf{x}_{cm}^n)\times \mathbf{u}_{s,tot}^n \, d\mathbf{x}, && (7.22)\\
\mathbf{u}_R^n &= \dot{\Theta}^n \times (\mathbf{x}-\mathbf{x}_{cm}^n), && (7.23)\\
\mathbf{u}_{def}^n &= \mathbf{u}_{s,tot}^n - \mathbf{u}_T^n - \mathbf{u}_R^n, && (7.24)
\end{aligned}$$

where $\mathbf{x}_{cm}$ represent the position of the center of mass and $\dot{\Theta}^n$ represent the angular velocity of the swimmer at the center of mass.

This code would require optimization through better computational techniques in the treatment of the various fields, especially the characteristic functions and the velocity fields, because for the moment the code is very memory intensive.

7.2 Validation with imposed kinematics

In this section, we only use prescribed kinematics simulations. To validate the deformation motion pattern and the resulting global movement, we use as reference the simulation from Gazzola et al. [5]. To validate the hydrodynamic and actuation moments, we use as reference the simulation from Verma et al. [43]. The same lateral displacement of the mid-line are applied on the two references but the fluid properties differ as explained in the previous Chapter.

7.2.1 2D self-propelled anguilliform swimmer

Based on this new algorithm, a comparison between our methodology and the method of Gazzola et al. [5] is presented for the simulation of 2D self-propelled anguilliform swimmers. The motion pattern used for this validation is described by the lateral displacement of the mid-line, $y_s(s,t)$, as in Eq. (6.1).

The only difference relies on the parameterization of the motion imposed to the new scheme of deformation. Indeed, we only have access to the generalized coordinates and not the lateral displacement of the mid-line. In Fig. 7.4, we show the deformation of the body mid-line where dy can be found via the formulation Eq. (6.1) along s. This allows to compute the angle corresponding to the general coordinates already mentioned in Fig. 7.1 by calculating

$$\theta_i = a\sin(\frac{dy}{ds}) \qquad (7.25)$$

$$q_i = \theta_i - \theta_{i-1}. \qquad (7.26)$$

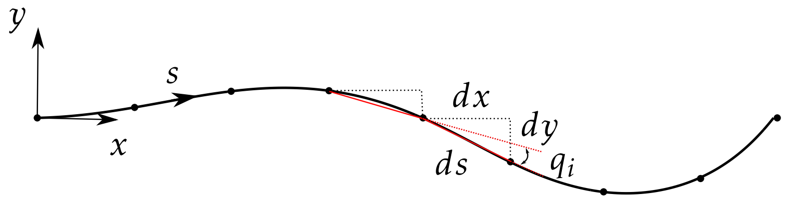

Figure 7.4: Continuous actuation scheme : midline segmentation principle.

In Fig. 7.4, a slight difference of position at the end of the body can be possible as we impose the body to keep a constant length (see the different position of the bullet and the mid-line of the body). This will always induce a difference in the resulting motion, that will have to be taken into account and discussed.

All simulations are started with the body at rest and the motion is initialized by gradually increasing the displacement magnitude (through a sinusoidal function used on the rising quarter of its period) from zero to its designated value during the first cycle. We set the viscosity of the fluid to be $\mu = 1.4\ 10^{-4}$, the body length to be $L = 1$ and the density to be $\rho_{fluid} = \rho_{body} = 1$. The volume is conserved, therefore fluid and body densities are the same and the baroclinic term drops out.

Simulations are carried out on a rectangular domain $[0,4L]\times[0,4L]$ with a resolution of 2048×2048 grid, $LCFL = 0.01$, $\lambda = 1/dt$, and $\epsilon = h$.

Results

Fig. 6.4 depicts the unsteady forward (u_x, solid line) and lateral (u_y, dashed line) velocities of the center of mass of the body, normalized by L. Similar dynamics are observed but a slight difference can be explained by the notable variation in the motion applied. The lateral and angular (not shown) velocities in the steady regime also agree both in amplitude and phase.

Two curves are visible: one for 8 segments swimmer and one of 16 segment swimmer. The only notable difference between these two curves is that the one with 16 segments allows a more smooth velocity. We can see that the oscillations are more rounded than in the case of 8 segments which is closer to the reference.

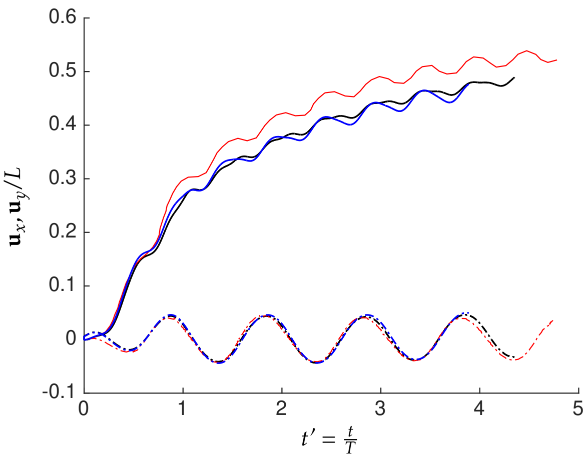

Figure 7.5: Validation with imposed kinematics: Forward velocity u_x/L (solid lines), lateral velocity u_y/L (dashed lines). Black and blue lines indicate 2D swimmer simulations with the proposed method, black for an 8 segments swimmer and, blue, 16 segments. Red lines reproduce the results from Gazzola et al. [5].

7.2.2 Simplified generation of movement

For future simulations, it would be useful to have a mathematical expression of the angular pattern of the generalized coordinates q_i that corresponds to the "typical" body deformation provided in Eq. (6.1). This is motivated by the simplification of the implementation of the several controllers that will be needed in the next section. We have exported the angles q_i assigned to each coordinates for a 8 segmented body and we have approximated these angles with a simple sinusoidal function whose amplitude and phase shift vary, see Fig. 7.6 :

$$\begin{aligned} q_i &= A_i \cos(2\pi \frac{t}{T} - \frac{\pi}{9} + \varphi_i) \qquad (7.27) \\ \text{with } A &= [\ 0.194 \quad 0.235 \quad 0.289 \quad 0.349 \quad 0.413 \quad 0.481 \quad 0.551\ ] \\ \text{and } \varphi &= [\ \tfrac{6.7\pi}{4} \quad \tfrac{5.5\pi}{4} \quad \tfrac{4.2\pi}{4} \quad \tfrac{3.2\pi}{4} \quad \tfrac{2\pi}{4} \quad \tfrac{\pi}{4} \quad 0.0\ ]. \end{aligned}$$

To verify that this approximation works we have reproduced the simulation of the swimmer from [5]. Fig. 7.7 shows the comparison of the velocities between the movement with the original angles in black and the simplified movement in blue. This shows that the simplified motion is very close to the original motion and that we can use it for further investigations.

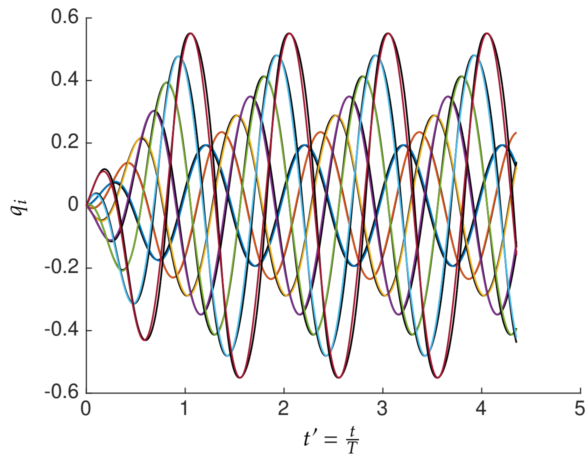

Figure 7.6: Simplified generation of movement: generalized coordinates motion q_i from the complete simulation in black, mathematical model given in Eq. (7.27) in color.

Here the simulation is carried out on a rectangular domain $[0, 4L] \times [0, 4L]$ with a resolution of 1024×1024 grid, $LCFL = 0.01$, $\lambda = 1/dt$, and $\epsilon = h$.

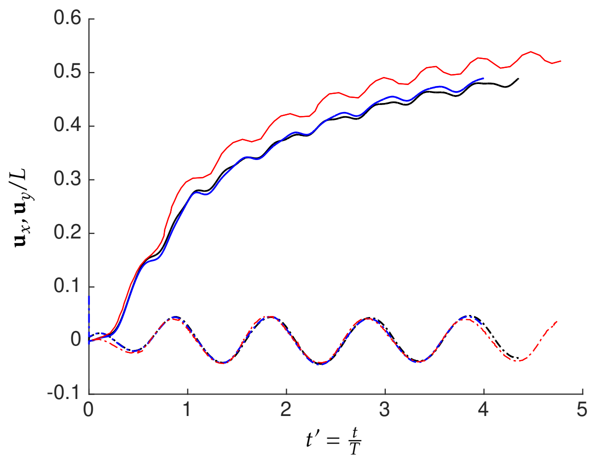

Figure 7.7: Simplified generation of movement: Forward velocity u_x/L (solid lines), lateral velocity u_y/L (dashed lines). Black lines indicate 2D swimmer simulations with the proposed method for an 8 segments swimmer. Blues lines account for the results obtained with the complex motion resolution and red lines account for the results from Gazzola et al. [5].

7.2.3 Extraction of actuation moments from imposed deformations

Now we look at the actuation torque needed to imposed this motion for the simulation parameters presented in Section 6.3. We use the configuration where we impose the kinematics in order to extract the torque by using the inverse dynamics of the system. The inverse dynamics requires solving for the term $\boldsymbol{\tau}_{\text{act}}$ in the equation of the dynamics presented in Chapter 2 :

$$\boldsymbol{\tau}_{\text{act}} = \mathbf{D}(\mathbf{q})\ddot{\mathbf{q}} + \mathbf{C}(\mathbf{q},\dot{\mathbf{q}})\dot{\mathbf{q}} - \boldsymbol{\tau}_{\text{hyd}}. \tag{7.28}$$

As a reminder, this simulation is done with viscosity of the fluid set to $\mu = 2.5e^{-}6$, the body length $L = 0.1$; it is carried out on a rectangular domain $[0,4L]\times[0,4L]$ with a resolution of 1024×1024 grid, $LCFL = 0.01$, $\lambda = 1/dt$, and $\epsilon = h$. Fig. 7.8 reports the velocity profile compared to the test of Verma et al. [43].

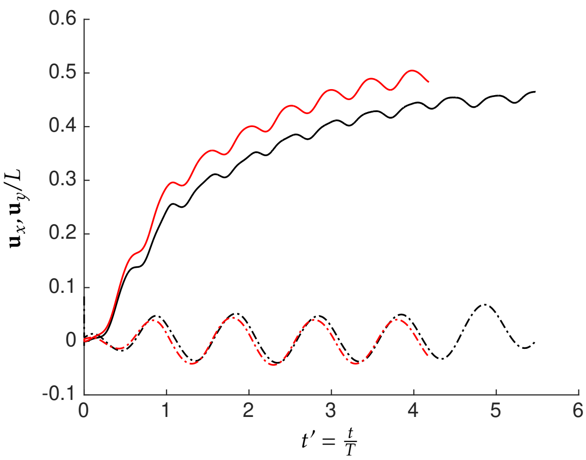

Figure 7.8: Continuous actuation scheme: Forward velocity u_x/L (solid line), lateral velocity u_y/L (dashed line). Black lines indicate 2D swimmer simulations with the proposed method and red lines account for the results from Verma et al. [43].

In Fig. 7.9, the actuation torque of each joint inside the swimmer (q_4, ... ,q_{N+2}) needed to achieve motion is pictured, both in 3D view and as a function of time. If we compare to the torque extracted form the theoretical mapping (from Section 6.3.2) that we repoduced in Fig. 7.10 with the same color map, we can see that the torque from this simulation is not quite smooth but remains in the same range of values especially if we look at the last period of motion between $t^* = [6;8.5]$. What we can also see is that the acceleration phase at the beginning of the movement does require a higher torque amplitude.

In Fig. 7.11, we can see the difference between the torque from the inverse dynamics and the theoretical torque again with the same color map. The gait frequency is visible but it is dominated by higher mode of noise.

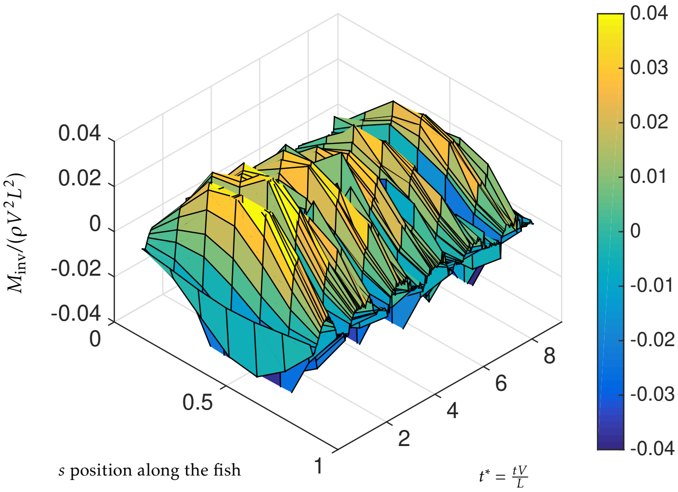

(a) 3D view

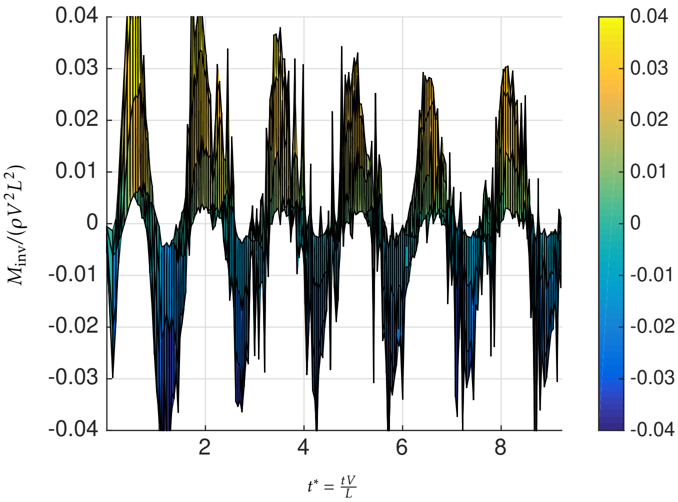

(b) Side view

Figure 7.9: Extraction of moment actuation from imposed deformations: extraction of actuation moment via the inverse dynamics of motion.

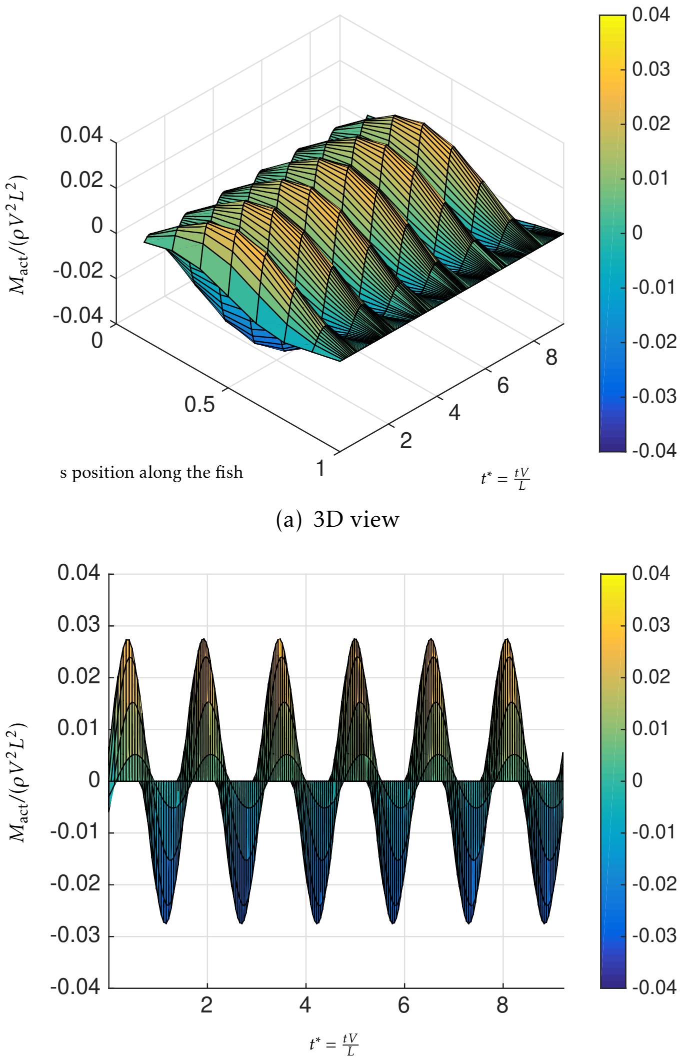

(a) 3D view

(b) Side view

Figure 7.10: Extraction of moment actuation from imposed deformations: theoretical torque extracted from Section 6.3.2 with more periods to match the simulation case.

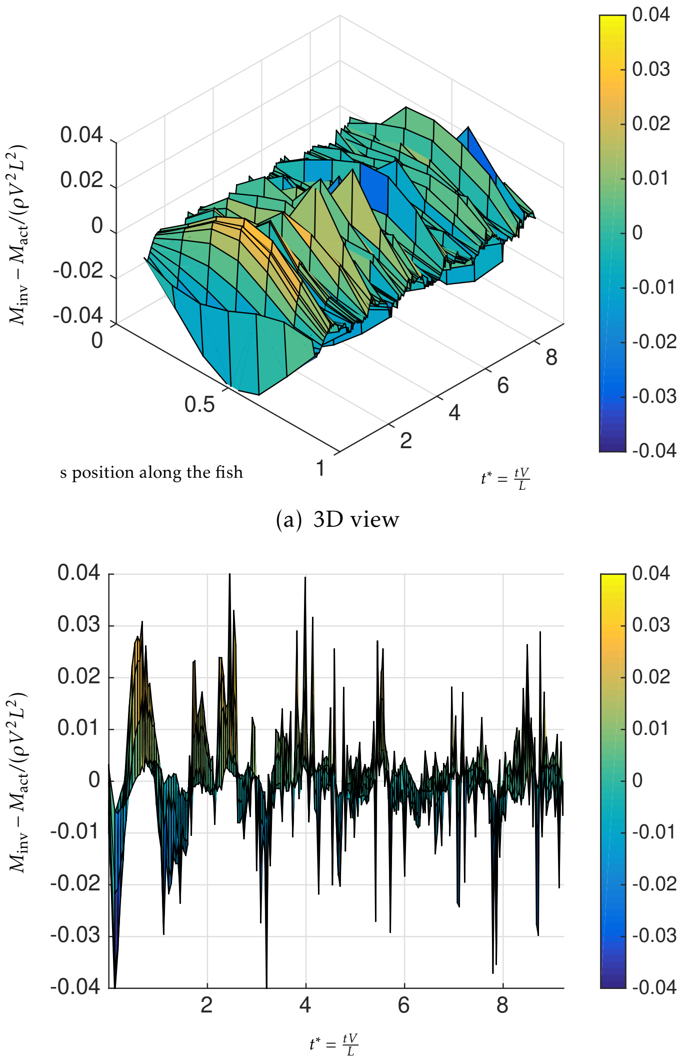

(a) 3D view

(b) Side view

Figure 7.11: Extraction of moment actuation from imposed deformations: difference between the actuation torque issue from the inverse dynamics and the theoretical actuation torque.

7.3 Moments reintroduction in the new framework

The aim of this Section is to give the actuation moments extracted on the mid-line of the swimming continuous fish in Section 6.3 to the new model without imposing the kinematics of deformation. The model is set in direct dynamics mode and is free to respond to actuation torques and hydrodynamics efforts.

To study the response of the new algorithm, we are going to make several tests. At first, we will make a simple test by giving to the swimmer only the theoretical moments that we will call for now on the feed-forward moments/torques. For this test, we expect that the feed-forward control is not stable and that the swimmer will not be able to reach the same speed nor a stable propulsion. Indeed, the feed-forward moments were fitted on the steady operation of the swimmer where it reaches constant velocity and is, thus, not able to carry out the start up phase. As we showed in last section the torque amplitude must be higher for the start-up phase.

In a second step, we add a feed-back component to the feed-forward one which will help to stabilize the movement on the basis of a reference motion which is the one presented in the Section 7.2.2. This will allow the swimmer to get closer to the prescribed kinematic swimming curve. We will be able to show that the feed-back torque is very noisy but that this is not the main component of torque. Remember that for this test we only have an approximation of the reference movement due to the discretization of the body, as explain in Section 7.2, and not the exact movement of the midline, Eq. (6.1), unfortunately this will introduce error in the feed-back.

The fluid parameters and dimensions stays the same as in the test of Verma et al. [43], the viscosity of the fluid is set to $\mu = 2.5e^{-}6$, the body length to be $L = 0.1$ and the density is still $\rho_{fluid} = \rho_{body} = 1$, resulting in a Reynolds number of approximately 2600, given the final swimming velocity. All simulations are started with the body at rest and the motion is initialized with a sinusoidal trigger. Simulations are carried out on a rectangular domain $[0, 4L] \times [0, 4L]$ with a resolution of 1024×1024 grid, $LCFL = 0.01$, $\lambda = 1/dt$, and $\epsilon = h$.

7.3.1 New framework : feed-forward control

In this test, as we have already mention, we control the swimmer only by providing the torque extracted from Section 6.3.3, defined as the feed-forward torque, $\boldsymbol{\tau}_{i,ff}$,

$$
\begin{aligned}
\frac{\tau_{\mathrm{i,act}}(s(i),t)}{(\rho V^2 L^2)} &= \frac{\boldsymbol{\tau}_{i,ff}}{(\rho V^2 L^2)} = A(s(i))\sin(2\pi f t + \phi), && (7.29)\\
A(s) &= \alpha \cdot (1 + \beta s(i))(s(i) - 1)(s(i) - 1)s^2(i), && (7.30)\\
\phi &= \phi_0 + k, && (7.31)\\
k &= -2\pi\tau_{tail} s(i). && (7.32)
\end{aligned}
$$

with $\alpha = 0.4862$, $\beta = -0.1329$, $\tau_{tail} = 0.2326$ and $\phi_0 = 0.5986$, the parameter of adaptation.

We made this simulation to see how the structure will react without any stabilization from a feed-back signal except the fluid around the structure.

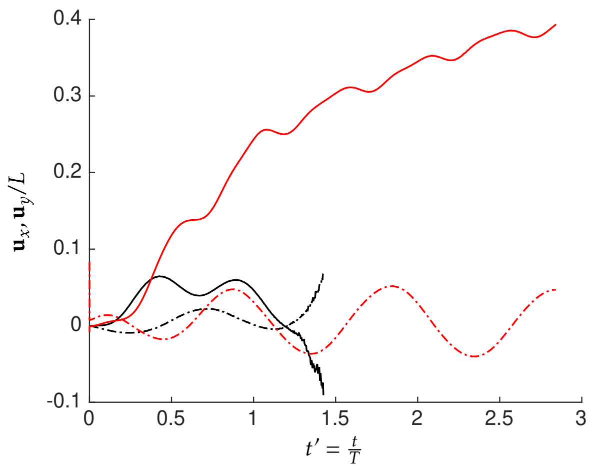

Figure 7.12: Feed-forward control: Forward velocity u_x/L (solid lines), lateral velocity u_y/L (dashed lines). Black lines indicate 2D swimmer simulations with feed-forward control for an 8 segments swimmer. Red lines account for the results obtained with the imposed motion resolution.

We can see in Fig. 7.12 that the swimmer manages to accelerate in the longitudinal direction at the very beginning and then reach or a short moment $u_x/L = 0.5$ to finally be completely destabilized. This can be seen in more detail when you look at the generalized coordinates of the Figs. 7.13(a) and 7.13(b). Indeed, the position of two joints goes to extremes and is not regulated. In other words the feed-back only realized by the hydrodynamic efforts is not sufficient in this set-up to stabilize the swimming mode in a pure feed-forward case. In Fig. 7.14, we can observe the swimmer deformation and it is clear for the last time sequence that the fish is reaching a state that the solver could not treat as the segment are too much overlapping.

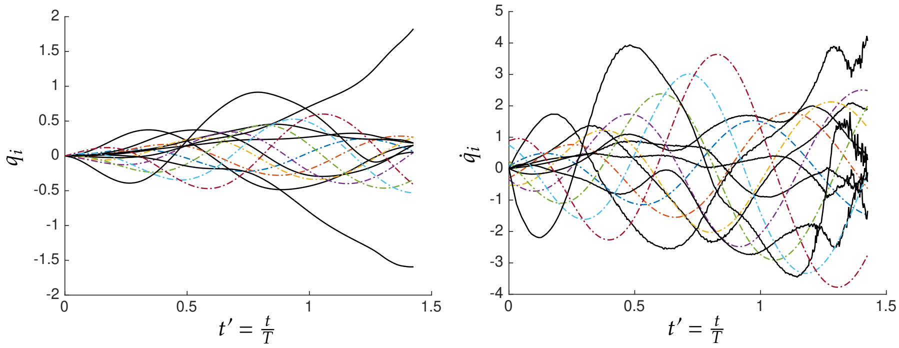

(a) Motion q_i (b) Velocities $\dot{q}_i$

Figure 7.13: Feed-forward control: generalized coordinates present results, black, comparison to the approximation from Section 7.2.2, in colors.

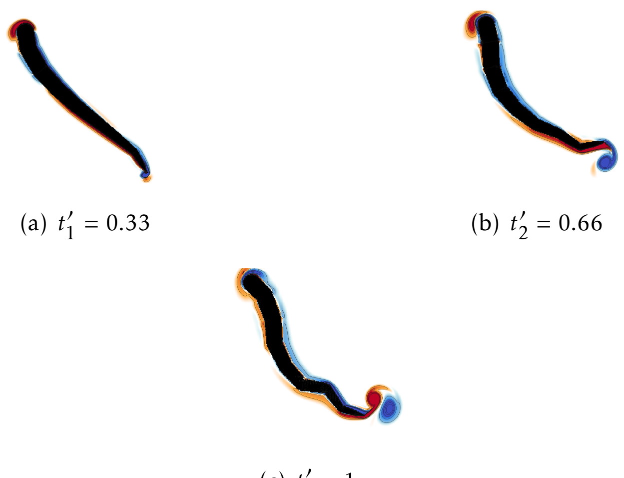

(a) $t'_1 = 0.33$

(b) $t'_2 = 0.66$

(c) $t'_3 = 1$

Figure 7.14: Feed-forward control: vorticity snapshots at different normalized times: $t' = t/T$. Negative and positive vorticity are denoted in blue and red respectively.

7.3.2 Combined feed-forward and feed-back control

In this section, we stabilize the control in feed-forward with a feed-back action that will be realized with a proportional controller,

$$\boldsymbol{\tau}_{i,act} = K_p'(q_{i,ref} - q_i) + \boldsymbol{\tau}_{i,ff};$$

where $q_{i,ref} = A_i \cos(2\pi \frac{t}{T} - \frac{\pi}{9} + \varphi_i)$ with A_i and φ_i form Eq. (7.27) the the reference motion, $K_p = \frac{K_p'}{\rho V^2 D} = 0.190$ the dimensionless proportional coefficients, and, $\boldsymbol{\tau}_{i,ff}$ the feed-forward torque component. K_p was chosen to be the lowest to ensure a good tracking of the chosen kinematic.

The feed-back control is only there to stabilize the swimmer, so it should be very small or of an order of magnitude smaller than the feed-forward torque. On the Fig. 7.15, we can see that the feed-back stabilization allows to reach almost the same swimming speed as when the simulation is done with prescribed kinematics.

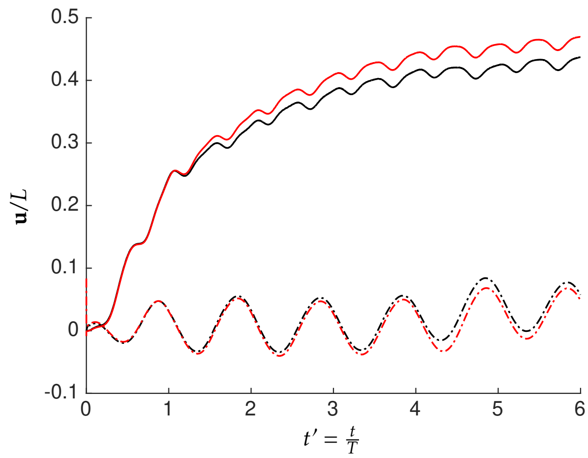

Figure 7.15: Continuous actuation scheme: Forward velocity u_x/L (solid line), lateral velocity u_y/L (dashed line). Black lines indicate 2D swimmer simulations with the proposed method and red lines account for the results of the present method but with imposed kinematics.

Indeed the values of the generalized coordinates q_i, see Fig. 7.16, reach well the same values in position although their speed is a little noisy leading to a slight difference on the average speed of the swimmer in the last cycles of movement.

- Figs. 7.17 shows the actuation torque obtained by the inverse dynamics of the system.
- Figs. 7.18 shows the torque generated by the feed-back control.
- Figs. 7.19 shows the torque given by feed-forward controller.

All these visualizations have been made with the same color bar to guarantee a better comparison between them.

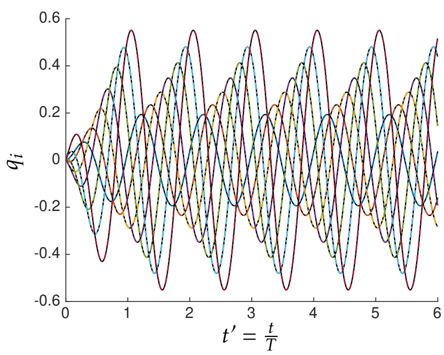

(a) Motion q_i

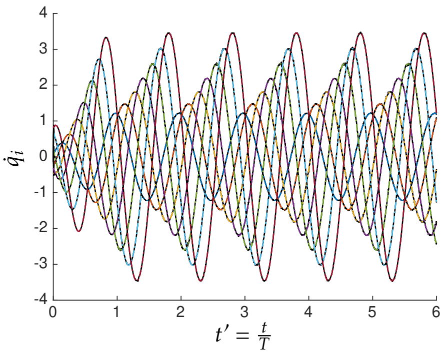

(b) Velocities $\dot{q}_i$

Figure 7.16: Anguilliform swimmer: generalized coordinates present results, black, comparison to the approximation from Section 7.2.2, in colors.

What we observe is that the main component of the inverse torque is indeed the feed-forward torque as can be seen by comparing Figs. 7.17(b) (feed-back) and 7.19(b) (feed-forward). However, this inverse torque is very noisy as it was the case in the prescribed kinematics simulation (see Fig. 7.9). These noises are therefore compensated by the feed-back torque which is also very noisy. If we now look at the top view of the 3D graphs we can see that the feed-back has also changed the position of the torque amplitude peak compared to the feed-forward torque. Indeed we can see on the figure Fig. 7.17(c) that the peak in yellow is more at $0.65L$ along the length of the swimmer rather than at the center of the swimmer as it was the case of the imposed kinematics simulation.

We have to be careful that here we do not have exactly the right reference motion because as we said in the Section 7.2, the body being sectioned in a rough way, we cannot give exactly the same reference motion in the feed-back component since it has a constant length. This means that the feed-back torque can never cancel and is of the

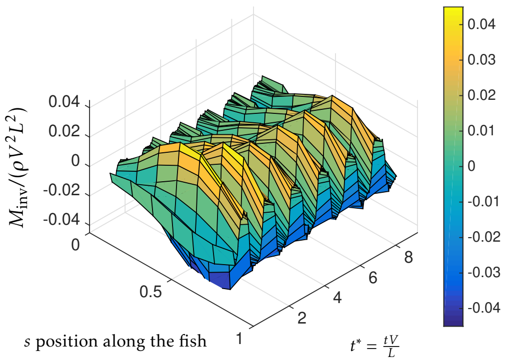

(a) 3D view

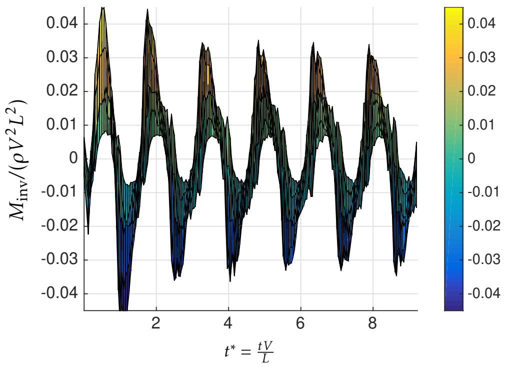

(b) Side view

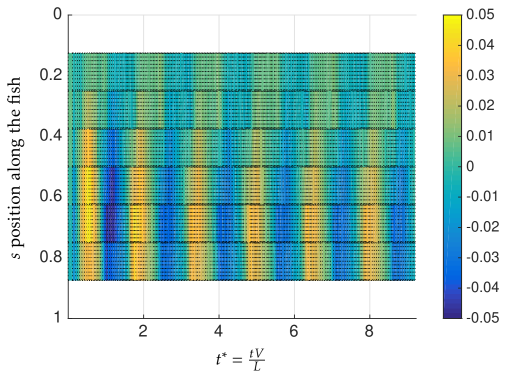

(c) Top view

Figure 7.17: Anguilliform swimmer: extraction of actuation moment via the inverse dynamics, the color bar represent the moment amplitude for each subfigure.

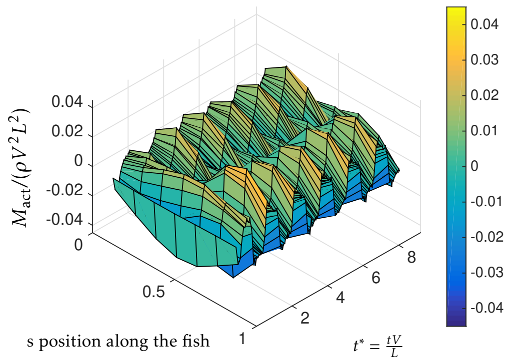

(a) 3D view

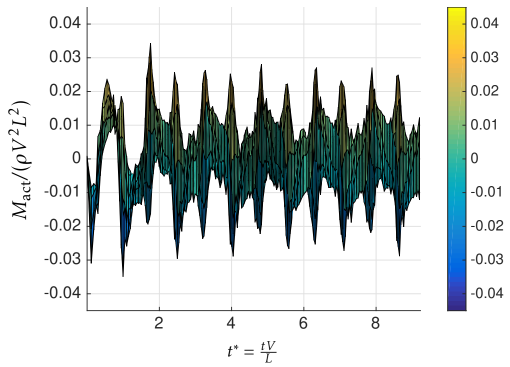

(b) Side view

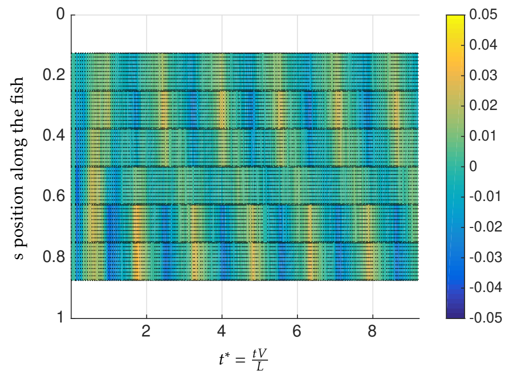

(c) Top view

Figure 7.18: Anguilliform swimmer: extraction of actuation moment provided by the feed-back controller, the color bar represent the moment amplitude for each subfigure.

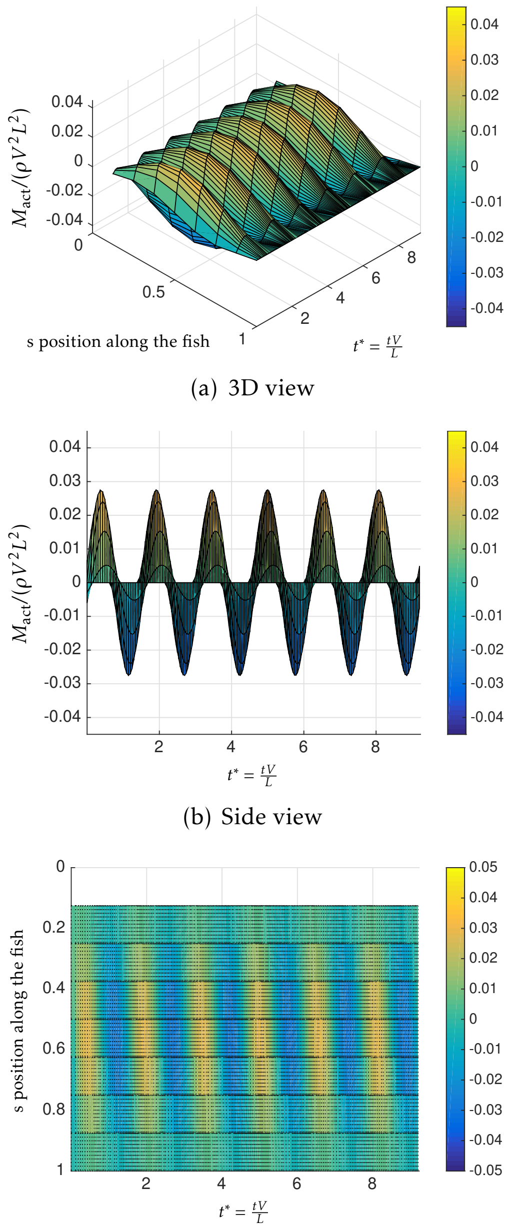

(c) Top view

Figure 7.19: Anguilliform swimmer: extraction of actuation moment provided by the feed-forward component, the color bar represent the moment amplitude for each subfigure.

same order of magnitude as the feed-forward torque. We only impose a proportional control which implies that the deformation speed of the joints is not checked. This has also an influence on the importance of the feed-back torque.

7.4 Analytical swimming gait

In this new test case, we impose a new reference motion and the swimmer is discretized with 5 segments ($N = 5$), it has thus 4 joints, to observe the differences from the previous test case and see if it works with more segments. We use a controller with only a feed-back action because we did not extract the actuation torque needed for this specific reference motion. This controller is realized with a proportional controller,

$$\boldsymbol{\tau}_{i,act} = K_p'(q_{i,ref} - q_i);$$

with $K_p = \frac{K_p'}{\rho V^2 D} = 40$ the dimensionless proportional coefficients. This coefficient is chosen in order to be lowest to ensure a good tracking of the desired kinematic.

$$q_{i,ref} = -\alpha \cdot (\frac{s_i}{L} + b_a)/(1 + b_a)\sin(2\pi(\frac{s_i}{L} - \frac{t}{T})) \cdot (1 - \frac{1}{e^t}). \tag{7.33}$$

with $b_a = 0.25$, $T = 1.0$ and $\alpha = 1.0$

The fluid parameters and dimensions stay the same as in the test of Verma et al. [43], the viscosity of the fluid is set to $\mu = 2.5e^{-}6$, the body length to be $L = 0.1$ and the density is still $\rho_{fluid} = \rho_{body} = 1$. The simulation is started with the body at rest and the motion is initialized with a sinusoidal trigger. Simulations are carried out on a rectangular domain $[0, 4L] \times [0, 4L]$ with a resolution of 1024×1024 grid, $LCFL = 0.01$, $\lambda = 1/dt$, and $\epsilon = h$.

In Fig. 7.20, we can observe the speed profile reached by the swimmer. It reaches a higher velocity but has higher oscillation amplitude. It seems to benefit from higher generalized coordinates amplitude of motion as it is shown in Fig. 7.21.

In Fig. 7.22, we can observed the torque needed to achieved the swimming gait. The torques has a higher amplitude and if we compare the top views, Fig. 7.22(c), has the same patterns as Fig. 7.18(c).

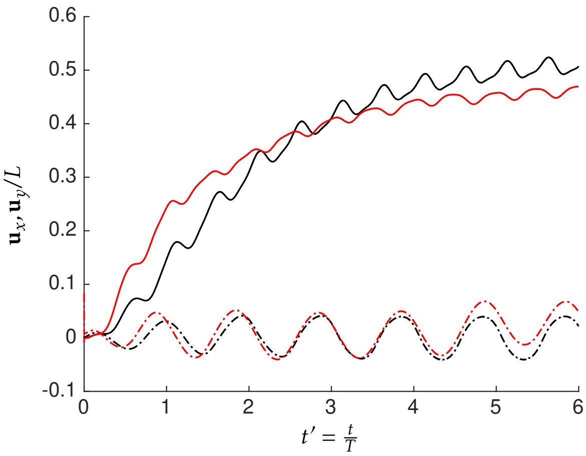

Figure 7.20: Continuous actuation scheme: Forward velocity u_x/L (solid line), lateral velocity u_y/L (dashed line). Black lines indicate 2D swimmer simulations with the proposed method and red lines account for the results of the present method but with imposed kinematics.

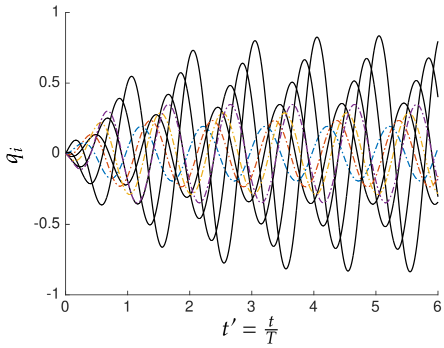

Figure 7.21: Continuous actuation scheme: generalized coordinates positions, q_i, present results, black, comparison to the approximation from Section 7.2.2 adapted for 5 segments, in colors.

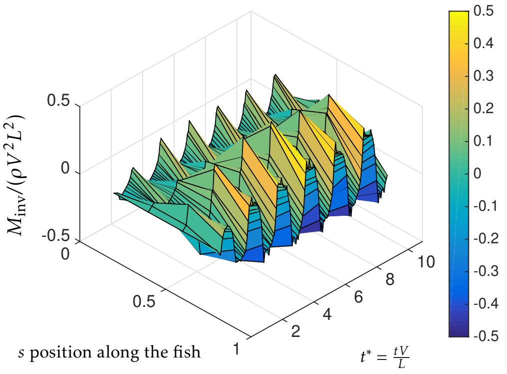

(a) 3D view

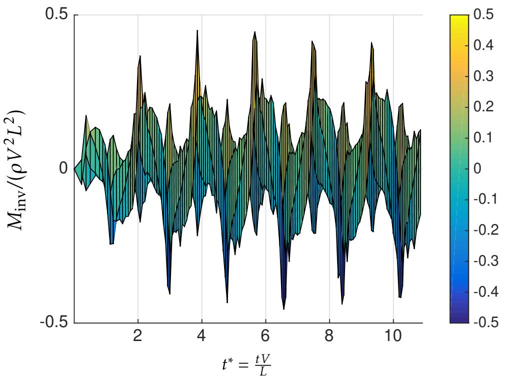

(b) Side view

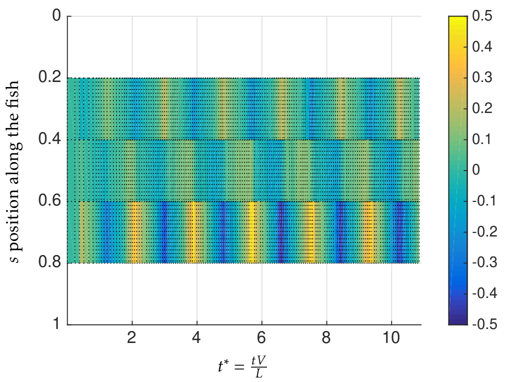

(c) Top view

Figure 7.22: Anguilliform swimmer: extraction of actuation moment via the inverse dynamics of motion, the color bar represent the moment amplitude for each subfigure.

We now look at the Cost of Transport of this motion compared to the case "Combined feed-forward and feed-back control". The CoT indicates the energy spent per unit distance traveled and is defined following the definition found in [68] :

$$CoT(t) = \frac{\int_{t-T}^{t} max(P_{act}, 0)\, dt}{\int_{t-T}^{t} \|\mathbf{u}\|\, dt} \tag{7.34}$$

In Fig. 7.23, we can see that the Cot of the "Combined feed-forward and feed-back control" is less energy demanding than the specific propulsion motion. The swimmer consume more energy per unit of distance with four actuators. The CoT is flatter and more stable in the reference motion than for the present result, this means that the motion presented here has not yet reached a constant speed propulsion.

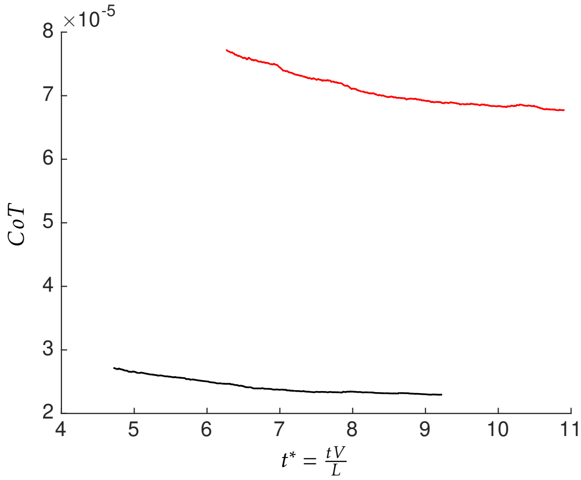

Figure 7.23: Anguilliform swimmer: Cost of transport, present result for the specific motion in black and reference result from the case "Combined feed-forward and feed-back control" in red.

7.5 Conclusion

In this Chapter, we introduced a new variant of the methodology in which continuous deformable bodies can be solved. These continuous bodies can deform via the use of prescribed kinematics or actuation torques. We have shown that this variant is able to reproduce a reference motion with prescribed kinematics. The torques extracted from that exercise showed a very good coherence with the theoretical result found in the previous Chapter, even though the ones extracted in this chapter were very noisy.

The new solver allows the application on the continuous body of the torque formula extracted in the previous chapter. We showed that if it is applied alone to the body, it is not sufficient to guarantee a given swimming gait. If we want to reach the same swimming gait, it is necessary to add a stabilizing term to the torque component. Here, we tested a proportional feed-back term on the position. This allowed extracting the feed-back torque from the solver, as expected the feed-back torque helps mainly the swimmer to start but it seems also to change the amplitude peak of the total torque function necessary for the movement, which is no longer in the middle of the body but at 3/4 of it.

Finally, we showed a last swimming test where the number of segments is changed and where the torques given to the segment follow another function. In this case the swimmer manages to reach a higher swimming speed.

Chapter 8

Conclusions and perspectives

8.1 Conclusions

In this manuscript, we have developed a Fluid-Structure-Actuation Interaction solver for free-swimming problems based on the combination of a Vortex Particle-Mesh method with a Multi-Body System solver. Because it needs to time-integrate the dynamics of the actuated system too, the solver constitutes a marked departure from the force-free approach originally proposed in the works of [5, 33, 36] and thus enables investigations of structural internal dynamics including complex kinematic constraints (e.g. rotational joints, linear rails, *etc*). It indeed has to recover hydrodynamic forces and moments; this is achieved through a procedure that exploits the results of the intermediate steps of penalization and projection.

The resulting approach was applied to benchmark cases of increasing complexity: the sedimentation of a 2D cylinder, a comparison with vorticity-based Noca formulas, the flow past an elastically-mounted circular cylinder, a free swimming articulated fish and the problem of passive propulsion within the wake of a bluff body. The method is shown to reproduce reference results and accurately capture the coupled dynamics of the flow and the articulated structure.

The approach was then applied to the motion of an articulated eel-like harvester in the wake of a cylinder where the harvesting process is achieved by damper-like elements. We performed a series of simulations to identify a maximum power recovery and concurrently studied the interaction between the fluid mechanics of the cylinder-harvester system and the power recovery. Our test configuration, in spite of its simple geometry, is an effective test-bed for the investigation of dynamically-rich harvesting problems. It has indeed shown some interesting features: a tuned uniform damping allows the harvester to achieve 88% of Betz's optimum while a spatially-varying damping allows to harvest energy more uniformly over the device. These performances are promising as they hint at the efficient combination of power production and flow control, through drag reduction and lift stabilization.

We have also developed a bio-inspired control framework for self-propelled swimmers evolving in complex flows. This framework relies on three nested control layers controlling the motion of a self-propelled swimmers in the wake of a cylinder. The swimmer equipped with vorticity sensor near his head is able to feel the complex environment. The resulting approach has been applied to several scenarios of increasing complexity. The swimmer indeed had to maintain a stationary position in a uniform flow or exploit the wake of an obstacle, which was first stationary then mobile. Results showed that the swimmer saved 3.2 - 12.6 % energy when it evolved within a wake rather than in a uniform flow.

We validated the use of forces on a continuous and deformable body by comparing our results to the original algorithm of Gazzola et al. [5]. We also show that this new method is able to extract the necessary actuation torques in order to achieve a certain swimming kinematics.

We adapted the method presented in the first part to extend it to a continuous body. We show that our method allows to reproduce a similar motion with the same imposed kinematics. The new algorithm is now able to extract and impose actuation torques on a continuously deformable body. Actuation torques extracted from a specific kinematics that are applied to a swimmer with the same morphology enables to reproduce a very close swimming gait if they are stabilized by a feedback component. We also show that the use of the torques alone does not allow the reproduction of the same swimming gait.

8.2 Discussion

In Section 1.2, we identified a series of research questions to be addressed in the present thesis. We begin this discussion by enumerating again these research questions, and outlining how we believe the thesis has contributed to address them. In the first part of this manuscript, Chapter 2 to 5, we focused on the first two research questions that we mentioned in the introduction, namely

- *Is VPM method suited to retrieve the hydrodynamics efforts (forces and moments) applied to a fixed or moving, deformable or rigid body ?*

  In Chapter 2, we presented the method that addresses this question. We found a correct formulation of the hydrodynamic efforts by integrating already available quantities. Two contributions to this hydrodynamic efforts were exposed : the penalization and the projection term. The penalization contribution is obtained by integrating the Brinkman penalization constraint included in the Navier-Stokes equations on the body surface. The projection contribution is identified as the momentum gained by the system when the fluid evolves freely over the whole domain – i.e. like if no body was there – according to the current velocity field.

- *Can these efforts be introduced in an actuation scheme described by means of a multi-body system governing the deformation and motion of articulated rigid bodies in a fluid?*

  In Chapter 2, we described the method applying the hydrodynamic efforts to a multi-body system of rigid bodies. Then in Chapter 3, we validate the framework on well documented reference test cases showing the efficiency of the method to reproduce the same dynamics.

This method handles complex interactions with the environment as presented in the example of Chapter 4 and 5. We have shown that the algorithm can be adapted in order to be a competing technique in the identification of wake effects, in comparison to other formalisms. Furthermore, this approach easily enables the extraction of all the actuation and hydrodynamic efforts that takes place in the mechanism without any supplementary computation. By using VPM method, we surpass the capabilities of analytical fluid dynamics solvers used in robotic design [9, 39, 40] to capture the environment of the swimmer at the cost of longer simulations.

A critical limitation of the method is that it cannot handle continuous actuated bodies. For this reason, actuation is provided by virtual actuators that are actually not embodied in the very body structure. Therefore, in the second part of this manuscript, Chapter 6 and 7, we focused on the last two research questions, namely

- *Can this method recover the actuation forces of a continuous deforming body in a fluid?*

In Chapter 6 and in Appendix C, we show that the code is able to extract the necessary actuation torques in order to achieve a specific swimming kinematics. The penalization contribution in the hydrodynamic efforts computation correspond to the inverse of the actuation.

In this chapter, the deformation are prescribed and are not the result of the underlying dynamic interactions. The dynamic coupling between the swimmer and the fluid is computed only on the whole deformed body. The purpose of this chapter was precisely to compute the hydrodynamic and actuation torques distributed along the fish in order to compare them with the literature where prescribed deformations are also used. It shows that the efforts computation method is still valid on continuous body swimmer and that the distribution of hydrodynamic efforts along the center line of the fish is really close to the result identify in other studies like [43].

- *Can this method be used to create a dynamic control scheme for an articulated continuous body moving in a fluid?*

  In Chapter 7, we adapt the method presented in the first part to extend it to a continuous body. We show that our method allows to reproduce a similar motion with the same imposed kinematic than in previous chapter. The new algorithm is also able to resolve the direct dynamics on continuously deformable body. We manage to impose actuation torques extracted from a specific swimming gait to a new swimmer and it reproduce a kinematics very close to the reference one. This is only possible if the actuation torque applied is augmented by the use of a stabilizing feedback component.

The last results from Chapter 7 are obtained by the use of an approximation of the prescribed movement and thus are not exactly reproducing the same deformations as in Chapter 6. This induced differences observed in the results comparing Sections 6.2 and 7.3.2. Also the method does not accurately reproduce the deformation velocity field of the continuous swimmer since it is computed on each sub-element. The velocity transition between each sub-element is then not continuous even if it was mollified with the same properties as the definition as the body surface. Although the deformations velocity field is not perfectly continuously defined the body of the swimmer is closed and continuous.

8.3 Perspectives

The present work focused on the Direct Numerical Simulation of moderate Reynolds number cases but nothing precludes the present methodology from higher Reynolds number cases. One should however use care in the handling of the penalization and projection techniques: (i) penalization will likely have to be quite stiff to remove spurious flows inside the body (one might then use an iterative penalization as in Hejlesen et al. [34] and Gillis et al. [35]); (ii) the grid will be finer in order to ensure that the thickness of the mollified region is small compared to the boundary layer around the body; (iii) the accuracy of the momentum flux, as calculated over the pseudo-time step of the projection, will probably lead to more severe constraints on the spatial and temporal resolutions. On the topic of time integration, we note that the method in its current state achieves a low temporal convergence order. One could either extend the method to multi-step schemes by using intermediate evaluations of the projection and penalization terms or use the above-mentioned iterative penalization to better capture added mass effects.

The present methodological contribution has a broader scope than vortex particle methods. Indeed, the hydrodynamic force extraction procedure can readily be transposed to the original velocity-pressure-based penalization context, as introduced by Angot et al. [31]. It does also constitute a potential breakthrough for the robust handling of actuated and deformable structures, either position- or torque-controlled. It can be readily applied to the study of the interactions between a system, either artificial or biological, and its fluid environment and bring some new interesting questions and prospects.

First, there are perspectives regarding the first part of this work, i.e. dealing with disconnected elliptical sub-bodies.

- a 3-D implementation of the algorithm is an interesting prospect as it will enable easier comparison with real robotic devices evolving in a fluid environment. The transition is quite straightforward, as it does not entail any stencil modification or deep methodological changes;

- this framework allows to envision applications for the design of robotic swimmers and the control of their actuation, the study of neuromuscoluskeletal systems and gait generation. This tool could be used in the investigation of control schemes and motion generation mechanisms to produce efficient and robust swimming gaits;

- from a biological viewpoint, our algorithm also enriches the toolbox of the experimentalist, for example in order to study sensory pathways recruited in swimming locomotion control. In particular, our framework could be used in order to highlight the way fishes perceive their environment with different sensory modalities (pressure line, velocity sensor, ...) and how they manage to adapt their behavior in order to exploit this sensory information in an optimal way.

There is more fundamental developments being still required regarding the second algorithm presented in this manuscript, i.e. the one dealing with continuous bodies. In particular, we believe that our results will be more faithful to those from other fields of research if the following directions are explored;

- Thorough sensitivity analyses could be performed in order to better characterize the solver developed in this work. The analyses could concern the following elements:
  - the effect of larger mollification region on the deformation velocity field and body definition;
  - an analytical definition of the prescribed reference motion in order to correctly capture the difference between the reference simulation with prescribed deformation and the dynamically coupled one;
  - the convergence properties of the methodology by performing temporal and spatial convergence studies on simple test-cases.
- The code could benefit from a computational study to make the resolution faster with a better consideration of the different velocity fields and characteristic function.
- Moreover, we do not take into account the elasticity of the body structure, i.e. there is no resistance to deformation due to the body's inherent structure which could come from the skin, tendons and other biological elements. This can be added in a later version of the code to study the interplay between compliance and actuation in the locomotion mechanism.

As an outcome of those enhancements, the dream simulation environment would allow studying the flow around a continuously actuated swimmer sensing the flow and evolving in a perturbed fluid with specific target positions to be reached in the domain. The underlying challenge would be to optimize its movement in order to harvest energy from the environment and reach a optimum efficiency. This multi-layered simulation framework will then open the doors towards new studies on sensing and control for robotic swimmer and energy harvesting applications. This is of potential interest for a vast amount of industrial fields that are concerned by interactions between fluid and solid structures.

8.4 Acknowledgements

The present research benefited from computational resources made available on the Tier-1 supercomputer of the Fédération Wallonie-Bruxelles, infrastructure funded by the Walloon Region under the grant agreement n^o1117545. Caroline Bernier was funded by a FSR fellowship of Université catholique de Louvain for the project COMPACT-SWIM (FSR 2013).

Appendix A

Vortex method for fluid structure interaction

In this Appendix, more details are given on the main computational steps for the vortex method formerly developed by [5].

A.1 Brinkman penalization details

The immersed object shapes are described by a mollified characteristic function, χ_s. This function is built upon a level set function that specifies the signed distance to the surface of the body, d. The mollified characteristic function is evaluated as

$$\chi_s = \begin{cases} 0 & d < -\epsilon \\ 1/2[1 + \frac{d}{\epsilon} + \frac{1}{\pi}\sin(\pi\frac{d}{\epsilon})] & |d| \leq \epsilon \\ 1 & d > \epsilon \end{cases} \tag{A.1}$$

where ϵ is the mollification length. For moderate Reynolds numbers, ϵ should be a small fraction (about 1%) of the characteristic length of the body geometry. This geometry information is carried by a specific deformable grid; this allows to interpolate the color function onto the computational mesh in a flexible manner (see [5] for further details).

A.2 Splitting

For the sake of completeness, all the operations performed in this method are summarized in the global Algorithm 4. In this Algorithm, a first order Godunov splitting approach is used in order to solve Eq.

(2.7). Given the penalized vorticity field Eq. (A.7), the first step is to solve for the baroclinic term Eq. (A.8) then diffuse the vorticity strength Eq. (A.9) and finally advect the particules Eq. (A.10). It also highlights and explains the force-free character in the treatment of the fluid-structure interaction, as it handled as an exchange of momentum, or integrals of the fluid forces over a time step (Eqs. (A.3)-(A.4)).

Algorithm 4 Original method

WHILE $t^n \leq T_{end}$

χ_s^n given deformation

$\mathbf{u}_{DEF}^n$ given deformation velocity field

$\sigma = \chi_s^n(\nabla \cdot \mathbf{u}_{DEF}^n)$

$$\rho^n = \rho_s^n \chi_s^n + \rho_f(1 - \chi_s^n) \tag{A.2}$$

$\nabla^2 \psi^n = -\omega^n$

$\nabla^2 \phi^n = \sigma^n$

$\mathbf{u}^n = \nabla \times \psi^n + \nabla \phi^n$

$$\mathbf{u}_T^n = \frac{1}{M_s} \int_\Sigma \rho^n \chi_s^n \mathbf{u}^n \, d\mathbf{x} \tag{A.3}$$

$$\dot{\theta}^n = \frac{1}{J_s^n} \int_\Sigma \rho^n \chi_s^n (\mathbf{x} - \mathbf{x}_{cm}^n) \times \mathbf{u}^n \, d\mathbf{x} \tag{A.4}$$

$$\mathbf{u}_R^n = \dot{\theta}^n \times (\mathbf{x} - \mathbf{x}_{cm}^n) \tag{A.5}$$

$$\mathbf{u}_\lambda^n = \frac{\mathbf{u}^n + \lambda \Delta t \chi_s^n (\mathbf{u}_T^n + \mathbf{u}_R^n + \mathbf{u}_{DEF}^n)}{1 + \lambda \Delta t^n \chi_s^n} \tag{A.6}$$

$$\omega_\lambda^n = \nabla \times \mathbf{u}_\lambda^n \tag{A.7}$$

$$\frac{\partial \omega_\lambda^n}{\partial t} = -\frac{\nabla \rho^n}{\rho^n} \times \left(\frac{\partial \mathbf{u}_\lambda^n}{\partial t} + (\mathbf{u}_\lambda^n \cdot \nabla) \mathbf{u}_\lambda^n \right) \tag{A.8}$$

$$\frac{\partial \omega_\lambda^n}{\partial t} = \nu \nabla^2 \omega_\lambda^n \tag{A.9}$$

$$\frac{\partial \omega_\lambda^n}{\partial t} + \nabla \cdot (\mathbf{u}_\lambda^n \omega_\lambda^n) = 0 \tag{A.10}$$

$\omega^{n+1} = \omega_\lambda^{n+1}$

$\mathbf{x}_{cm}^{n+1} = \mathbf{x}_{cm}^n + \mathbf{u}_T^n \Delta t^n$

$\theta^{n+1} = \theta^n + \dot{\theta}^n \Delta t^n$

$t^{n+1} = t^n + \Delta t^n$

ENDWHILE

Appendix B

Hydrodynamic forces

In this section, the hydrodynamic contact forces between the body and the fluid are computed. We first focus on the effort exerted by the fluid at the boundary of a volume Ω. The resulting force and moment are expressed as

$$\begin{aligned} \mathbf{F}^c &= \int_{\delta\Omega} \sigma \cdot \mathbf{n} dS; \\ \mathbf{M}^c &= \int_{\delta\Omega} \mathbf{x} \times (\sigma \cdot \mathbf{n}) dS. \end{aligned}$$

Through the Green's theorem, both expression $\mathbf{F}^c$ and $\mathbf{M}^c$ are readily simplified as

$$\begin{aligned} \mathbf{F}^c &= \int_{\delta\Omega} \sigma \cdot \mathbf{n} dS \\ &= \int_{\Omega} \nabla \cdot \sigma dV; \end{aligned} \tag{B.1}$$

and

$$\mathbf{M}^c = \int_{\delta\Omega} \mathbf{x} \times (\sigma \cdot \mathbf{n}) dC$$
$$M_i^c = \int_{\delta\Omega} (\varepsilon_{ijk}\, x_j\, n_l\, \sigma_{lk}) dC$$

Through the Green's theorem, the expression becomes

$$= \int_{\Omega} \frac{\partial}{\partial x_l} (\varepsilon_{ijk}\, x_j\, \sigma_{lk}) dV$$
$$= \int_{\Omega} \varepsilon_{ijk} \frac{\partial x_j}{\partial x_l}\, \sigma_{lk}\, dV + \int_{\Omega} \varepsilon_{ijk} x_j \frac{\partial \sigma_{lk}}{\partial x_l}\, dV$$

The first term vanishes by symetry of the strain tensor, σ, i.e.

$$\mathbf{M}^c = \int_{\Omega} \mathbf{x} \times (\nabla \cdot \sigma) dV. \tag{B.2}$$

We now focus on the Navier-Stockes equations in their conservative form

$$\rho_f \frac{D\mathbf{u}}{Dt} = \nabla \cdot \sigma + \rho_f \lambda (\mathbf{u}_s - \mathbf{u}). \tag{B.3}$$

The combination of Eqs. (B.1), (B.2) and (B.3) gives the following expressions:

$$\begin{aligned}
\mathbf{F}^c &= \int_{\Omega} \left(\rho_f \frac{D\mathbf{u}}{Dt} + \rho_f \lambda (\mathbf{u} - \mathbf{u}_s) \right) dV \\
&= \frac{d}{dt} \int_{\Omega_{mat}} \left(\rho_f \mathbf{u} \right) dV + \int_{\Omega} \left(\rho_f \lambda (\mathbf{u} - \mathbf{u}_s) \right) dV; \qquad \text{(B.4)} \\
\mathbf{M}^c &= \int_{\Omega} \mathbf{x} \times \left(\rho_f \frac{D\mathbf{u}}{Dt} + \rho_f \lambda (\mathbf{u} - \mathbf{u}_s) \right) dV
\end{aligned}$$

Following the Reynolds transport theorem, it becomes

$$= \frac{d}{dt} \int_{\Omega_{mat}} \mathbf{x} \times \left(\rho_f \mathbf{u} \right) dV + \int_{\Omega} \mathbf{x} \times \left(\rho_f \lambda (\mathbf{u} - \mathbf{u}_s) \right) dV \tag{B.5}$$

And we retrieve the equations used in Section 2: Eqs. (2.17) and (2.18).

Appendix C

Motion control test case

In this appendix, we highlight the different types of simulations that we used though the manuscript : imposed kinematics, torque control using pure feed-back and torque control using feed-forward coupled to feed-back useful for stability reason. This allow us to dissociate the influence of the two components, penalization and projection, of the hydrodynamic efforts presented in Section 2.4.3.

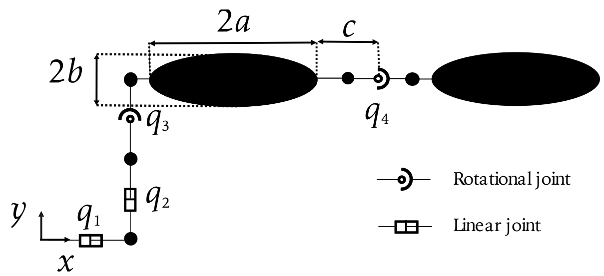

Figure C.1: Motion control test case: two segmented stucture description : floating base generalized coordinates, q_1, q_2, q_3, and the joints generalized coordinates, q_4, q_5; $2a$ the lenght, $2b$ the width and c the distance from the tip to the hinge joint of each element.

We consider a structure composed of two ellipses with an aspect ratio of $\frac{a}{b} = 10$. The distance that separates a hinge from the ellipse tips c is taken equal to $0.05a$ (see Fig. C.1). We based our control on a reference motion described by

$$q_{4,\mathrm{ref}}(t) = 0.45\ \sin(2\pi t/T). \tag{C.1}$$

with $T = 5$. The present study considers the bodies as neutrally-buoyant ($\frac{\rho_f}{\rho_s} = 1$).

The characteristic length and velocity scales used for the non-dimensionalization are respectively $L = 0.42$ and $U = \dot{q}_{4,max} = 0.56$. The common Reynolds number in this study is $Re = \frac{UL}{\nu} = 1176$. The simulation uses a computational domain size of $[0;4\,L] \times [0;2\,L]$ discretized by a 768×384 grid. The following numerical parameters for VPM and the penalization are used: LCFL = $2.0\,10^{-2}$, $\epsilon = 2h$, $\lambda = 1.0\,10^{4}$.

C.1 Imposed kinematics

For the imposed kinematics case, we impose the motion and velocity of the generalized coordinates q_4 to follow $q_{4,ref}$. The floating base dynamics is then solved following the hydrodynamic efforts and the articulation dynamics. The torque needed for actuation is then recover through the inverse dynamics by inverting the equation Eq. (2.13) :

$$\begin{aligned} \boldsymbol{\tau} = \boldsymbol{\tau}_{\text{hyd}} + \boldsymbol{\tau}_{\text{act}} &= \mathbf{D}(\mathbf{q})\ddot{\mathbf{q}} + \mathbf{C}(\mathbf{q},\dot{\mathbf{q}})\dot{\mathbf{q}} \\ \boldsymbol{\tau}_{\text{act,imposed}} &= \mathbf{D}(\mathbf{q})\ddot{\mathbf{q}} + \mathbf{C}(\mathbf{q},\dot{\mathbf{q}})\dot{\mathbf{q}} - \boldsymbol{\tau}_{\text{hyd}}. \end{aligned}$$

C.2 Pure feed-back control

The pure feed-back control is achieved by imposing the actuation torque, $\boldsymbol{\tau}_{act,4}$, in order to follow the desired kinematic through a PD controller:

$$\boldsymbol{\tau}_{act,4} = k_p \cdot (q_{4,\text{ref}} - q_4(i)) + k_d \cdot (\dot{q}_{4,\text{ref}} - \dot{q}_4). \tag{C.2}$$

where $k_p/(\rho V^2 L) = 0.0298$ and $k_d/(\rho V^2 L) = 3.7229 \cdot 10^{-4}$ are respectively the proportional and the derivative coefficients.

C.3 Combined feed-forward and feed-back control

The feed-forward associated to the feed back controller is achieved by adding the feed-foward component to the same controller as in the previous section :

$$\boldsymbol{\tau}_{act,4} = \boldsymbol{\tau}_{ff} + k_p \cdot (q_{4,\text{ref}} - q_4(i)) + k_d \cdot (\dot{q}_{4,\text{ref}} - \dot{q}_4). \tag{C.3}$$

where $\boldsymbol{\tau}_{ff} = \boldsymbol{\tau}_{\text{act, 4,imposed}}$ is extracted from the imposed kinematics test. In this approach, we preferred using an analytic fitted curve to describe $\boldsymbol{\tau}_{ff} = A \cdot \cos(2\pi t/T + \phi)$ for easier computational aspect. k_p and k_d are the same than in the previous section.

C.4 Results

First we compare the results form the imposed kinematic case with the pure feed-back control. The resulting motion over the course of three undulation periods appears to be in very good agreement with the reference curve see Fig. C.2. We see that the imposed movement is well followed with the selected control gains.

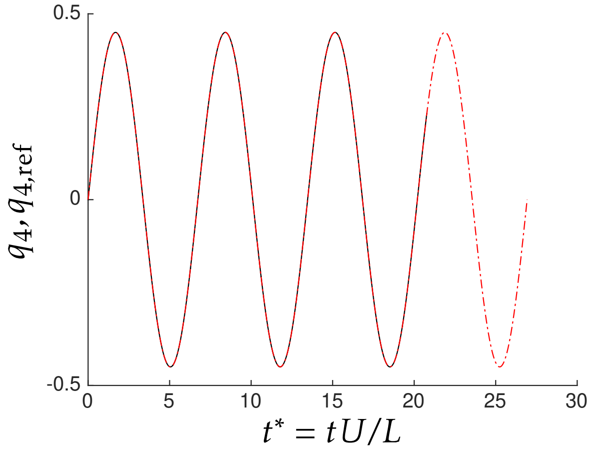

Figure C.2: Motion control test case: angle of inclination, q_4 between the two bodies : imposed kinematic, dashed red; pure feed-back, solid black .

In Fig. C.3, we can compared the resulting actuation moment needed to achieved this motion, τ_{act}. We see that the two approaches reach the same moment to accomplish the same movement. Based on this result, we can extract a feed-forward component for the next control scheme, τ_{ff}, here shown in yellow. This curve is characterized by this analytic formula :

$$\frac{\tau_{ff}}{\rho V^2 L^2} = 5.6375 \cdot 10^{-5} \cdot \cos(2\pi t/5 + \pi/3). \tag{C.4}$$

This component is supposed to be sufficient to provide the right actuation moment except for the start-up phase. This is visible in Fig. C.4, where we can see the result of the feed-forward coupled to feedback test. The feed-back action is really reduced (solid black curve) and is activated only at start-up and in the sharp transitions.

Fluid moments exerted by the fluid on the central joint is shown in Fig. C.5 and also the component extracted from the projection step and penalization step. This result show that the penalization component of the hydrodynamic penalization moment correspond to inverse

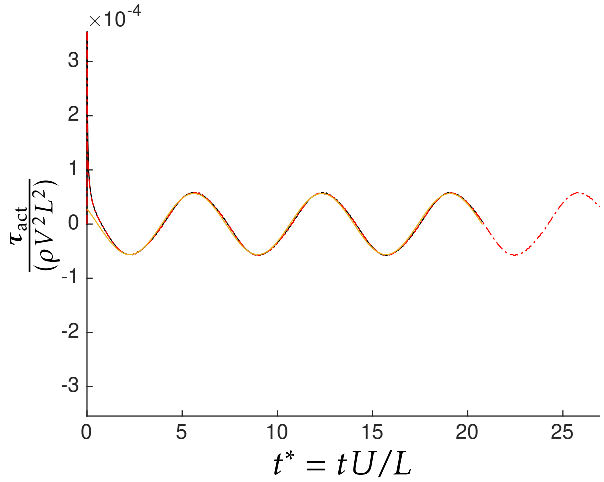

Figure C.3: Motion control test case: actuation moment under various control scheme: imposed kinematic, dashed red; pure feed-back, solid black; curve fitting along the moment, solid yellow.

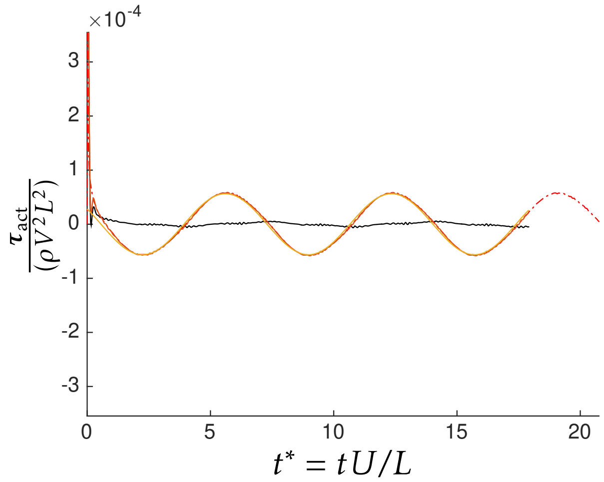

Figure C.4: Motion control test case: actuation moment under various control scheme: imposed kinematic, dashed red; feed-back component, solid black; feed-forward component, solid yellow; feed-back associated to feed-forward, solid red.

of the actuation applied on the joint. This is a quite outstanding result because this really simple method relying only on integration on the body enables to retrieve the actuation need to produce a defined movement.

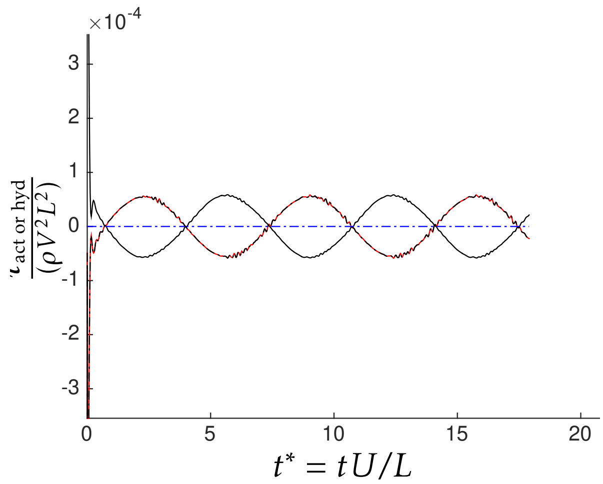

Figure C.5: Motion control test case: central joint hydrodynamic moments : solid red, its component : dashed blue for the projection part and dashed black for the penalization part, and the actuation torque : solid black.

Bibliography

[1] J. O. Dabiri, How fish feel the flow, Nature 547 (2017) 406–407.

[2] A. J. Ijspeert, A. Crespi, D. Ryczko, J.-M. Cabelguen, From swimming to walking with a salamander robot driven by a spinal cord model, Science 315 (2007) 1416–1419.

[3] A. J. Ijspeert, Biorobotics: Using robots to emulate and investigate agile locomotion, Science 346 (2014) 196–203.

[4] S.-J. Park, M. Gazzola, K. S. Park, S. Park, V. Di Santo, E. L. Blevins, J. U. Lind, P. H. Campbell, S. Dauth, A. K. Capulli, F. S. Pasqualini, S. Ahn, A. Cho, H. Yuan, B. M. Maoz, R. Vijaykumar, J.-W. Choi, K. Deisseroth, G. V. Lauder, L. Mahadevan, K. K. Parker, Phototactic guidance of a tissue-engineered soft-robotic ray, Science 353 (6295) (2016) 158–162. arXiv:http://science.sciencemag.org/content/353/6295/158.full.pdf, doi:10.1126/science.aaf4292.
URL http://science.sciencemag.org/content/353/6295/158

[5] M. Gazzola, P. Chatelain, W. M. van Rees, P. Koumoutsakos, Simulations of single and multiple swimmers with non-divergence free deforming geometries, Journal of Computational Physics 230 (2011) 7093–7114.

[6] P. Koumoutsakos, A. Leonard, High-resolution simulations of the flow around an impulsively started cylinder using vortex methods, Journal of Fluid Mechanics 296 (1995) 1–38.

[7] G.-H. Cottet, Level set and penalization methods for fluid structure interaction problems (mai 2011).

[8] F. Boyer, M. Porez, A. Leroyer, Poincaré-cosserat equations for lighthill three-dimensional dynamic model of a self propelled eel devoted to robotics, Journal of Nonlinear Science 20 (1) (2010) 47–79.

[9] M. Porez, F. Boyer, A. J. Ijspeert, Improved lighthill fish swimming model for bio-inspired robots - modelling, computational aspects and experimental comparisons., International Journal of Robotics Research, SAGE Publications (1-34. <10.1177/0278364914525811>. <hal-00943604>).

[10] S. Kern, P. Koumoutsakos, Simulations of optimized anguilliform swimming, Journal of Experimental Biology 209 (24) (2006) 4841–4857. arXiv:http://jeb.biologists.org/content/209/24/4841.full.pdf, doi:10.1242/jeb.02526.
URL http://jeb.biologists.org/content/209/24/4841

[11] M. J. Lighthill, Note on the swimming of slender fish, Journal of Fluid Mechanics 9 (1960) 305–317.

[12] J. Lighthill, Large-amplitude elongated body theory of fish locomotion, Proceedings of the Royal Society B 179 (1971) 125–138.

[13] E. Kanso, J. E. Marsden, C. W. Rowley, J. Melli-Huber, Locomotion of articulated bodies in a perfect fluid, Journal of Nonlinear Science 15 (2005) 255–289.

[14] E. Kanso, Swimming due to transverse shape deformations, Journal of Fluid Mechanics 631 (2009) 127–148.

[15] E. Kelasidi, K. Y. Pettersen, J. T. Gravdahl, P. Liljebäck, Modeling of underwater snake robots, in: 2014 IEEE International Conference on Robotics and Automation (ICRA), 2014, pp. 4540–4547. doi:10.1109/ICRA.2014.6907522.

[16] J. Carling, T. Williams, G. Bowtell, Self-propelled anguilliform swimming: Simultaneous solution of the two-dimensional navier–stokes equations and newton's laws of motion, Journal of Experimental Biology 201 (1998) 3143–3166.

[17] A. Shirgaonkar, M. Maclver, N. Patankar, A new mathematical formulation and fast algorithm for fully resolved simulation of self-propulsion, Journal of Computational Physics 228 (2009) 2366–2390.

[18] J. D. Eldredge, Numerical simulations of undulatory swimming at moderate reynolds number, BIOINSPIRATION & BIOMIMETICS 1 (2006) S19–S24.

[19] L. Zhang, X. Chang, X. Duan, Z. Wang, H. Zhang, A block lu-sgs implicit unsteady incompressible flow solver on hybrid dynamic grids for 2d external bio-fluid simulations, Computers and Fluids 38 (2008) 290–308.

[20] K. Yeo, S. Ang, C. Shu, Simulation of fish swimming and manoeuvring by an svd-gfd method on a hybrid meshfree-cartesian grid, Computers and Fluids 39 (2010) 403–430.

[21] S. Hieber, P. Koumoutsakos, An immersed boundary method for smoothed particle hydrodynamics of self-propelled swimmers, Journal of Computational Physics 227 (2008) 8636–8654.

[22] J. Kajtar, J. Monaghan, Sph simulations of swimming linked bodies, Journal of Computational Physics 227 (19) (2008) 8568–8587.

[23] H. Liu, K. Kwachi, A numerical study of undulatory swimming, Journal of Computational Physics 155 (1999) 223–247.

[24] R. Glowinski, T. Pan, T. Hesla, D. Joseph, J. Periaux, A fictitious domain approach to the direct numerical simulation of incompressible viscous flow past moving rigid bodies: application to particulate flow, Journal of Computational Physics 169 (2001) 363–426.

[25] L. Lee, R. J. Leveque, An immersed interface method for incompressible navier–stokes equations, SIAM Journal on Scientific Computing 25 (2003) 832–856.

[26] R. Mittal, G. Iaccarino, Immersed boundary methods, Annual Review of Fluid Mechanics 37 (1) (2005) 239–261. `arXiv:https://doi.org/10.1146/annurev.fluid.37.061903.175743`, `doi:10.1146/annurev.fluid.37.061903.175743`.
URL `https://doi.org/10.1146/annurev.fluid.37.061903.175743`

[27] M. Saif Ullah Khalid, I. Akhtar, H. Dong, Hydrodynamics of a tandem fish school with asynchronous undulation of individuals, Journal of Fluids and Structures 66 (2016) 19–35.

[28] S. G. Park, B. Kim, H. J. Sung, Self-propelled exible fin in the wake of a circular cylinder, Physics of fluids 28.

[29] T. Engels, D. Kolomenskiy, K. Schneider, J. Sesterhenn, Numerical simulation of fluid–structure interaction with the volume penalization method, Journal of Computational Physics 281 (2015) 96–115.

[30] S. A. Ghaffari, S. Viazzo, K. Schneider, P. Bontoux, Simulation of forced deformable bodies interacting with two-dimensional incompressible flows: Application to fish-like swimming, International Journal of Heat and Fluid Flow, Elsevier, Theme special issue celebrating the 75th birthdays of Brian Launder and Kemo Hanjalic 51 (2015) 88–109.

[31] P. Angot, C.-H. Bruneau, P. Fabrie, A penalization method to take into account obstacles in incompressible viscous flows, Numerische Mathematik 81 (1999) 497–520.

[32] J. D. Eldredge, Dynamically coupled fluid–body interactions in vorticity-based numerical simulations, Journal of Computational Physics 227 (2008) 9170–9194.

[33] M. Coquerelle, G.-H. Cottet, A vortex level set method for the two-way coupling of an incompressible fluid with colliding rigid bodies, Journal of Computational Physics 227 (2008) 9121–9137.

[34] M. M. Hejlesen, P. Koumoutsakos, A. Leonard, J. H. Walther, Iterative brinkman penalization for remeshed vortex methods, Journal of Computational Physics 280 (2015) 547–562.

[35] T. Gillis, G. Winckelmans, P. Chatelain, An efficient iterative penalization method using recycled krylov subspaces and its application to impulsively started flows, Journal of Computational Physics 347 (2017) 490–505.

[36] N. A. Patankar, N. Sharma, A fast projection scheme for the direct numerical simulation of rigid particulate flows, Communications in Numerical Methods in Engineering 21 (2005) 419–432.

[37] C. Wang, J. D. Eldredge, Strongly coupled dynamics of fluids and rigid-body systems with the immersed boundary projection method, Journal of Computational Physics 295 (2015) 87–113.

[38] G.-H. Cottet, E. Maitre, T. Milcent, Eulerian formulation and level set models for incompressible fluid-structure interaction, ESAIM: Mathematical Modelling and Numerical Analysis 42 (2008) 471–492.

[39] E. Kelasidi, P. Liljebäck, K. Y. Pettersen, J. T. Gravdahl, Integral line-of-sight guidance for path following control of underwater snake robots: theory and expreriments, IEEE transactions on robotics 33 (3) (2017) 610–628.

[40] R. Thandiackal, K. Melo, L. Paez, J. Herault, T. Kano, K. Akiyama, F. Boyer, D. Ryczko, A. Ishiguro, A. J. Ijspeert, Emergence of robust self-organized undulatory swimming based on local hydrodynamic force sensing, Science Robotics 6 (57). doi:10.1126/scirobotics.abf6354.
URL https://hal.archives-ouvertes.fr/hal-03430114

[41] J. W. Newbolt, J. Zhang, L. Ristroph, Flow interactions between uncoordinated flapping swimmers give rise to group cohesion, Proceedings of the National Academy of SciencesarXiv:https://www.pnas.org/content/early/2019/01/29/1816098116.full.pdf, doi:10.1073/pnas.1816098116.
URL https://www.pnas.org/content/early/2019/01/29/1816098116

[42] S. Verma, G. Novati, P. Koumoutsakos, Efficient collective swimming by harnessing vortices through deep reinforcement learning, Proceedings of the National Academy of Sciences 115 (23) (2018) 5849–5854. arXiv:https://www.pnas.org/content/115/23/5849.full.pdf, doi:10.1073/pnas.1800923115.
URL https://www.pnas.org/content/115/23/5849

[43] S. Verma, G. Abbati, G. Novati, P. Koumoutsakos, Computing the force distribution on the surface of complex, deforming geometries using vortex methods and brinkman penalization, International Journal for Numerical Methods in Fluids (2017) 1–18.

[44] D. Shiels, A. Leonard, A. Roshko, Flow-induced vibration of a circular cynlinder at limiting structural parameters, Journal of Fluids and Structures 15 (2001) 3–21.

[45] J. D. Eldredge, D. Pisani, Passive locomotion of a simple articulated fish-like system in the wake of an obstacle, Journal of Fluid Mechanics 607 (2008) 279–288.

[46] C. Bernier, M. Gazzola, R. Ronsse, P. Chatelain, Simulations of propelling and energy harvesting articulated bodies via vortex particle-mesh methods, Journal of Computational Physics 392 (2019) 34–55.

[47] C. Bernier, M. Gazzola, P. Chatelain, R. Ronsse, Numerical simulations and development of drafting strategies for robotic swimmers at low reynolds number, in: 2018 7th IEEE International Conference on Biomedical Robotics and Biomechatronics (Biorob) ©2018 IEEE, 2018, pp. 378–383.

[48] C. Bernier, M. Gazzola, R. Ronsse, P. Chatelain, Coupling a vortex particle-mesh method to a multi-body system solver for the simulation of articulated swimmers, in: 7th International Conference on Vortex Flows and Vortex Models (ICVFM), 2016.

[49] C. Bernier, M. Gazzola, R. Ronsse, P. Chatelain, Combining the vortex particle-mesh method with a multi-body system for the simulation of self-propelled articulated swimmers, in: American Physical Society, 2017.

[50] C. Bernier, M. Gazzola, R. Ronsse, P. Chatelain, Numerical simulations and development of drafting strategies for robotic swimmers at low reynolds number, in: Brain Mind Institute Symposium : Controlling Behavior in Animals and Robots (EPFL), 2018.

[51] P. Chatelain, A. Curioni, M. Bergdorf, D. Rossinelli, W. Andreoni, P. Koumoutsakos, Billion vortex particle direct numerical simulations of aircraft wakes, Computer method in applied mechanics and engineering 197 (2008) 1296–1304.

[52] G. Cottet, P. Koumoutsakos, Vortex Methods, Theory and Practice, Cambridge University Press, 2000.

[53] P. Koumoutsakos, Multiscale flow simulations using particles, Annual Review of Fluid Mechanics 37 (2005) 457–487.

[54] C. Bost, G.-H. Cottet, E. Maitre, Convergence analysis of a penalization method for the three-dimensional motion of a rigid body in an incompressible viscous fluid, SIAM Journal on Numerical Analysis 48 (4) (2010) 1313–1337.

[55] G. Carbou, P. Fabrie, Boundary layer for a penalization method for viscous incompressible flow, Advances in Difference Equations 8 (2003) 1453–1480.

[56] C. Wu, L. Wang, Where is the rudder of a fish?: the mechanism of swimming and control of self-propelled fish school, Acta Mechanica Sinica 26 (2010) 45–65.

[57] M. W. Spong, S. Hutchinson, M. Vidyasagar, Robot Modeling and control, John Wiley & Sons, Inc., 2006.

[58] G.-H. Cottet, Optimization of trailing vortex destruction by evolution strategies, Proceedings of the Summer Programm (2000) 75–82.

[59] K. Namkoong, J. Y. Yoo, H. G. Choi, Numerical analysis of two-dimensional motion of a freely falling circular cylinder in an infinite fluid, Journal of Fluid Mechanics 604 (2008) 33–53.

[60] F. Noca, On the evaluation of instantaneous fluid-dynamic forces on a bluff body, GALCIT Report FM96-5.

[61] C. Mimeau, F. Gallizio, G.-H. Cottet, I. Mortazavi, Vortex penalization method for bluff body flows, International Journal for Numerical Methods in Fluids (79) (2015) 55–83.

[62] M. Gazzola, B. Hejazialhosseini, P. Koumoutsakos, Reinforcement learning and wavelet adapted vortex methods for simulations of self-propelled swimmers, Journal of Computational Physics 36 (3) (2014) B622–B639.

[63] D. N. Beal, F. S. Hover, M. S. Triantafyllou, J. C. Liao, G. V. Lauder, Passive propulsion in vortex wakes, Journal of Fluid Mechanics 549 (2006) 385–402.

[64] E. Kelasidi, P. Liljebäck, K. Y. Pettersen, J. T. Gravdahl, Biologically inspired swimming snake robot, IEEE Robotics & Automation Magazine 23 (1) (2016) 44–62.

[65] A. Gilmanov, F. Sotiropoulosin, A hybrid cartesian/immersed boundary method for simulating flows with 3d, geometrically complex, moving bodies, Journal of Computational Physics 207 (2005) 457–492.

[66] D. Weihs, Hydromechanics of fish schooling, Nature 241 (1973) 290–291.

[67] M. Gazzola, A. Tchieu, D. Alexeev, A. D. Brauer, P. Koumoutsakos, Learning to school in the presence of hydrodynamic interactions, Journal of Fluid Mechanics 789 (2016) 726–749.

[68] G. Novati, S. Verma, D. Alexeev, D. Rossinelli, W. M. van Rees, P. Koumoutsakos, Synchronisation through learning for two self-propelled swimmers, Bioinspiration & Biomimetics 12.